Scientific Research Associates, inc.

AD-A249 446

‖‖‖‖‖‖‖‖‖‖‖‖‖

50 Nye Road, P.O. Box 1058
Glastonbury, Connecticut 06033
(203) 659-0333   FAX (203) 633-0676

Report R92-920036-F

ACTIVE CONTROL OF PRESSURE, SOUND AND VELOCITY OF

CENTRIFUGAL PUMPS

DTIC
ELECTE
APR 2 3 1992
S   D
C

D. G-N. Tse, I.S. Sabnis, and H. McDonald

Scientific Research Associates, Inc.
50 Nye Road, P.O. Box 1058
Glastonbury, CT 06033

and

James H. Whitelaw

Imperial College
Department of Mechanical Engineering
Exhibition Road
London SW7 2 BX
England

Final Report
Contract N00014-89-C-0090

Prepared for:

Office of Naval Research
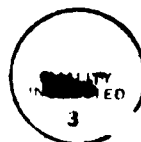Department of the Navy
Arlington, VA 22217-5000

92-09192

‖‖‖‖‖‖‖‖‖‖‖‖

March 1992

Approved for public release;
Distribution unlimited

9 2   09 0 27

ABSTRACT

Measurements of velocity, pressure and sound have been obtained in a centrifugal pump with a four blade impeller rotating at speeds between 1470 rpm and 3510 rpm to improve understanding of noise generation and to investigate the feasibility of reducing fluid dynamic noise with active control. The velocity results show flow separation in the region near the shroud wall and at the suction surface of the blades with the flow driven inward by the adverse pressure gradient near the shroud wall. The frequency spectra of the pressure distributions obtained inside the pump casing at 3510 rpm showed a dominant frequency of 50 to 60 dB above the background level associated with the blade passing frequency of approximately 240 Hz. However, the saw-tooth waveform observed in the pressure characteristic also comprised of second and third harmonics of 45 to 55 dB and 35 to 45 dB above the background level and another 8 higher harmonics with diminishing amplitude as the frequency increased. The pressure distribution underwent a circumferential variation which was believed to stem from resonance or suppression of the 11 harmonic frequencies due to circumferential variation of the geometry of the scroll. All the waveforms inside the pump were generated by 11 sinusoids of different amplitudes. Only the first three harmonics contained sufficient energy to produce a detectable signature in the air-borne noise characteristics. Consequently, there were some difference between the waveforms of the pressure and air-borne noise distributions. Intermediate maxima and minima were evident in air-borne noise characteristics but not in pressure distributions. This was due to the absence of the low amplitude high harmonic frequencies which had an effect of smoothing the waveform. A frequency of approximately 60 Hz, stemmed form blade-to-blade variation due to geometrical imperfection of the impeller, was marked by a spike of 45 dB above the background level in the frequency spectra of the pressure characteristics inside the pump. It was also evident in the frequency spectra of the air-borne noise because the energy of the cyclic blade-to-blade variation was as large as the third harmonics of the blade tone. Pressure characteristics obtained at 1470, 1770, 2340 and 2920 rpm were similar to that of 3510 rpm. The pressure fluctuations at 1470 and 1770 rpm were too low to produce any signature in the air-borne noise but the characteristics obtained at 2340 and 2920 rpm were similar to those obtained at 3510 rpm.

-1-

1. INTRODUCTION

Considerable attention has been paid to the flow characteristics of centrifugal, radial and mixed-flow compressors, see for examples Refs. 1 to 6. In general, these references describe investigations confined to locations accessible through the inlet and limited regions of the impeller passage. Understanding of the performance of the compressors is based on a substantial literature which is reviewed, for example, in Ref. 7. These early studies included extensive measurements of wall pressure and velocity in the intake and exit ducts. Much less emphasis has been placed directly on pumps, partly because their performance is closely linked to that of compressors, with the added assumption of incompressible flow, and partly because performance improvements are less financially beneficial. A summary of recent internal flow studies in centrifugal pumps has been given by Ref. 8. There is, however, interest in noise reduction, increased specific flow rates and reductions in size and geometric complexity and information of the local flow characteristics is required to provide the essential understanding.

The purpose of this report is to summarize the work done in the past two years for the research contract with the Office of Naval Research on the Active Control of Noise in centrifugal pumps. The objective of this research program was to investigate the links between fluid dynamics and noise generation in centrifugal pumps and to determine the extent to which the noise can be controlled by active control, based on feed-back of pressure and velocity-based signals. The geometries and rotational speeds are relevant to the pumps of naval vessels and the measurement techniques include laser velocimetry, miniature pressure transducers and free-field microphones with velocity measurements in the proximity of the impeller facilitated by the use of transparent materials and a working fluid with matched refractive index.

Measurements have been made at SRA and Imperial College with identical pump facilities, with initial emphasis at SRA being on the measurement of pressure and sound and the effort at Imperial College focusing on velocity measurements. Thus, instantaneous and ensemble-averaged pressure and sound have been measured as a function of impeller angle at SRA with velocity results obtained at Imperial College. Both SRA and Imperial College have the capability of obtaining velocity, pressure and sound measurements in rotating machineries.

The following section describes the flow configuration, the instrumentation and the possible sources of uncertainty. Results are presented and discussed in Section 3. Summary conclusions are included in the final section.

2. FLOW CONFIGURATION AND INSTRUMENTATION

Figure 1 shows the experimental arrangement including the pump, circuit for the temperature-controlled liquid and the shaft encoder used for identification of the circumferential location and the rotational speed of the impeller. The centrifugal pump (Price model SC100-150) was driven by an electric motor at speeds of up to 3540 rpm and circulated liquid from and to a 150 liter tank through a 36 mm inlet pipe and a 28.5 mm outlet pipe. The coordinate systems for measurements in the impeller and the casing are identified in Figure 2. The impeller had 4 backward-swept blades of 2.5 mm thickness and width which tapered from 11.2 mm at the 21 mm impeller radius to 6.2 mm at 62.3 mm outer radius where the blade angle was $58°$ $±1°$. The clearance between the impeller blade and casing was 0.5 mm for the velocity measurements obtained with the acrylic casing and 0.8 mm for the pressure and sound measurements obtained with the metal casing. The difference was due to manufacturing tolerances in the pump casing and the impeller and can be eliminated by replacing the gasket in the metal casing in future work.

The working fluid was a mixture of 68% (by volume) turpentine and 32% tetraline (1,2,3,4-tetrahydronathalene) with density and kinematic viscosity of 0.893 kg/m^3 and 1.74×10^{-6} m^2/s respectively at $26°$ C. The temperature of the mixture was monitored by a platinum resistance sensor and was maintained at $26 ± 0.5°$ C by a feedback controller to maintain a refractive index of 1.49 which was identical to that of the acrylic. The flow rate of the mixture was controlled by a valve in the pipe downstream of the pump and this was adjusted to provide a flow rate of 1.57×10^{-3} m^3/s, corresponded to 60% of the design flow rate, and measured by an orifice plate, calibrated to be accurate within 3%. The bulk mean velocities in the inlet and outlet pipes were 1.54 and 2.46 m/s corresponding to Reynolds numbers of 34000 and 43000.

The laser velocimeter comprised an argon-ion laser tuned to the green line and operating at powers from 0.1 to 0.8 W depending on the angle at which the scattered light was collected. The transmission optical components were based on a diffraction grating which divided the beam and provided frequency shifts up to 13 M Hz and the collection system on a collecting lens of 33 mm aperture and 200 mm focal length with a 300 μm diameter pinhole and a photomultiplier (EMI model 9817B). Rotation of the transmission optical components allowed the measurement of two orthogonal components of velocity and the third component was measured by realigning the velocimeter. The optical components were secured to an optical bench which was translated in three orthogonal directions with accuracy of location of better than 0.1 mm in each direction. A summary of the optical characteristics of the velocimeter is provided in Table 1.

TABLE I

Characteristics of the Laser-Doppler Velocimeter

Laser wave-length	514.8	nm
Beam intersection angle	9.7	deg
Measurement volume length at $1/e^2$ intensity	620	μm
Measurement volume diameter at $1/e^2$ intensity	53	μm
Fringe spacing	3.04	μm
Number of fringes	17	
Frequency shift	0-13	MHz

The Doppler signal was based on natural contaminants in the liquid, arrived at a rate corresponding to 20 per degree, and was processed by a frequency counter (TSI model 1990C) and interfaced to a microcomputer (IBM PC-AT) together with the pulse train from the optical shaft encoder which corresponded to a resolution of 0.25°. A marker pulse per rotation from the encoder identified the same angle on each rotation. The digital information was collected in sequences of 4×10^5 velocity values and used subsequently to provide angle-resolved velocity traces of up to 2500 rotation cycles or ensemble averaged values based on angles of 1° with between 1000 and 4000 velocity values depending on the magnitude of the rms of the fluctuations.

The possible sources of uncertainty associated with laser velocimeters have been considered in many contributions and only velocity gradient and statistical broadening were important here. Spatial gradients were greatest in the vicinity of the pressure and suction face of the impeller blades and the maximum uncertainties, minimized by the small effective length of the measurement volume, were less than 0.5% in the estimates of the rms velocities; the corresponding angle-broadening errors were less than 1%. Statistical uncertainties were maintained unimportant by ensuring a sufficient number of velocity data in each ensemble average. Ensemble-averaged information over 360° is presented at locations where the impeller influence is small. As a consequence of the above, the maximum uncertainties in the ensemble-averaged mean and rms velocities are not expected to exceed 2 and 5% of the local

values, respectively. The use of refractive-index-matching minimized the positioning errors in the model to an order of 0.2 mm.

A Kulite miniature transducer was used for pressure measurements inside the casing and the scroll. It was flush mounted on the wall at locations shown in Figure 3(a) for the time-resolved pressure measurements. The measuring position was selected by installing the miniature transducer at the appropriate pressure tap. The data acquisition system was based on an IBM/PC compatible microcomputer with the triggering provided by the shaft encoder. The data acquisition hardware obtained instantaneous pressure measurements throughout the 360° rotation as a function impeller angle. A marker pulse from the shaft encoder identified the starting angle on each rotation. The processing software was specially developed for these rotating machinery studies and provided values of ensemble-averages of each single-trace distributions at each location.

The miniature pressure transducer involved an uncertainty of 3% and the measurements discussed in Section 3 show that the pressure gradient is less than 1% of the local pressure so that spatial-gradient broadening is insignificant. Statistical uncertainty in the mean pressure measurements associated with a finite sample size can be estimated using the equation:

$$\overline{U}_C = \frac{S}{\sqrt{N}} \times \frac{\sqrt{\overline{u^2}}}{\overline{U}}$$

where S is equal to 2 for a 95% confidence limit. The sample size in each ensemble averages was 440 and the turbulence intensities were below 16% in all cases. The resulting statistical uncertainty was less than 2% in each ensemble-averaged pressure. The corresponding uncertainty in the rms values can be estimated from the expression:

$$\sqrt{\overline{u_C^2}} = \frac{S}{\sqrt{2N}}$$

which indicates, with 95% confidence, an accuracy of better than 7% for the sample size used in the measurements. The above analysis indicates that the overall uncertainty in the mean and rms pressure measurements were less than 4% and 8% respectively. A Bruel and Kjaer microphone was used to analyze the free-field sound characteristics which were obtained with the microphone located 1 m from the pump. The data acquisition hardware and the processing software were the same as those used for the pressure measurements. The results discussed in Section 3 show that there was no steep gradient in the sound measurements and spatial-gradient broadening was

unimportant. Statistical uncertainties were less than 2% and 7% of the mean and rms values for the sample size used in the experiments.

3. RESULTS AND DISCUSSION

3.1 Velocity Characteristics

The flow field within a blade passage is depicted by the vector plots of Figure 4 in a relative coordinate frame and was obtained by combining the angle-resolved radial and tangential velocity component measurements from six radial and three axial locations in one blade passage. In the mid-plane of the impeller, the flow appears to be guided reasonably well by the lagging convex blade face and less so by the leading concave face, particularly at the impeller discharge. The flow angle close to the outer radius is larger than the blade angle, indicating a slip effect which is partly attributed to the small number of blades and partly to the off-design operation of the pump. The flow in the plane nearer to the hub is similar to that on the mid-plane with the exception of flow angle at the inner radii and near the leading blade where it is affected by secondary flow which extends to a large region of the passage. The flow in the plane close to the shroud wall is totally different with most of the flow directed inwards at radii greater than 80% of the impeller radius. This is a typical feature of open impeller design and results from pressure gradient between scroll and center of the impeller. Similar vortex structure have been observed by Refs. 9 and 10 but not quantified as in the present work. A tendency of the flow to turn in the opposite direction to the blade is seen at 71% and 65% of the impeller radius near the concave face the leading blade, indicating the presence of flow recirculation. Measurements at inner radii closer to the concave face of the leading blade were limited by the obstruction of scattered light by the curved blade and this limitation can be removed by an acrylic impeller. These results are described in greater detail in Ref. 11.

3.2 Pressure Measurements

The ensemble-averaged static pressure distributions as a function of impeller angle at seven locations indicated in Figure 3(a) for impeller speeds between 1470 to 3510 rpm are presented in Figures 5 to 9. Pressure measurements were made for five different rotational speeds at four circumferential locations on the shroud wall and three locations on the diffuser. Figures 5(a) through 5(d) show that the blade tone is clearly seen in the pressure and shaft angle plots at all locations on the shroud wall obtained with 3510 rpm. The pressure distribution resemble a

saw-tooth wave and the corresponding frequency spectra review a fundamental frequency of around 240 Hz and another 10 harmonic frequencies. The amplitude of the fundamental frequency is generally 50 to 60 dB above the background level, the second harmonic, 45 to 55 dB and the third, 35 to 45 dB. The eleventh harmonic is still distinguishable from the background level. The measurements obtained at approximately 30° before and after the cut-off, Figures 5(a) and 5(c), show a more complex waveform with multiple-peaks but the same 11 harmonic frequencies are clearly evident in the corresponding frequency spectra. The saw-tooth waveform and the harmonic frequencies are also evident in the waveforms and frequency spectra obtained in the diffuser, Figures 5(e) to 5(g), and the remaining rotational speeds, Figures 6 to 9. Thus all the waveforms inside the pump are generated by sinusoids of different amplitudes and frequencies at multiples of the fundamental blade tone. The variations in the pressure distributions at the four location shown in Figure 5(a) to 5(d) indicate that the flow pattern within a blade passage undergoes circumferential variation. This variation is likely to stem from resonance and suppression of the different harmonics associated with the circumferential change in geometry of the scroll.

A distinct cyclic blade-to-blade variation caused by geometric variations among the blades is also quite evident in the pressure distributions presented in Figures 5(a) to 5(d). The magnitude of the blade-to-blade variation within the impeller is approximately 10% of the pressure fluctuation amplitude and is represented by a spike of 45 dB above the background level in the corresponding frequency spectra at 60 Hz. The variation is apparently more noticeable in the measurements obtained in the diffuser, Figures 5(e) to 5(g) because of the different in plotting scale and is also represented by a spike of 45 dB above the background level in the frequency spectra. The maximum revolution-averaged pressure in the diffuser is almost twice that of 80% of the dynamic head of the impeller observed at the edge of the impeller discharge. However, the corresponding pressure fluctuation is less, generally 20% of the dynamic head of the impeller in contrast to the 40% observed at the impeller discharged.

Static pressures near the shroud wall and close to the impeller discharge have particularly large fluctuations - for example, at 3510 rpm (Figure 5(b)) the pressure fluctuation at the cutoff reaches 100 kPa (40% of the dynamic head of the impeller) and at 1470 rpm (Figure 9(b)), 26 kPa (60% of the dynamic head of the impeller). Since the free-field sound intensity depends on the magnitude of the pressure fluctuations inside the pump casing, the large pressure fluctuation at the tip of the impeller is likely to be an important noise source. The absolute magnitude of the pressure fluctuation at 3510 rpm is higher than those at lower rotational speeds and it is expected to produce a more distinct signature in the air-borne noise, as evident in the results in the sound measurements in the following section. Comparison of Figures 5(b) and 5(g) show that, at 3510 rpm, the maximum revolution-averaged pressure in the diffuser is up to 100%

higher than that at the edge of the impeller. However, the corresponding pressure fluctuation in the diffuser is less, 20% of the dynamic head of the impeller in contrast to 40% observed at the edge of the impeller. Thus, the pressure distribution at the edge of the impeller has a greater effect on the air-borne noise characteristics and this is confirmed by the sound measurements presented in the following section.

The revolution-averaged pressure is highest at the cutoff at all rotational speeds and decreases along the direction of rotation - for example at 150° (Figures (d) of Figures 5 to 9) and 330° (Figures (a) of Figures 5 to 9) away from the cutoff, the revolution-averaged pressures are 10% and 20% below that at the cutoff, respectively. The static pressure increase evaluated from the difference between the revolution-averaged pressure and the inlet pressure is roughly equal to 60% of the dynamic head of the impeller at 3510 and 2920 rpm. Reducing the impeller speed to 2340, 1770 and 1470 rpm decreases the pressure rises to 55%, 43% and 25% of the dynamic head respectively. As expected, the performance of the pump reduces sharply as the deviation from design speed increases.

3.3 Sound Measurements

Ensemble-averaged free-field sound distributions obtained with the acrylic casing for an impeller speed of 3510 rpm at four locations indicated in Figure 3(b) are shown in Figure 10. Sound characteristics obtained at the same locations at impeller speeds between 1470 rpm to 3510 rpm with the aid of a frequency controller are show in Figures 11 and 15. A frequency controller is known to produce background noise that may interfere with the sound measurements. This effect can be quantified by comparison of the results obtained at 3510 rpm with the motor connected directly to the main and via the frequency controller. It is evident from the frequency spectra of Figures 10 and 11 that the controller does have any detectable effect at 60 Hz and it does not generate any noise at frequencies associated with the pump at 50 and 40 Hz. Thus, conclusions based on the results obtained with the aid of the frequency controller at 50 and 40 Hz are still valid but the results for 3510 rpm in the subsequent discussion will be based on those obtained without the use of the controller.

The fundamental frequency of the blade tone and its second and third harmonics are clearly evident in all the frequency spectra in Figures 10, 12 and 13 for impeller speeds between 2340 rpm to 3510 rpm. According to Refs. 12 and 13, the intensity of the free-field sound is proportional to the 8th power of the Mach number and the radiation efficiency of fluctuating pressure associated with rotating blade is low for impeller tip speed well below sonic. Nevertheless, sufficient energy is radiated to the free-field from the large pressure fluctuation associated with the first three harmonics inside the pump even at impeller tip speeds between

15.76 m/s and 23.65 m/s to produce a signature in the airborne noise. The free-field sound characteristics obtained at 150° after the cutoff, Figure 10(a), show distinct similarity to the pressure distribution obtained at 27.5° after the cutoff. As expected, the pressure fluctuation inside the pump and the free-field sound characteristics are related. The measurements obtained perpendicular to the 180° axis and at $=0°$, Figures 10(b) and 10(d), show that the waveform of the air-borne noise has a base frequency of three times higher than that of the pressure distribution. The differences in the waveforms between the air-borne noise and the pressure characteristic inside the pump are due to the absence of the 4th to 11th harmonics which do not contain enough energy to effect the signature of the air-borne noise. The 4th to 11th harmonics . are obviously smoothing the waveform of the pressure distribution. Another reason for the differences is that the miniature transducer detects a local effect and the microphone, a global effect. The results presented in the last section showed that the pressure distribution undergoes a substantial circumferential variation. The higher frequency signature detected by the microphone represents a superimposed pattern produce by the resulting interferencing of the free-field sounds radiated from fluctuating pressure at different locations. Thus, the circumferential pressure variation may have a drastic effect on the characteristics of the airborne noise close to the source. The substantial variation in the free-field sound characteristics detected 1 m away from the source, Figures 10(a) to 10(d), may also be a consequent of different interference. It is anticipated that a distant microphone would detect the pump as a point source for. The effect of the circumferential pressure variation would decrease with distance away from the source and consequently the air-borne noise detected from different direction would have a similar waveform.

The sound measurements at 1470 and 1770 rpm, Figures 14 and 15, show mechanical noises of 150 and 90 Hz generated by the coupling. The fluid dynamic noises may not be able to radiate to the free-field at low impeller speed because the corresponding pressure fluctuation inside the pump is low or they are swamped by the mechanical noise generated by resonance of the structure.

The measurements obtained at 3510, 2920 and 2340 rpm with the metal casing are presented in Figures 16 to 18. The results are similar to those obtained with the acrylic casing but the amplitude of the waveform and the corresponding spike in the frequency spectra for the metal casing are lower. According to Ref. 14, the acoustic impedance of acrylic is lower than that of metal. Thus, the same level of pressure fluctuation inside the metal casing will produce a weaker signature in the air-borne noise characteristic than the acrylic counterpart.

The active control system used to remove or reduce the air-borne noise must be able to respond to the instantaneous changes in the waveform. For this reason, single point measurements were obtained at 3510 rpm to verify the ability of the current instrumentation to

detect instantaneous changes. The results obtained at the same locations as those of the ensemble-averaged measurements are presented in Figures 19(a) to 19(d). The waveforms are not as smooth as those of the ensemble-averaged results and the spikes in corresponding frequency spectra obtained form single point measurements are less define. Nevertheless, instantaneous measurements can be obtained satisfactorily with the existing instrumentation. It is evident from the pressure and sound measurements that the first three harmonics are the most important in the active control of removing or reducing the air-borne noise. Pressure measurements should be used as the feedback because the air-borne noise characteristics may be affected by external interference.

4. CONCLUSIONS

A rig has been constructed to study the links between fluid dynamics and noise generation in centrifugal pumps. Instrumentation and software have been developed to obtain velocity, pressure and sound measurements and ensemble-averaged values of velocity, pressure and sound have been obtained for several conditions to provide a better understanding of the physical mechanisms associated with noise generation in centrifugal pumps. The results also provide a basis for the follow-on investigation of active control of the centrifugal pump's noise. The following conclusions can be extracted from the initial results obtained with impeller speeds in the range 1470 rpm to 3510 rpm:

1. The velocity measurements showed flow separation in the region near the suction surface of the blade and inwards flow caused by the adverse radial pressure gradient near the shroud wall.

2. The frequency spectra of the pressure distributions obtained inside the pump casing at 3510 rpm showed a dominant frequency with amplitude of 50 to 60 dB above the background level associated with the blade passing frequency of approximately 240 Hz. However, the saw-tooth waveform observed in the pressure characteristic also comprised second and third harmonics with amplitude of 45 to 55 dB and 35 to 45 dB above the background level and another 8 higher harmonics with diminishing amplitude as the frequency increased. The pressure distribution underwent a circumferential variation which was believed to stem from resonance or suppression of the 11 harmonic frequencies due to circumferential variation of the geometry of the scroll. All the waveforms inside the pump were generated by 11 sinusoids of different amplitudes. A frequency of approximately 60 Hz, stemmed form blade-to-blade variation due to

geometrical imperfection of the impeller, was marked by a spike of 45 dB above the background level in the frequency spectra.

3.   At 3510 rpm, the maximum revolution-averaged pressure at the tip of the impeller and the diffuser achieved 60 and 120% of the dynamic head of the impeller and the corresponding pressure fluctuations, 40 and 20%. Since the airborne sound intensity depended on the magnitude of pressure fluctuation, the large fluctuation at the impeller discharge region was likely to be a more important noise source and this was confirmed by air-borne noise measurements. However, the impeller tip speed was well below sonic and, as a result, the radiation efficiency of the fluctuating pressure was very low and consequently, the amplitude of the airborne noise was low.

4.   Operating the pump at 1470 rpm instead of 3510 rpm increased the pressure fluctuation at the cutoff from 40% of the dynamic head of the impeller to 60%, but the magnitude of the fluctuation decreased from 100 to 26 kPa.

5.   The frequency of the rotating blade of approximately 240 Hz was evident in the ensemble-averaged free-field sound measurements obtained at 3510 rpm with the metal and acrylic casings. Measurements obtained with the metal casing showed weaker signature due to its higher acoustic impedance. Only the first three harmonics contained sufficient energy to produce a detectable signature in the air-borne noise characteristics. Consequently, there were some difference between the waveforms of the pressure and air-borne noise distributions. Intermediate maxima and minina were evident in air-borne noise characteristics but not in pressure distributions. This was due to the absence of the low amplitude high harmonic frequencies which had an effect of smoothing the waveform. The cyclic blade-to-blade variation also produced a 60 Hz signature in the frequency spectra of the air-borne noise because it contained as much energy as the third harmonic of the blade tone.

6.   The instantaneous sound measurements obtained at 3510 rpm reviewed the same findings as the ensemble-averaged measurements but the signature was less distinct.

7.   Pressure characteristics obtained at 1470, 1770, 2340 and 2920 rpm were similar to that of 3510 rpm. The pressure fluctuations at 1470 and 1770 rpm were too low to produce any signature in the air-borne noise but the characteristics obtained at 2340 and 2920 rpm were similar to those obtained at 3510 rpm.

REFERENCES

1.   Eckardt, D.(1976) "Detailed flow investigations within a high-speed centrifugal compressor impeller," *Trans. ASME J. of Fluids Eng.*, 390.

2.   Eckardt, D. (1980) "Flow field analysis of radial and backswept centrifugal compressor impellers, Part 1: Flow measurement using a laser velocimeter," 25th ASME Gas Turbine Conference and 22nd Annual Fluids Engineering Conference, New Orleans. Symposium Performance Prediction of Centrifugal Pumps and Compressors Proceeding published by ASME.

3.   Schodl, R. (1984) "Optical techniques for turbomachinery flow analysis". Lecture to NATO Advanced Study Institute on Thermodynamics and Fluid Mechanics of Turbomachinery, held in Turkey.

4.   Sideris, M. Th. and Van den Braembussche, R. A. (1987) "Influence of a circumferential exit pressure distortion on the flow in an impeller and diffuser," *Trans. ASME J. of Turbomachinery*, 109, 48.

5.   Khezzar, L. Vafidis, C. and Whitelaw, H. J. (1987) "Laser velocimetry for the measurement of air velocity in a centrifugal compressor," Imperial College, Fluids Section, Report FS/87/36.

6.   Paone, N., Riethmuller, M. L. and Van den Braembussche, R. A. (1989) "Experimental investigation of the flow in the vaneless diffuser of a centrifugal pump by particle image displacement velocimetry," *Experiments in Fluids*, 7, 371.

7.   Cumpsty, N. A. (1989) Compressor Aerodynamics, Longman, U.K.

8.   Miner, S. M., Beaudoin, R. J. and Flack, R. D. (1989) "Laser velocimeter measurements in a centrifugal flow pump, *Trans. ASME, J. of Turbomachinery*, 111, 205.

9.   Hamkins, C. P. and Flack, R. D. (1987) "Laser velocimeter measurements in shrouded and unshrouded radial flow pump impellers," *Trans. ASME, J. of Turbomachinery*, 109, 70.

10. Nouri, J. M., Vafidis, C. and Whitelaw, J. H. (1989) "Characteristics of turbulent flow in a model centrifugal pump," Imperial College, Fluids Section, Report FS/89/29.

11. Liu, C.H. Nouri, J.M., Vafidis, C. and Whitelaw, J.H. (1990) "Experimental Study of the Flow in a Centrifugal Pump," Imperial College Report FS/90/12.

12. Koopman, G.H., Neise, W. and Chen, W. (1987) "Active Noise Control to Reduce the Blade Zone Noise of Centrifugal Fans," *J. of Vibration, Acoustic, Stress and Reliability*.

13. Yeager, D.M. and Lauchle, G.C. (1987) "Measurement and Analysis of Noise Radiated by Low Mach Number Centrifugal Blowers". The Pennsylvania State University, Applied Research Lab, Report TR 87-009.
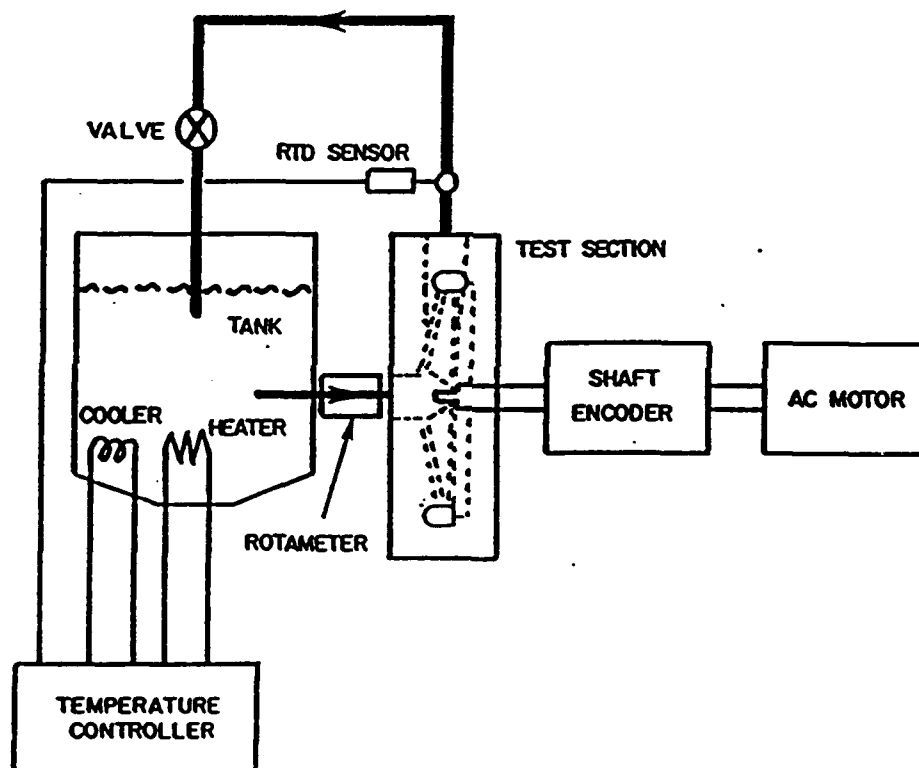
Figure 1   Flow Configuration.
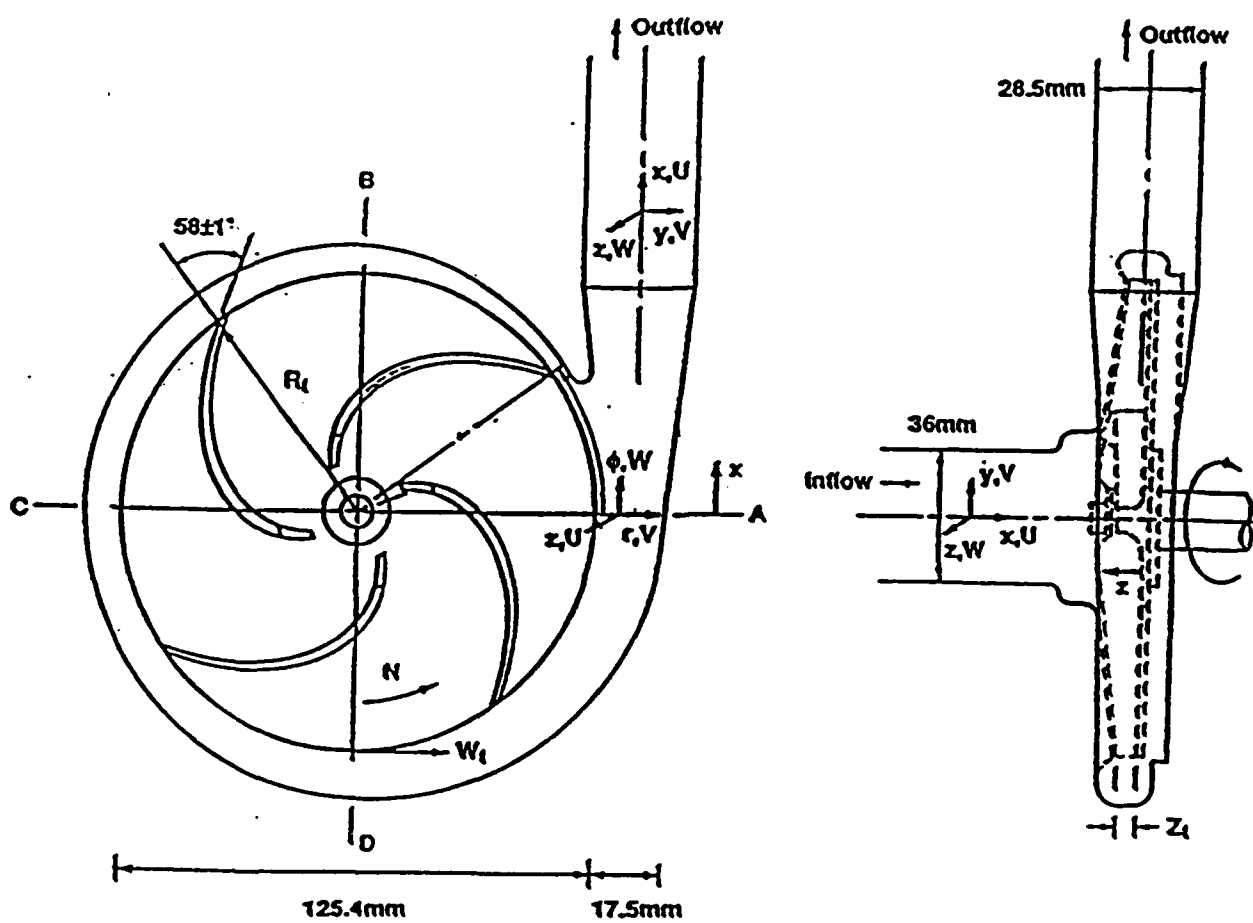
Figure 2   Dimensions of the Centrifugal Pump and Coordinate Systems.
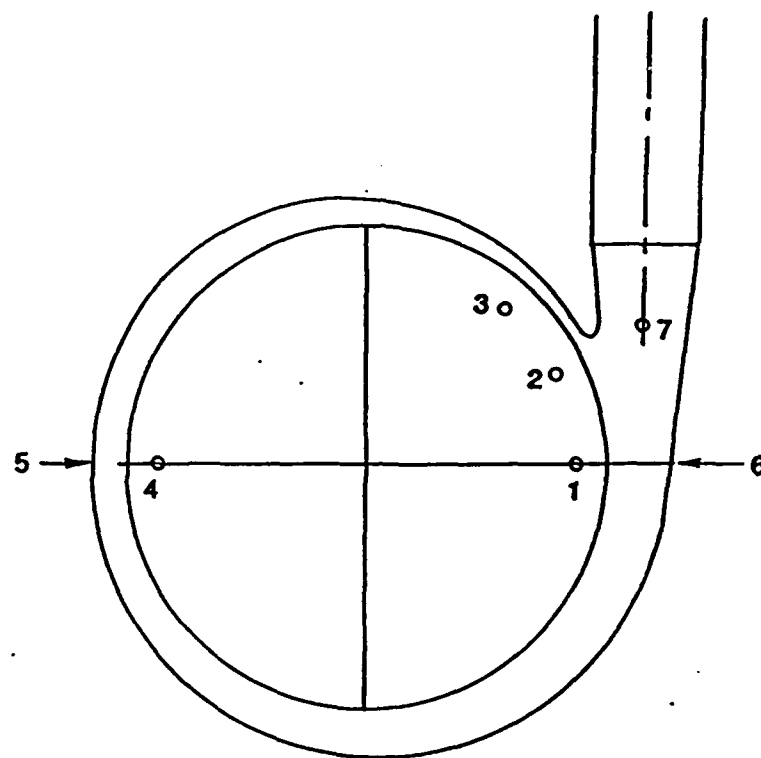
Figure 3(a) Measuring Locations of Miniature Pressure Transducer.
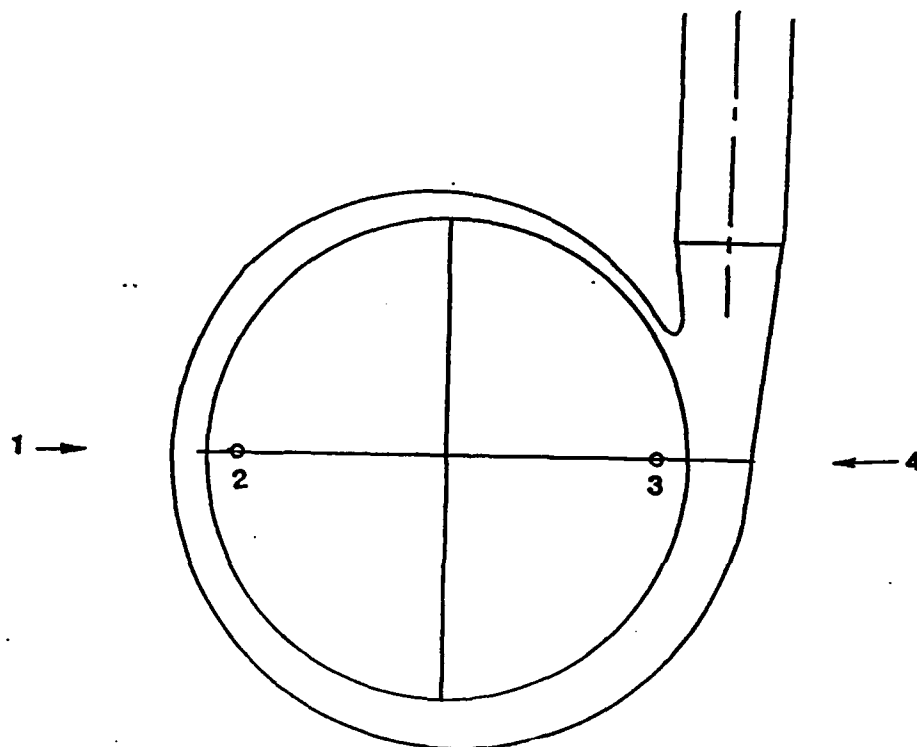
Figure 3(b) Measuring Locations of the Microphone .
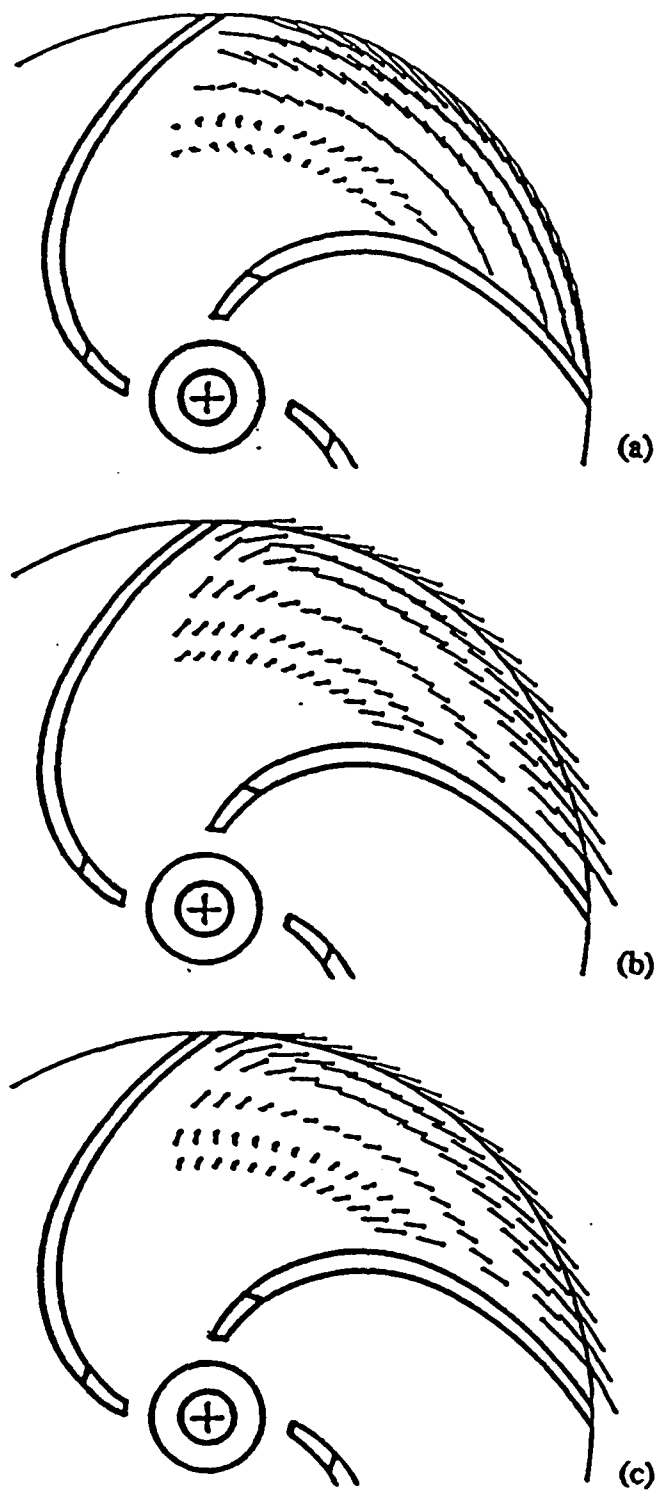
Figure 4   Relative Flow within an Impeller Blade Passsage:
r = 65%, 71%, 81%, 90%, 95% and 100% of the Impeller Radius.

(a) Plane at 1mm from the Shroud
(b) Plane in the Middle of the Blade Passage
(c) Plane at 1mm from the Impeller Hub
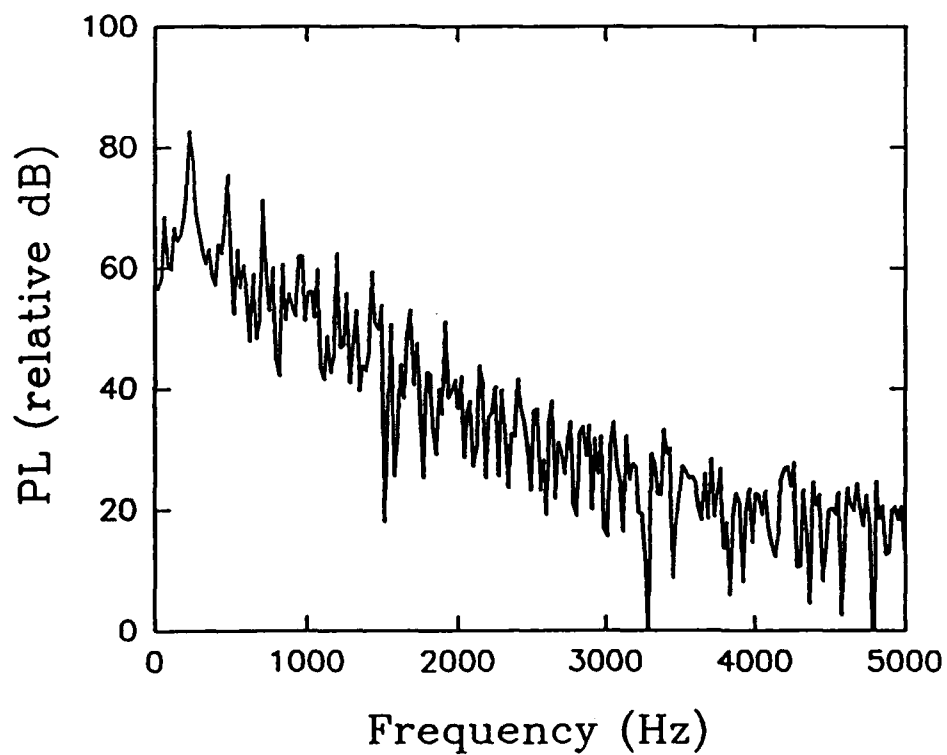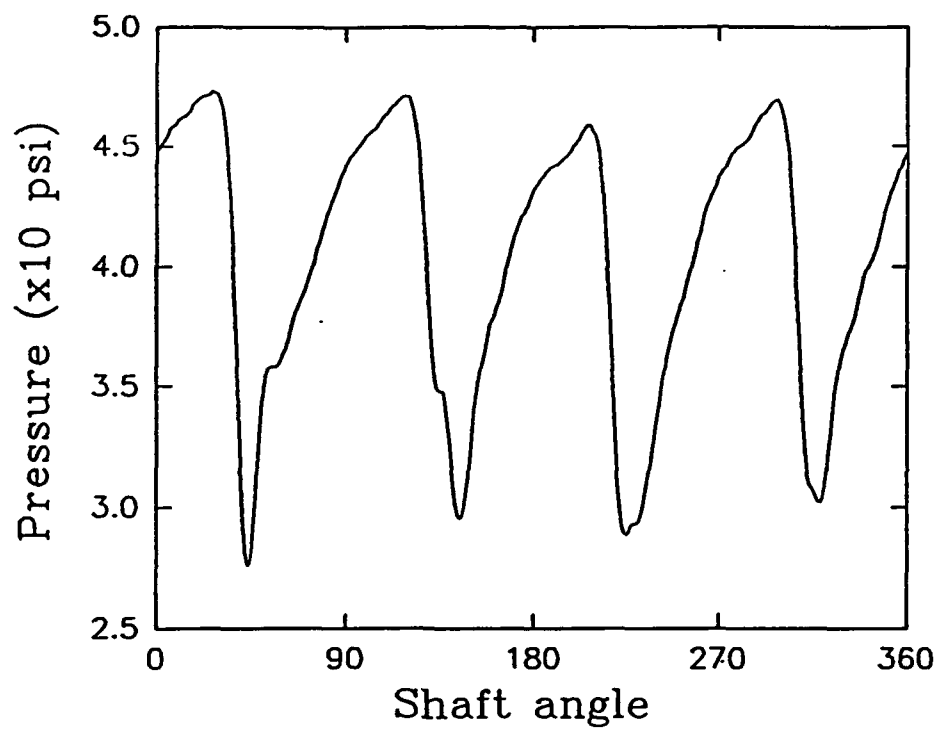
Figure 5(a)   Pressure Distribution and Frequency Spectra Obtained at 3510 rpm at Location 1.
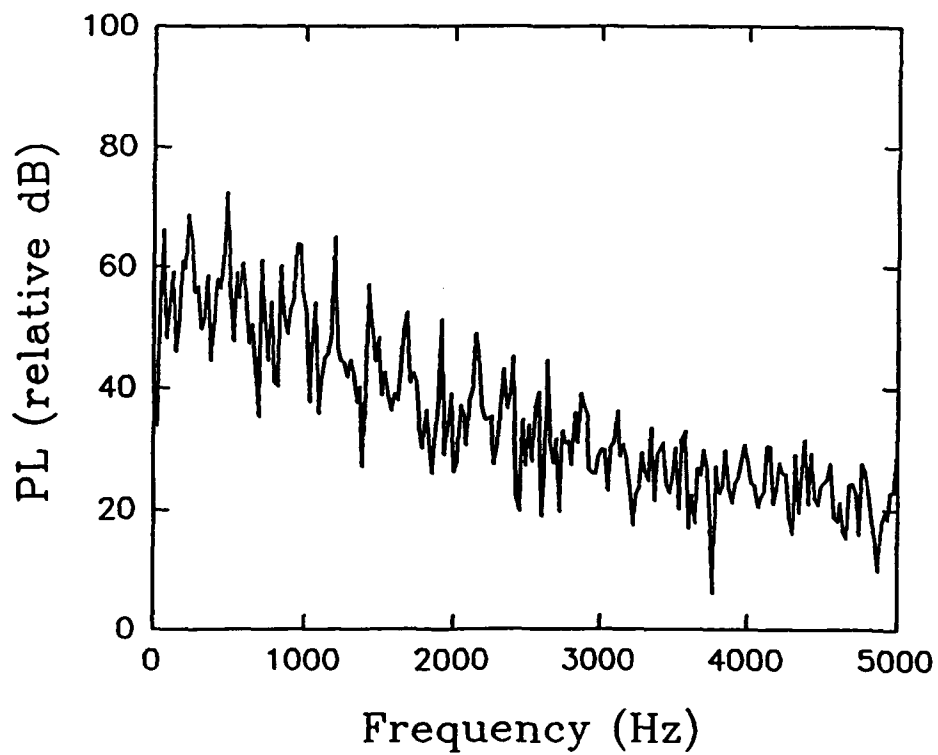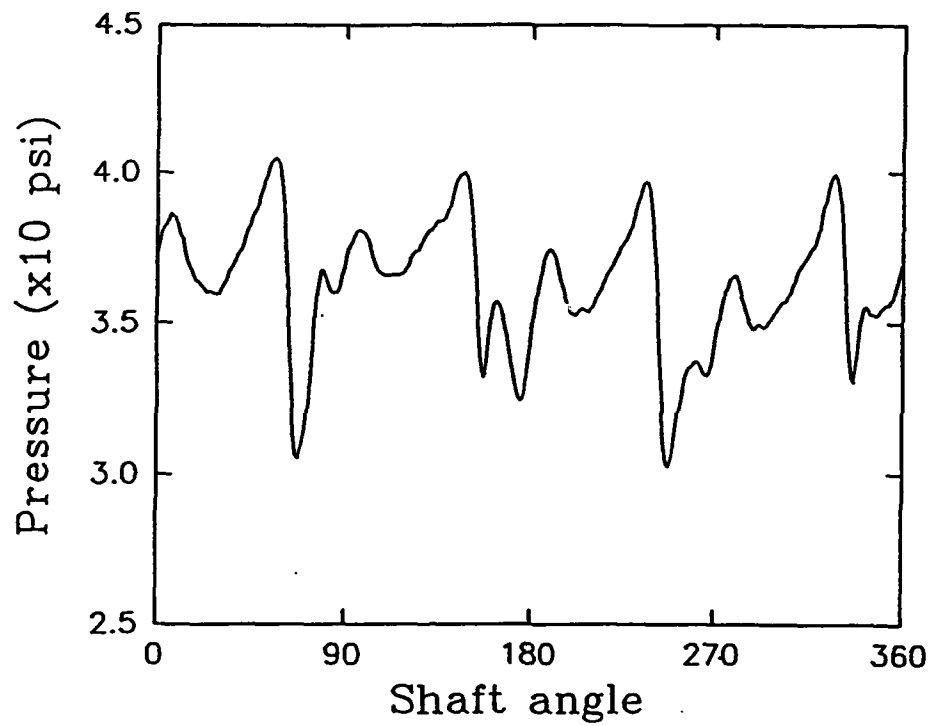
Figure 5(b)   Pressure Distribution and Frequency Spectra Obtained
at 3510 rpm at Location 2.
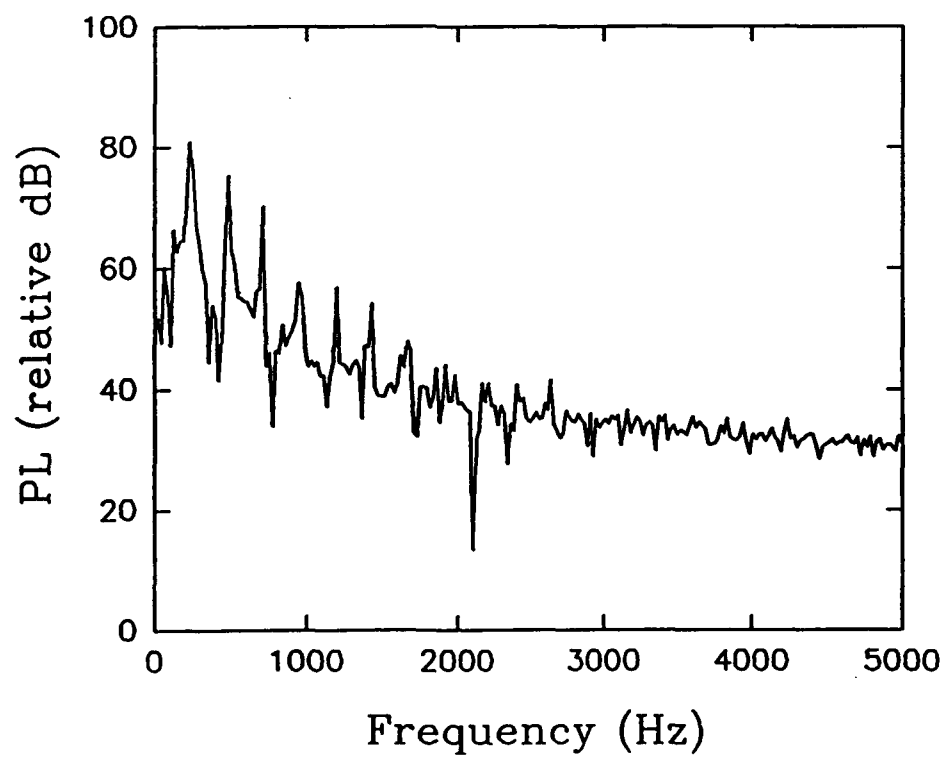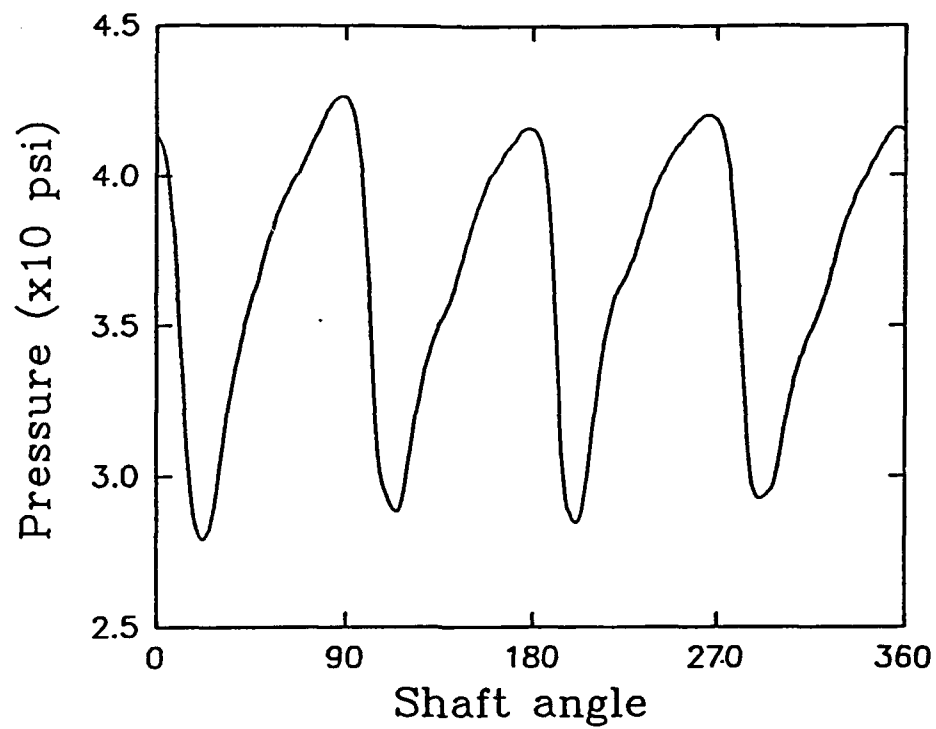
Figure 5(c)   Pressure Distribution and Frequency Spectra Obtained
at 3510 rpm at Location 3.
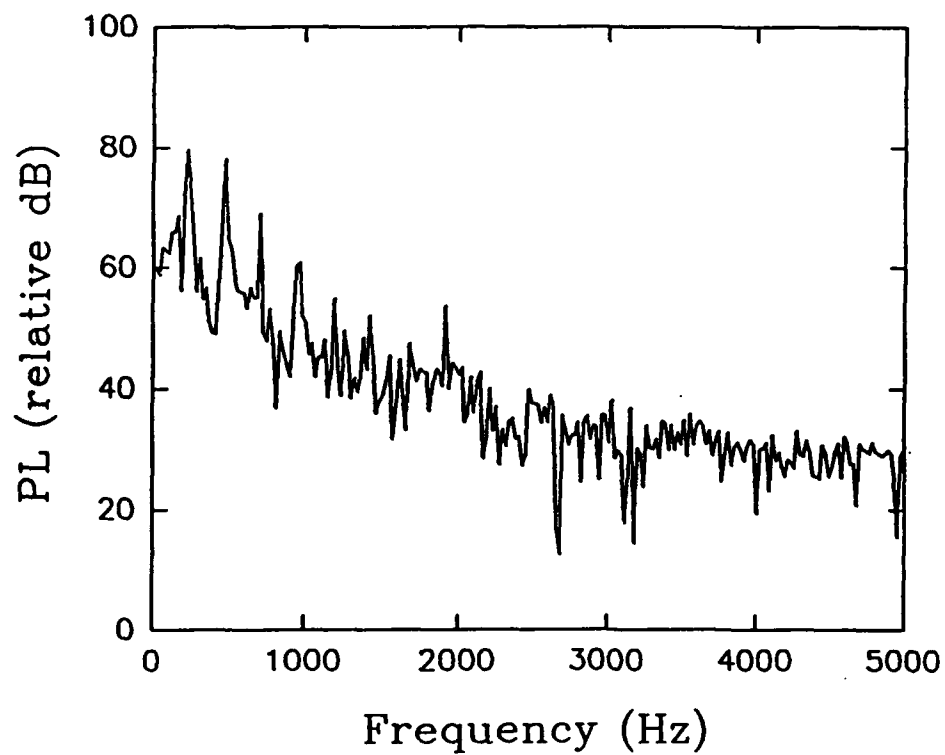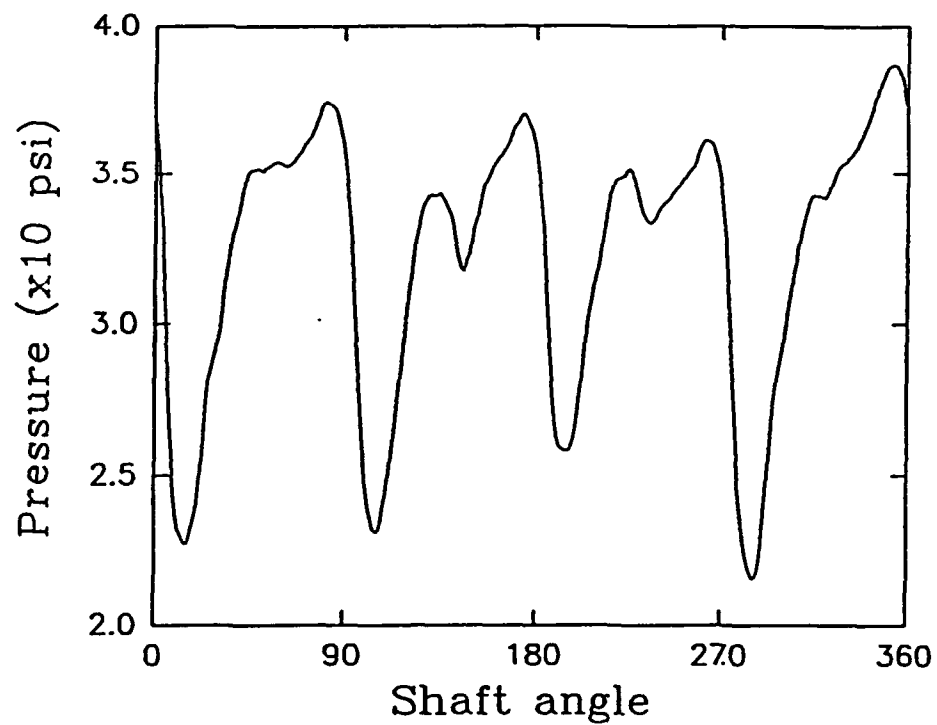
Figure 5(d)   Pressure Distribution and Frequency Spectra Obtained
               at 3510 rpm at Location 4.
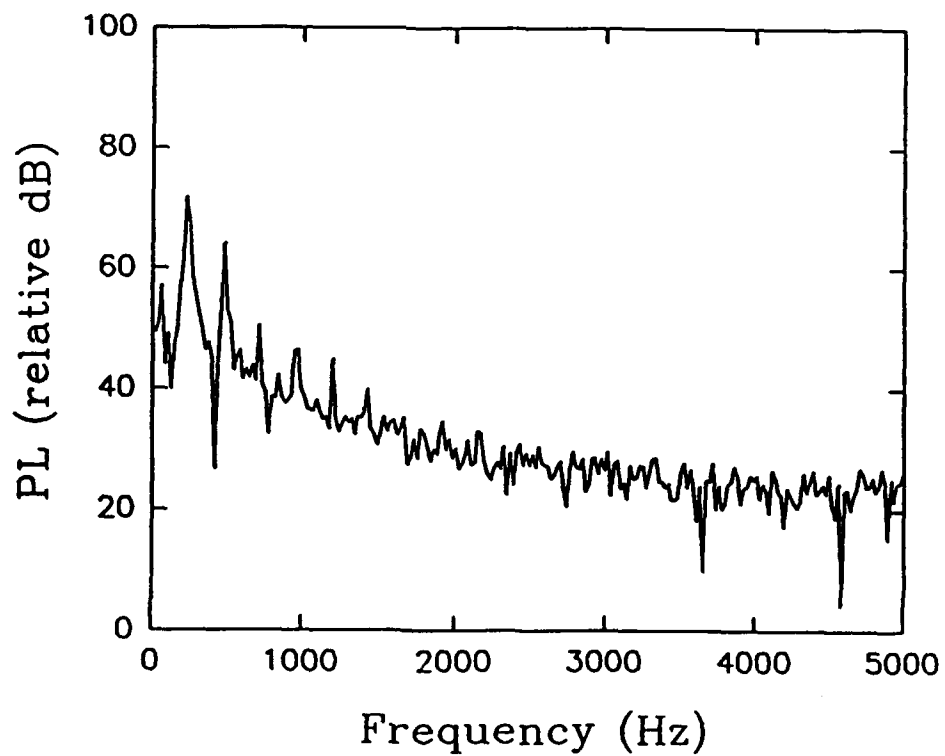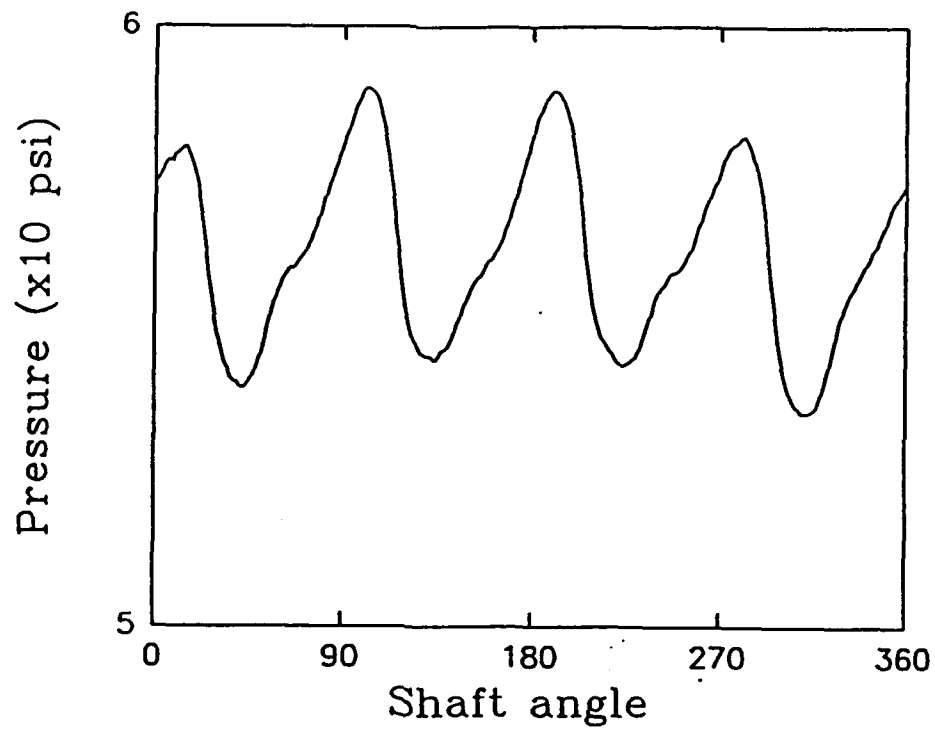
Figure 5(e)   Pressure Distribution and Frequency Spectra Obtained at 3510 rpm at Location 5.
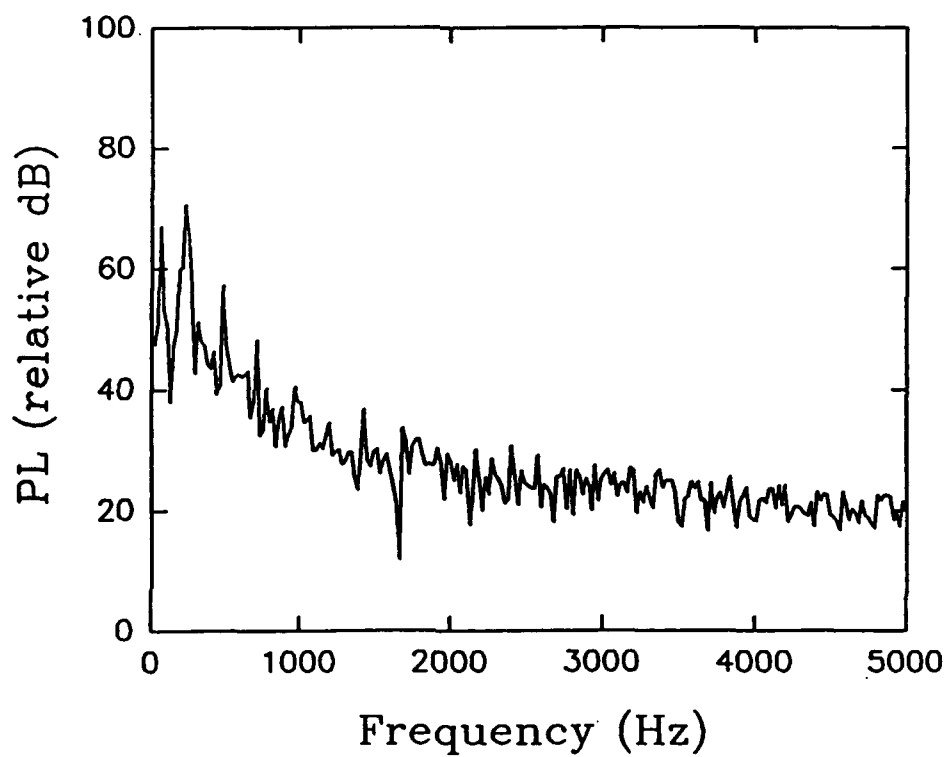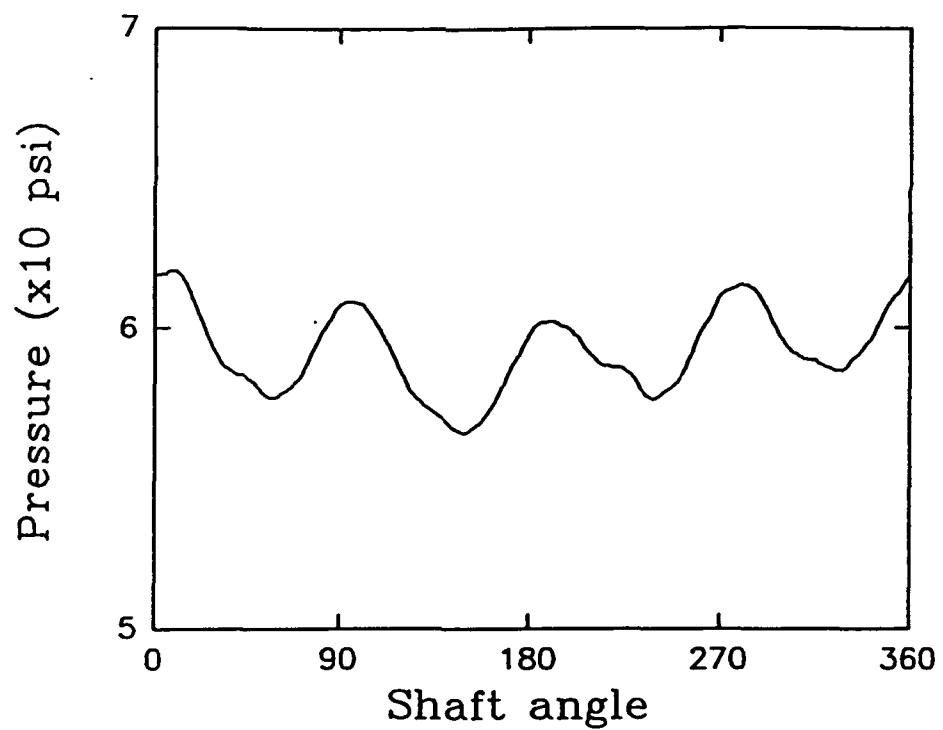
Figure 5(f)   Pressure Distribution and Frequency Spectra Obtained
               at 3510 rpm at Location 6.
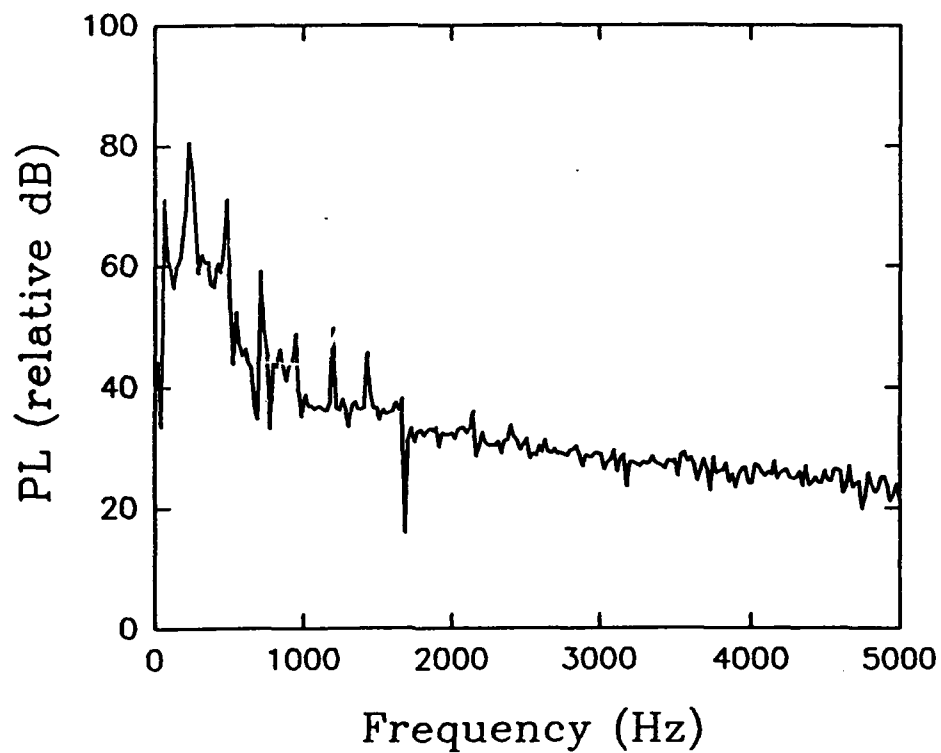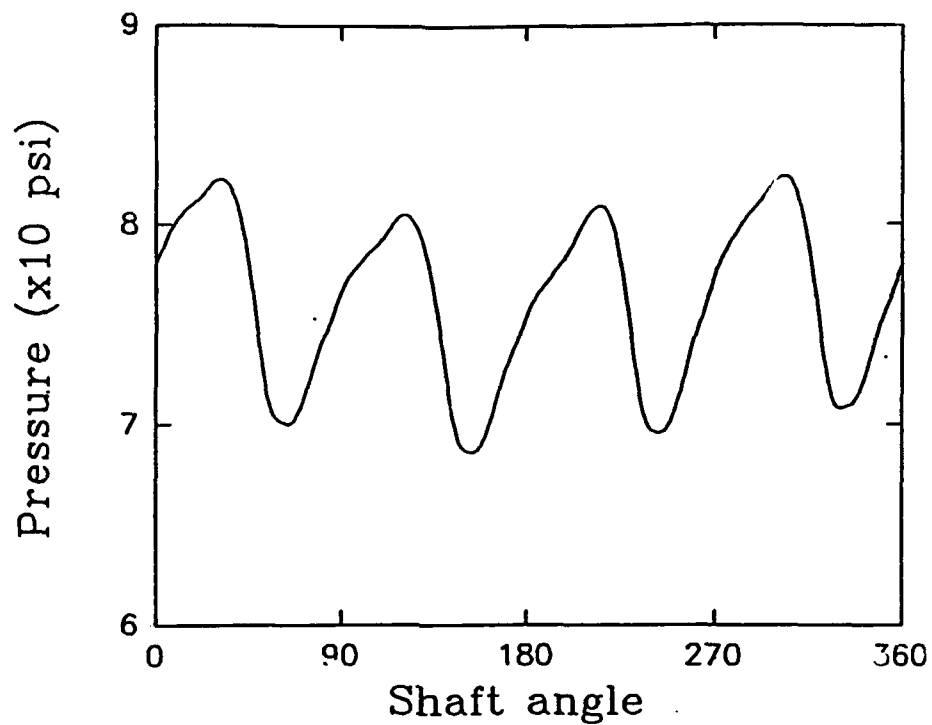
Figure 5(g)   Pressure Distribution and Frequency Spectra Obtained
at 3510 rpm at Location 7.
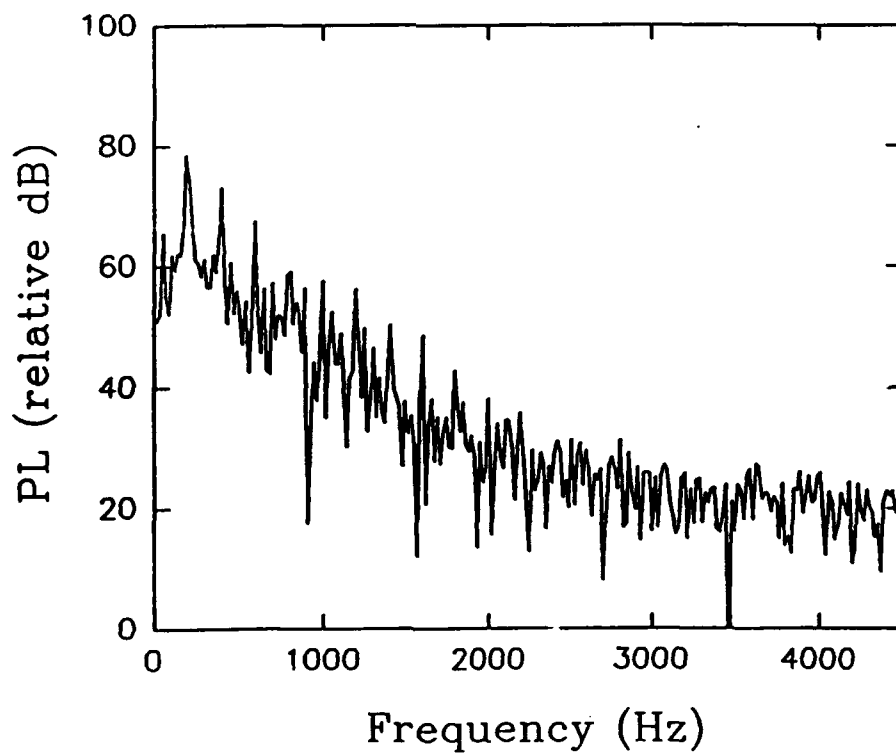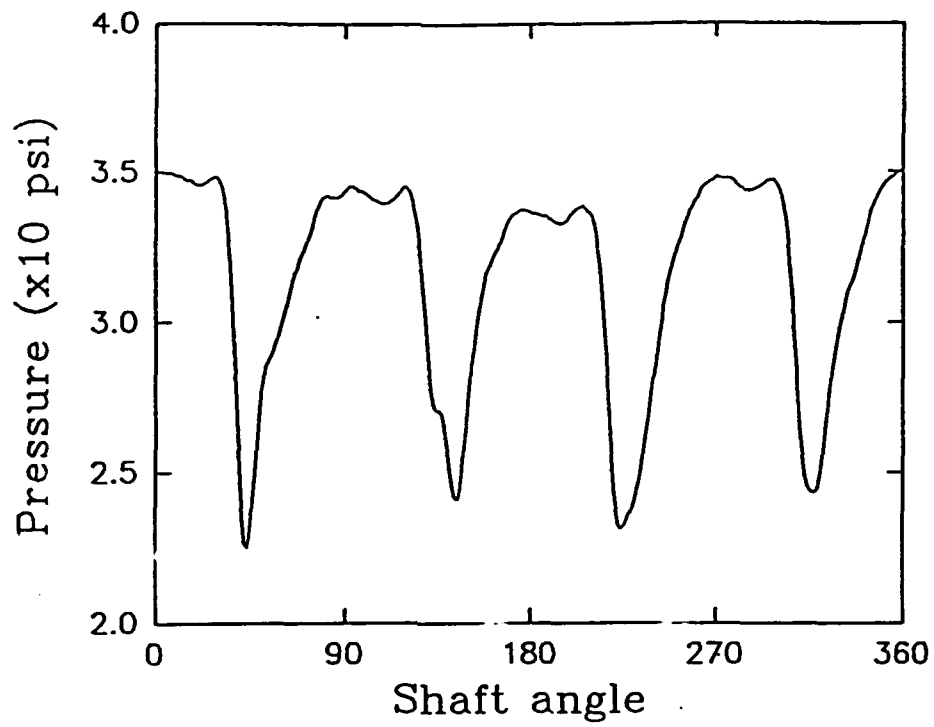
Figure 6(a)   Pressure Distribution and Frequency Spectra Obtained
at 2920 rpm at Location 1.
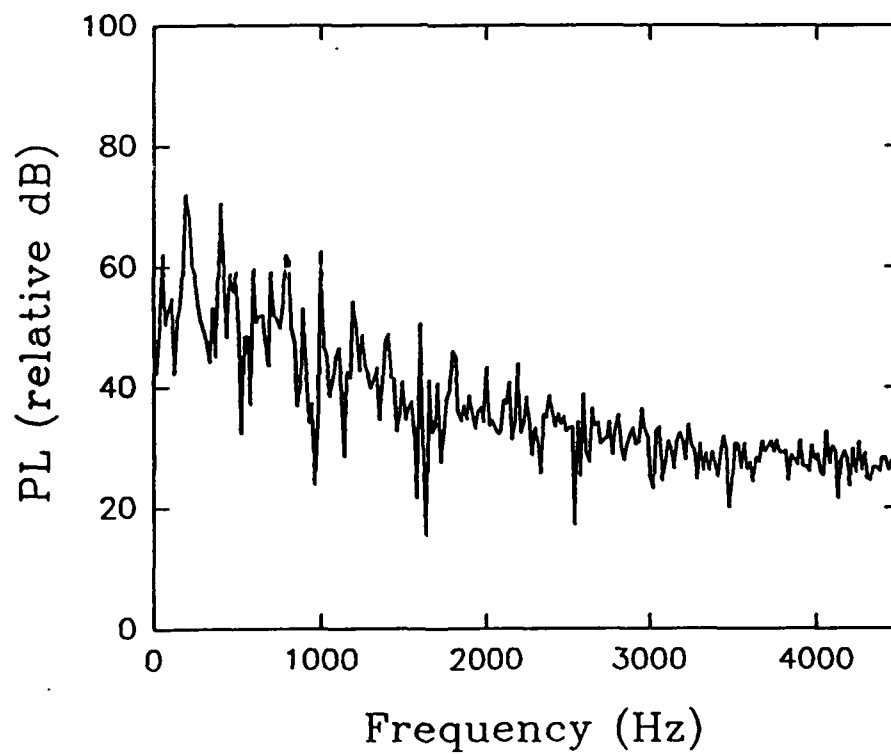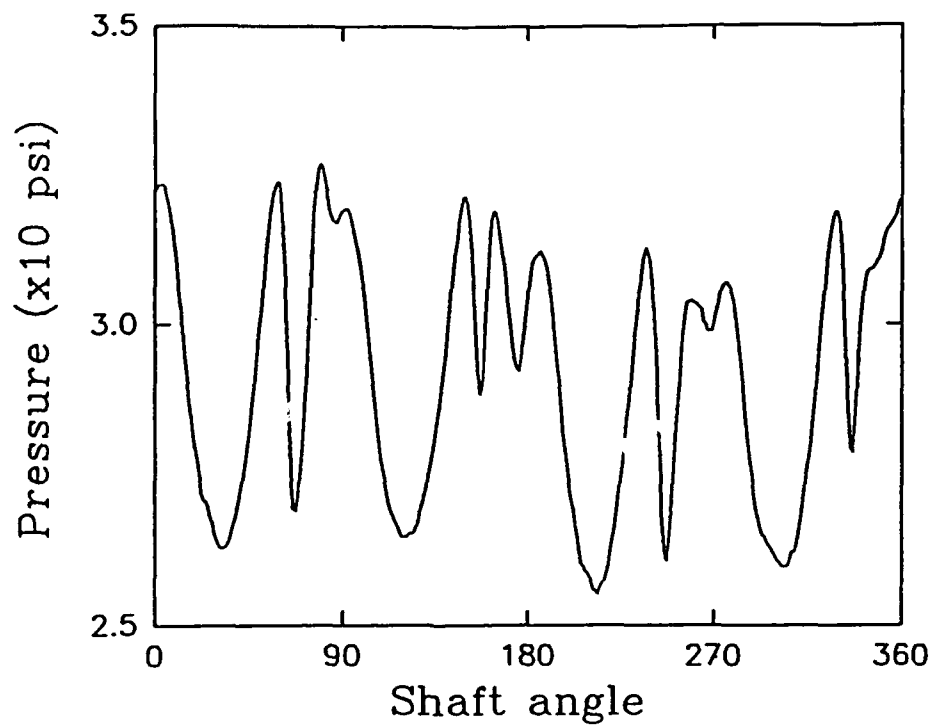
Figure 6(b)   Pressure Distribution and Frequency Spectra Obtained
at 2920 rpm at Location 2.
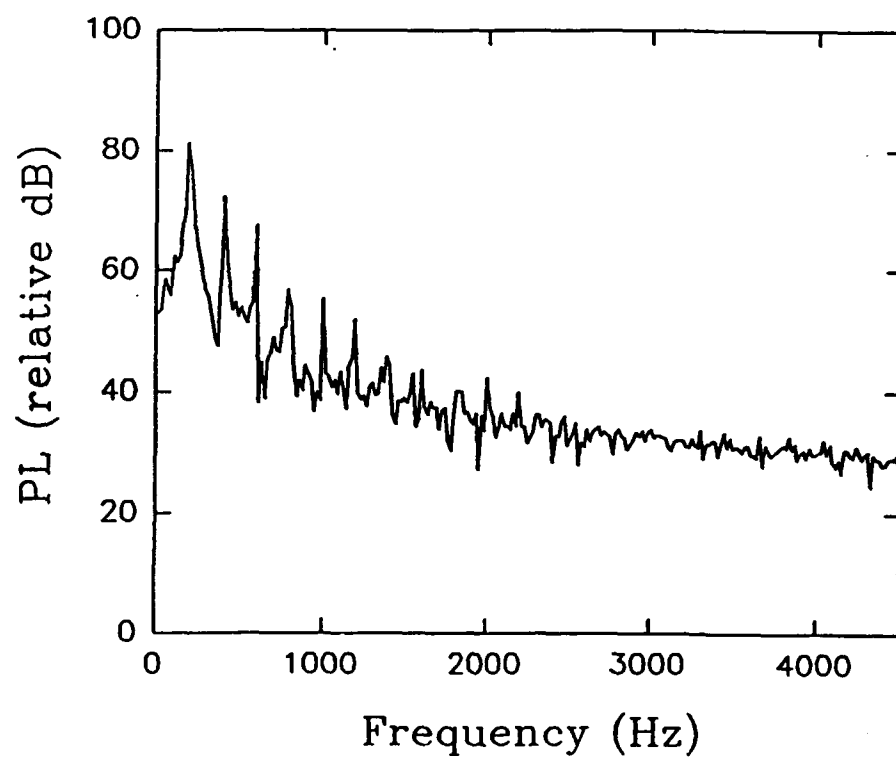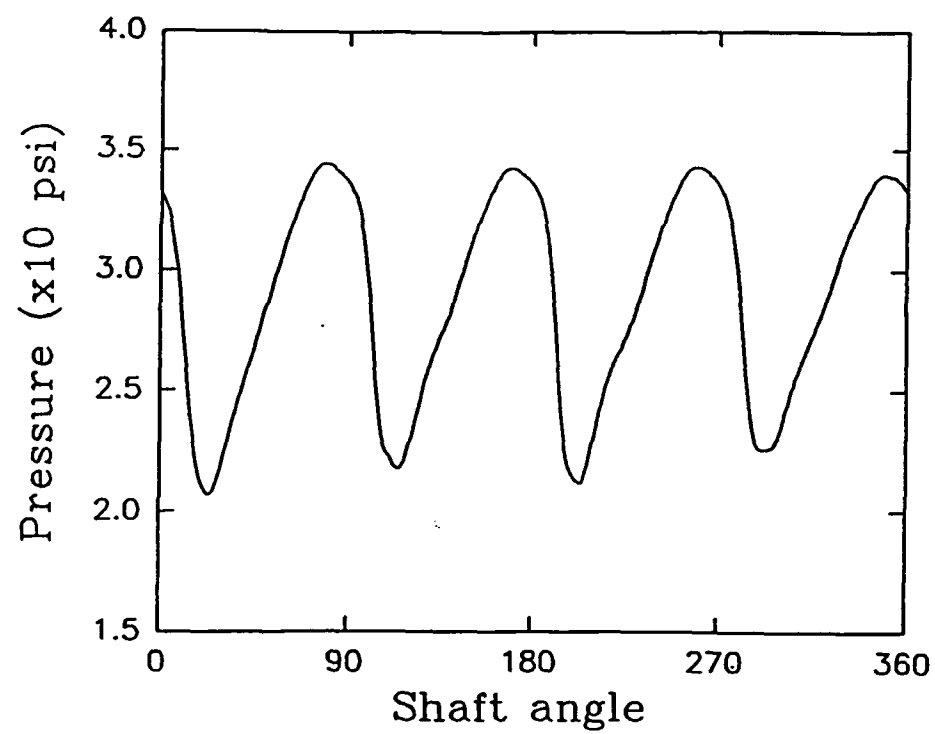
Figure 6(c)   Pressure Distribution and Frequency Spectra Obtained
at 2920 rpm at Location 3.
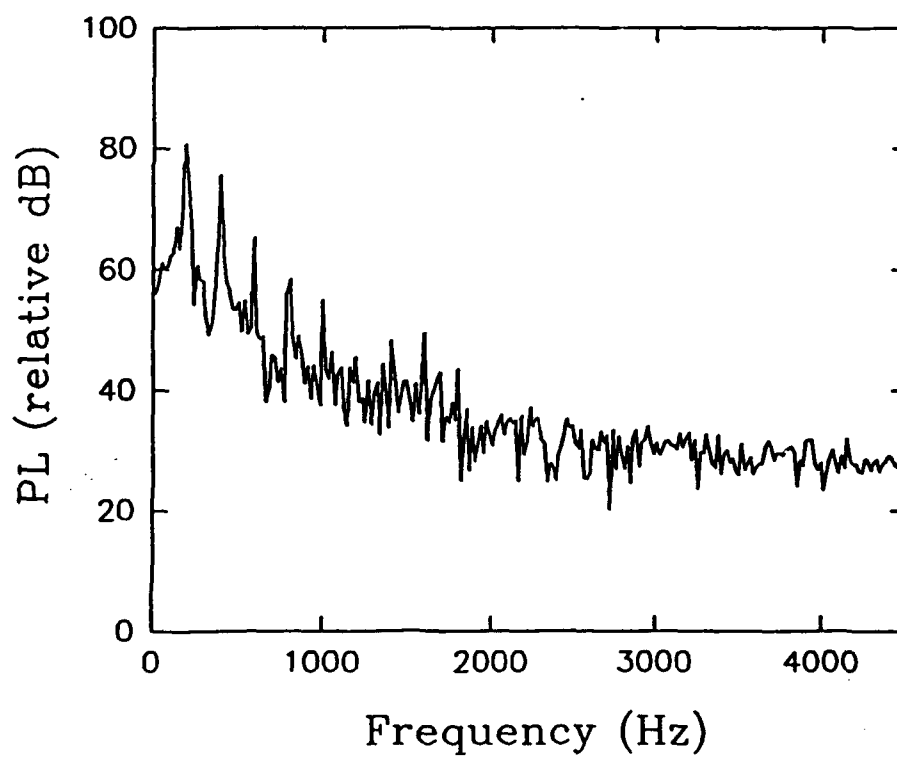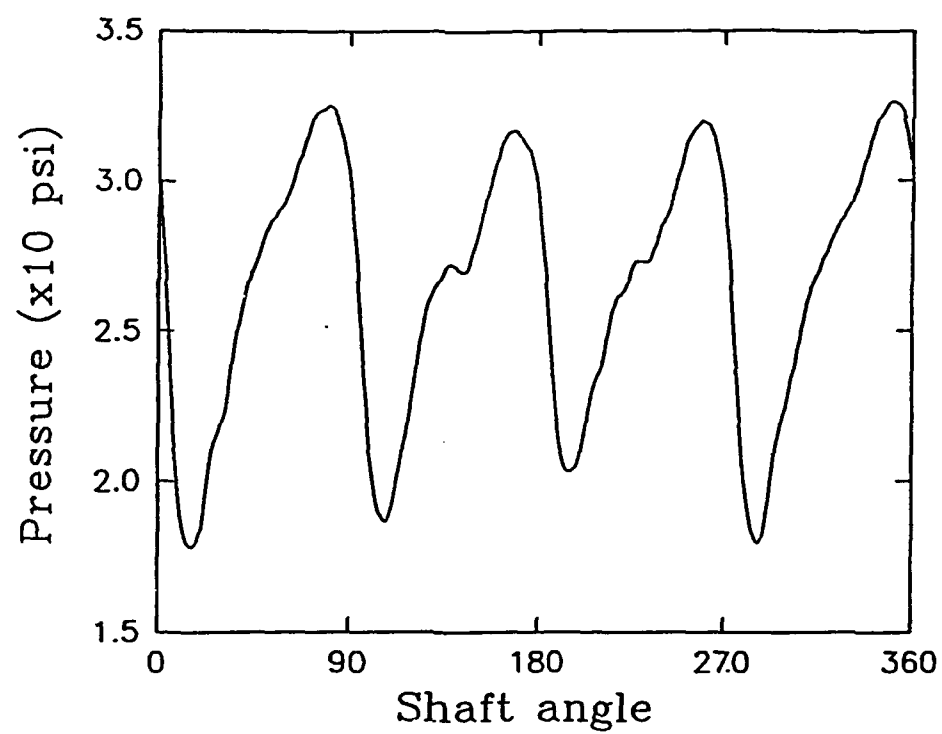
Figure 6(d)   Pressure Distribution and Frequency Spectra Obtained
at 2920 rpm at Location 4.
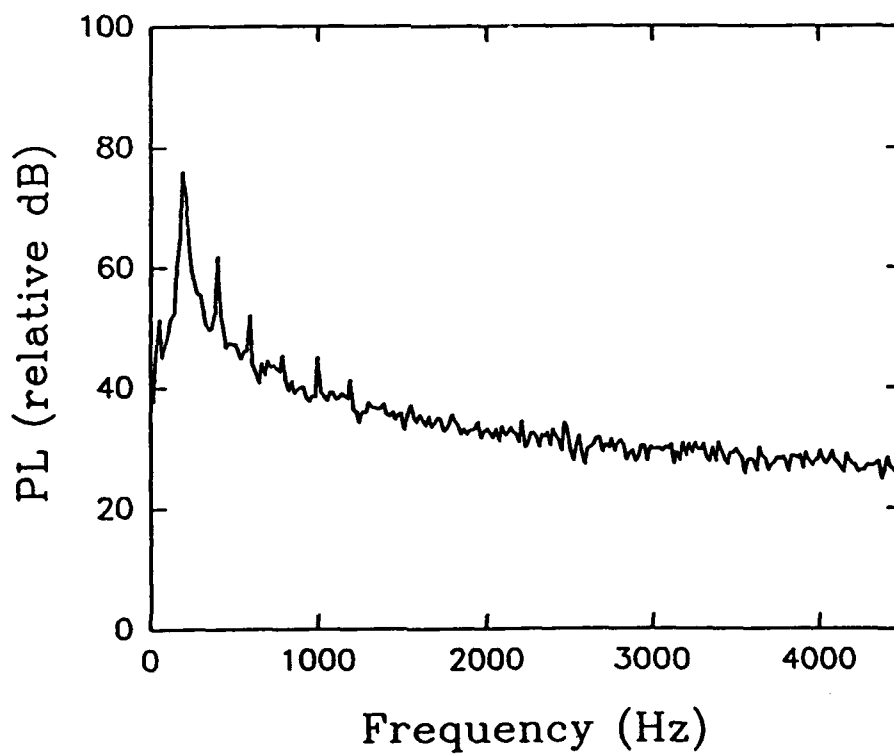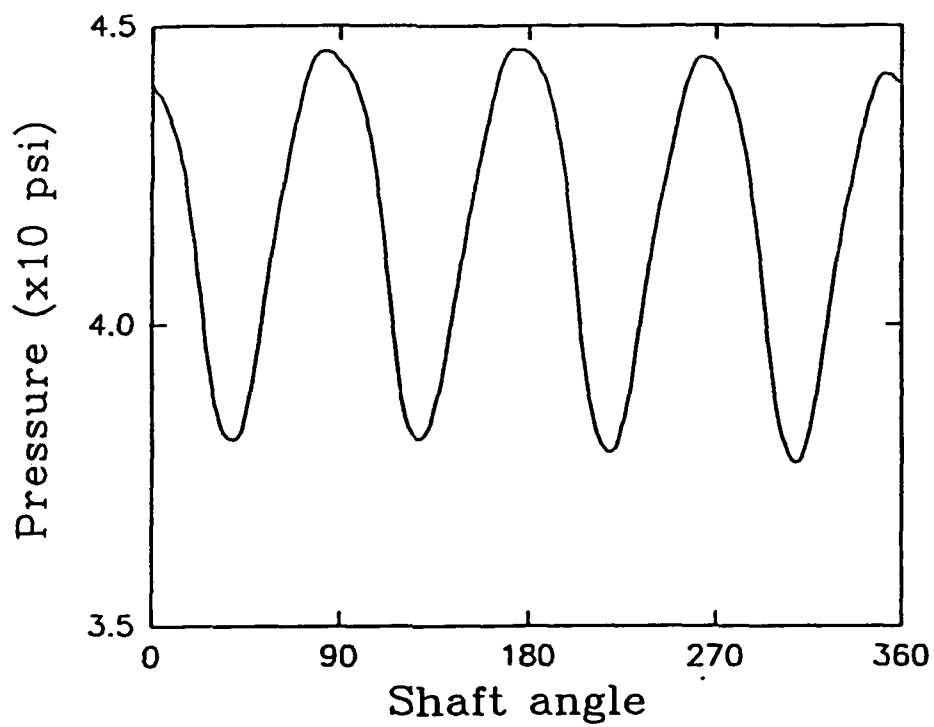
Figure 6(e)   Pressure Distribution and Frequency Spectra Obtained
               at 2920 rpm at Location 5.
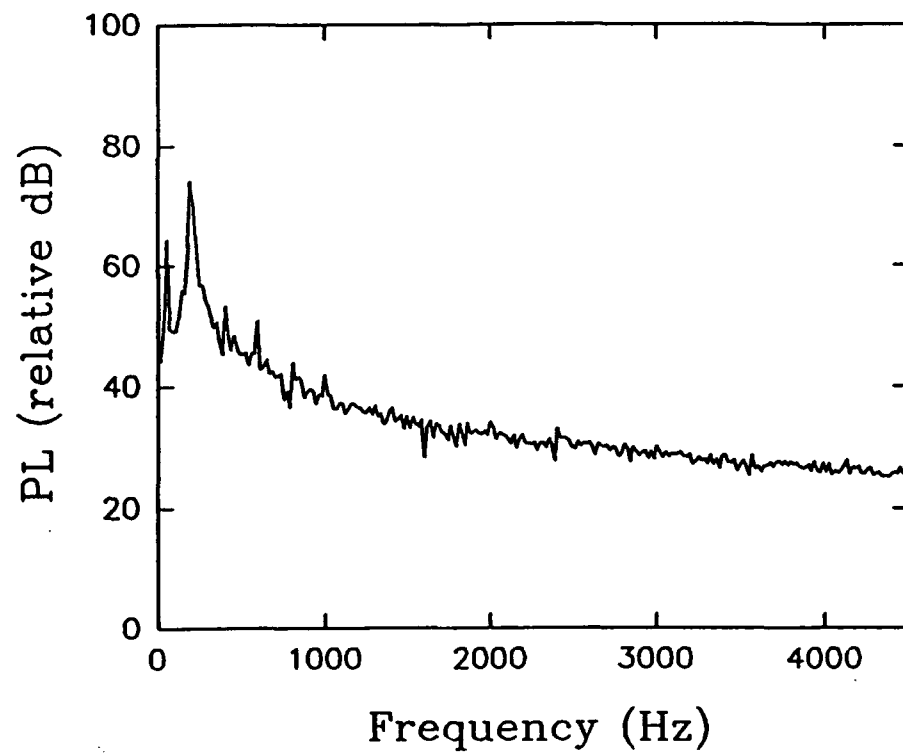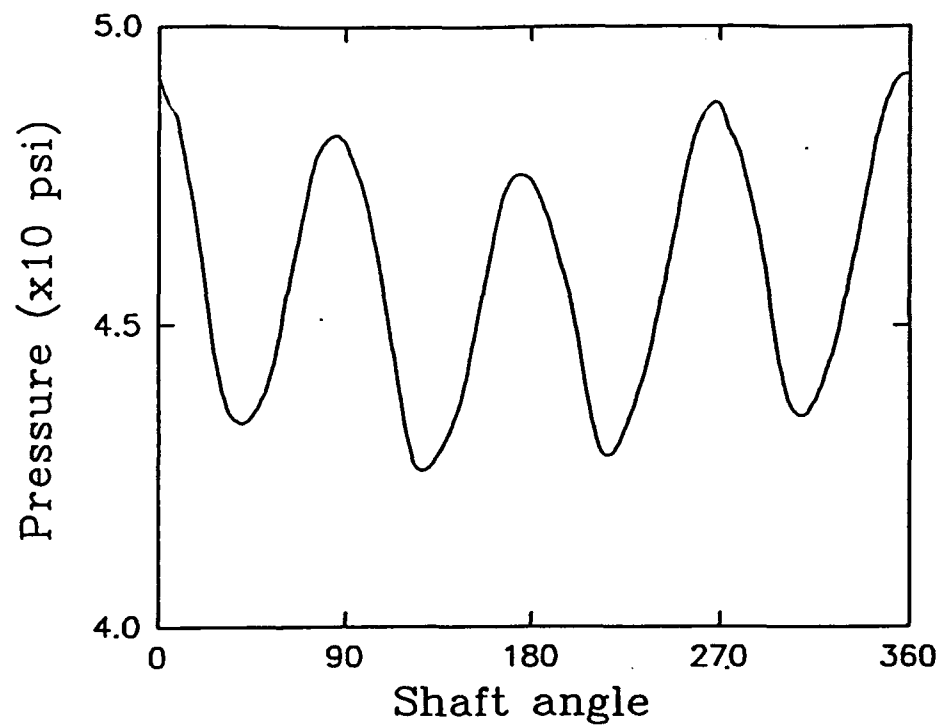
Figure 6(f)   Pressure Distribution and Frequency Spectra Obtained
at 2920 rpm at Location 6.
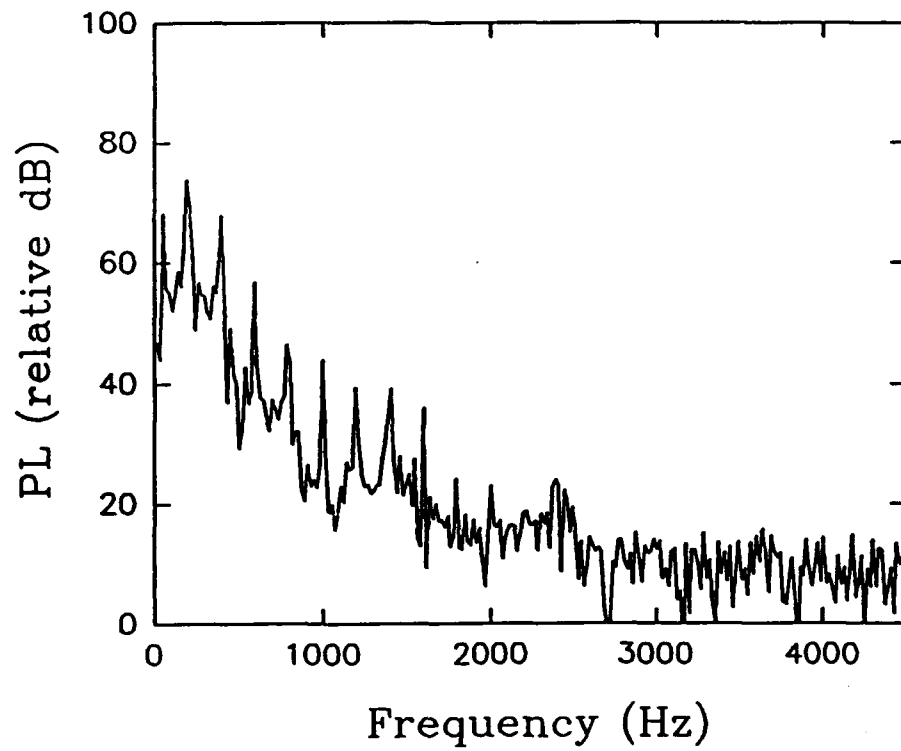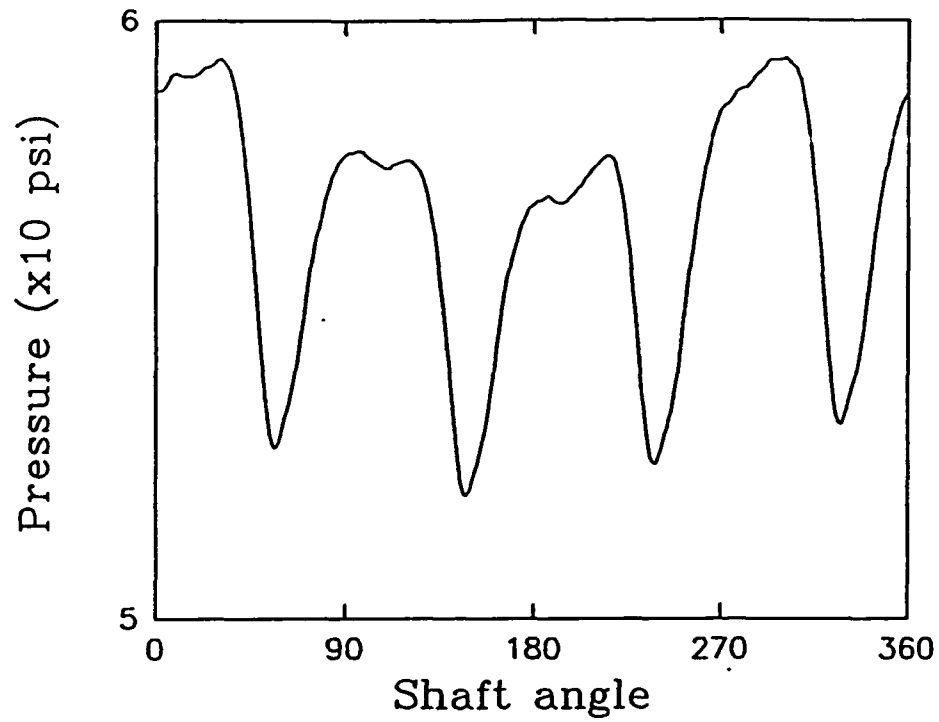
Figure 6(g)   Pressure Distribution and Frequency Spectra Obtained
at 2920 rpm at Location 7.
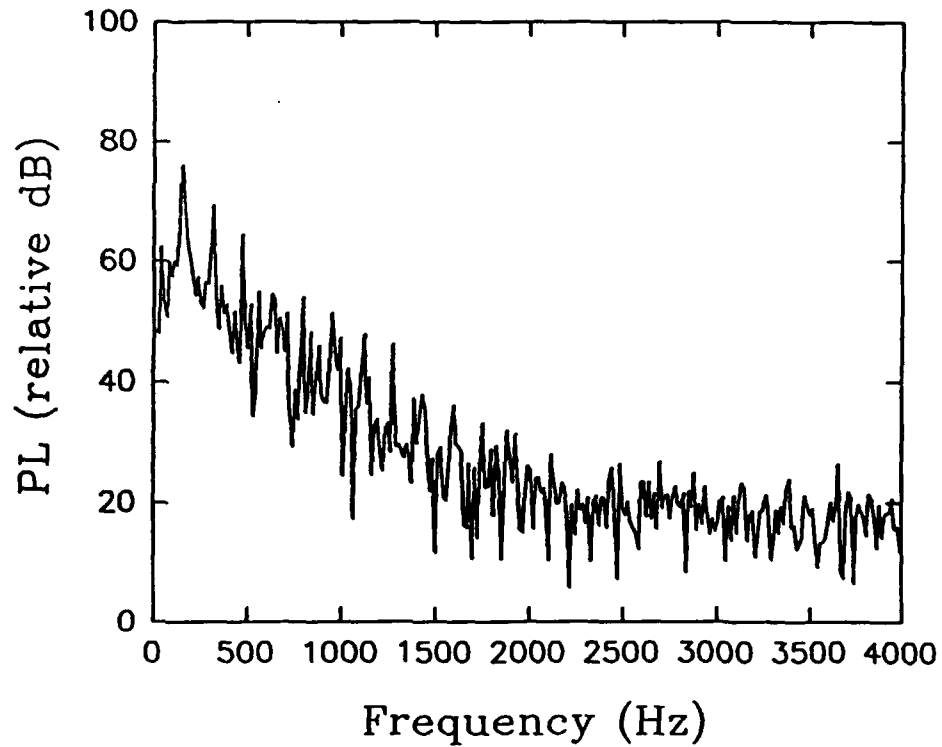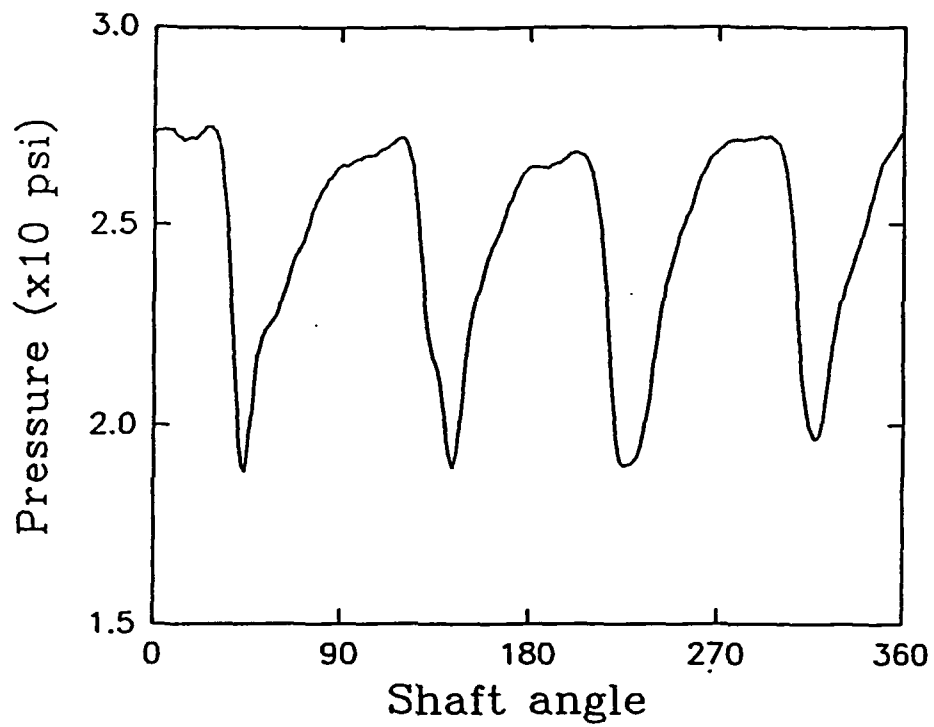
Figure 7(a)   Pressure Distribution and Frequency Spectra Obtained
                at 2340 rpm at Location 1.
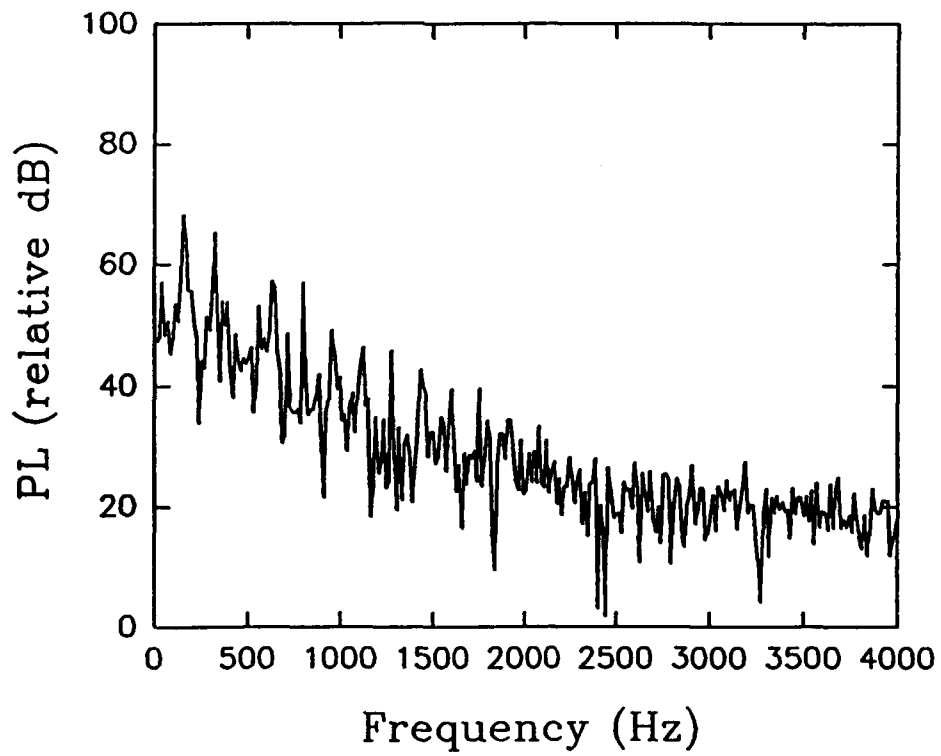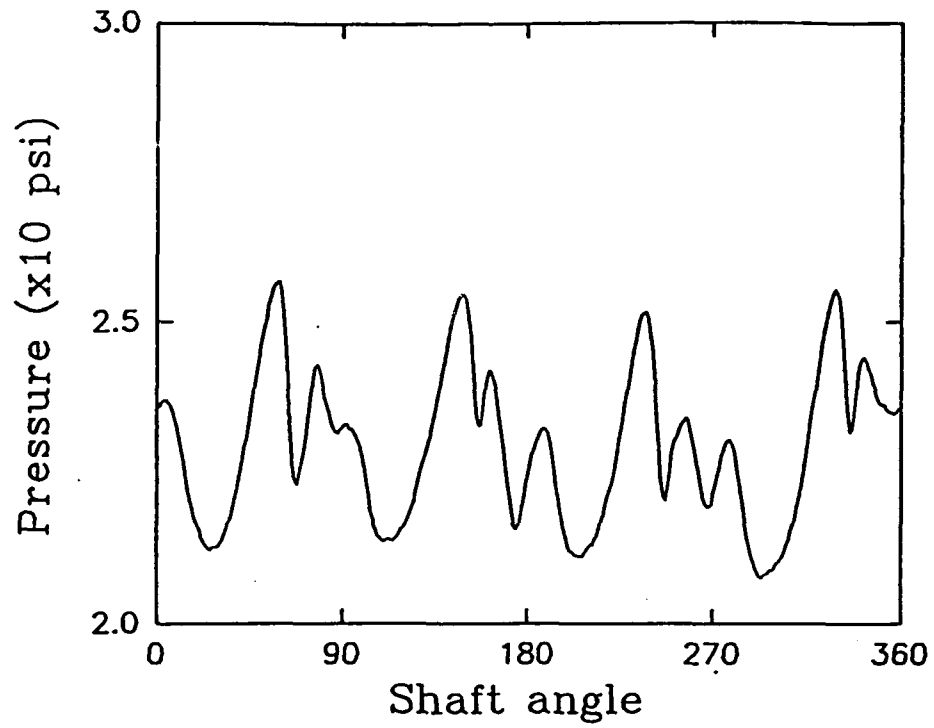
Figure 7(b)   Pressure Distribution and Frequency Spectra Obtained
at 2340 rpm at Location 2.
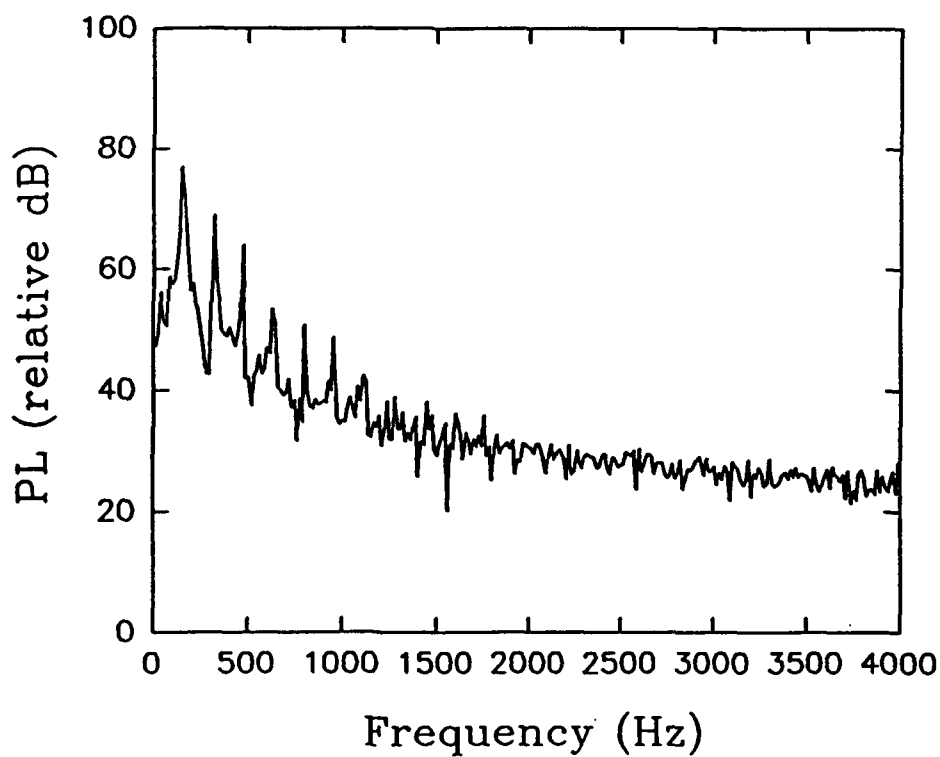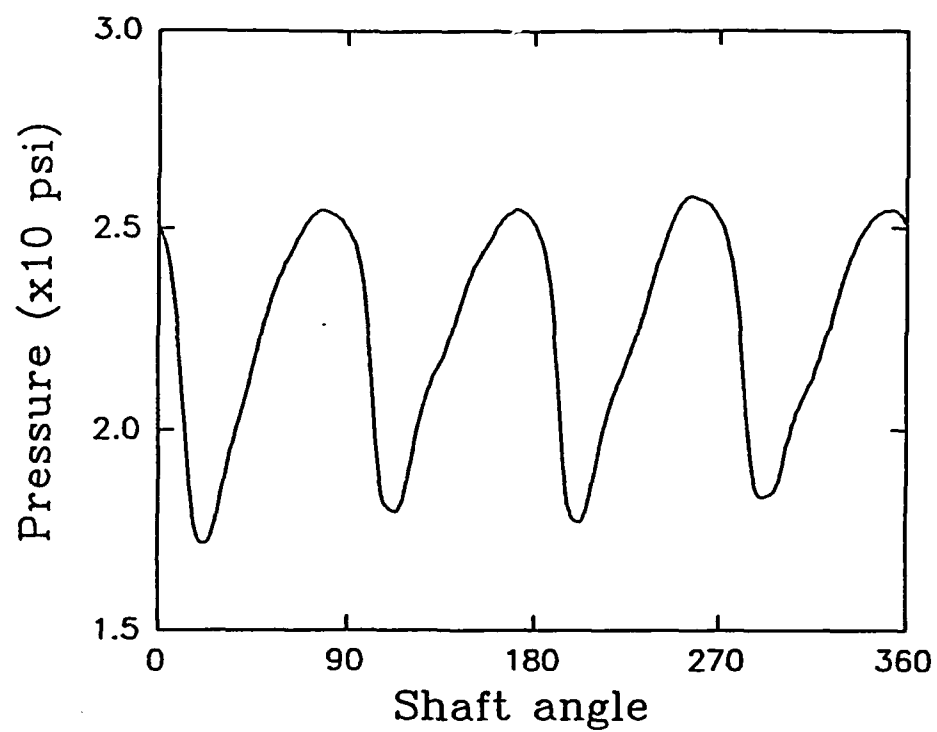
Figure 7(c)   Pressure Distribution and Frequency Spectra Obtained
at 2340 rpm at Location 3.
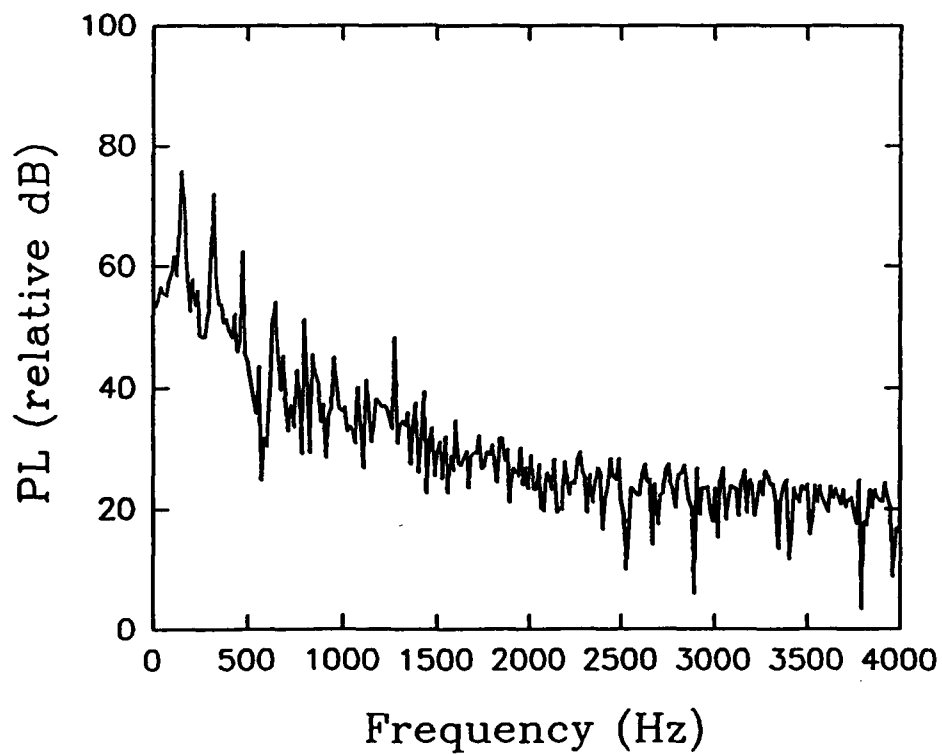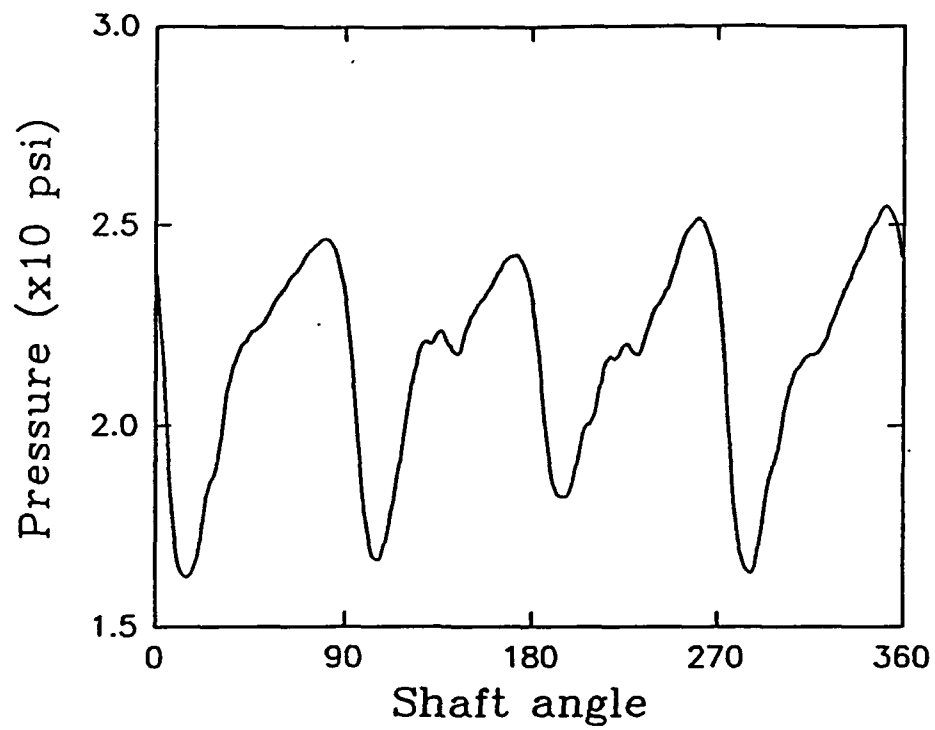
Figure 7(d)   Pressure Distribution and Frequency Spectra Obtained
               at 2340 rpm at Location 4.
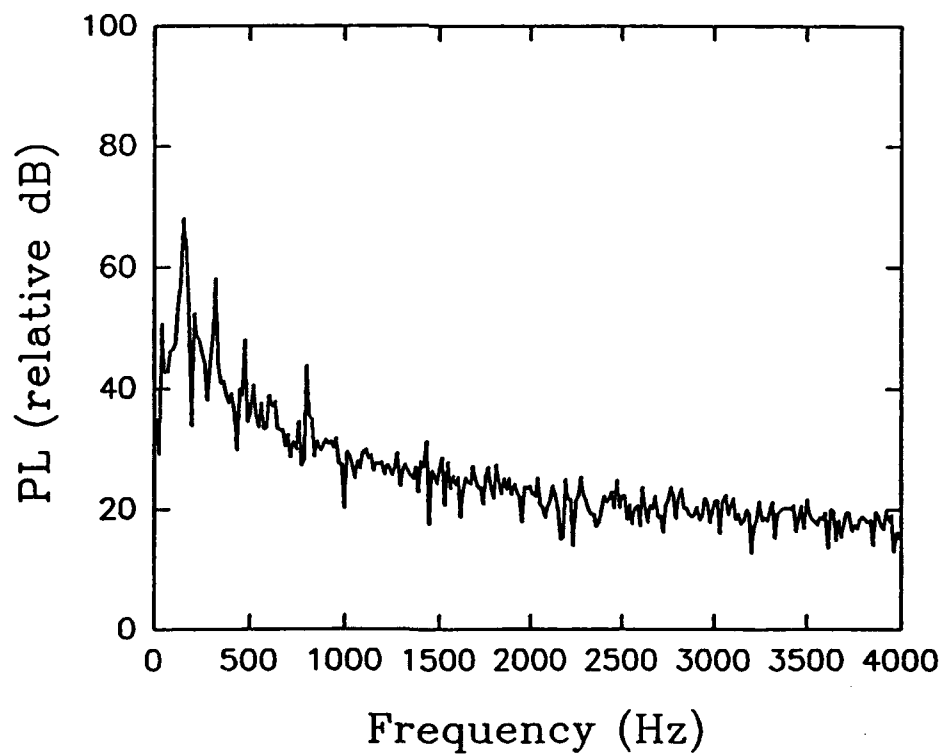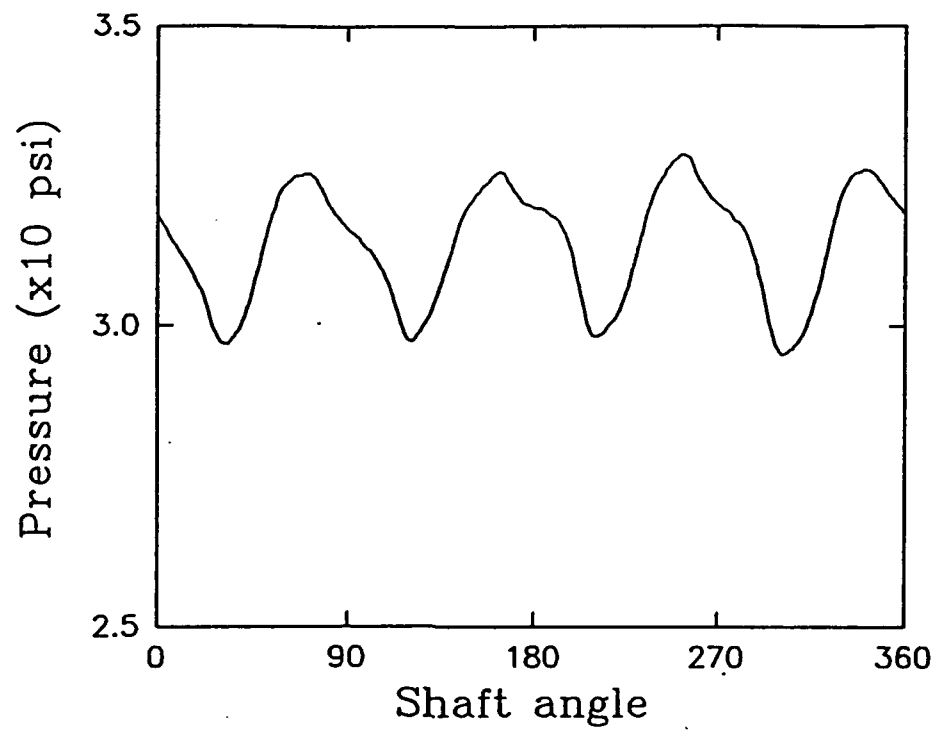
Figure 7(e)   Pressure Distribution and Frequency Spectra Obtained at 2340 rpm at Location 5.
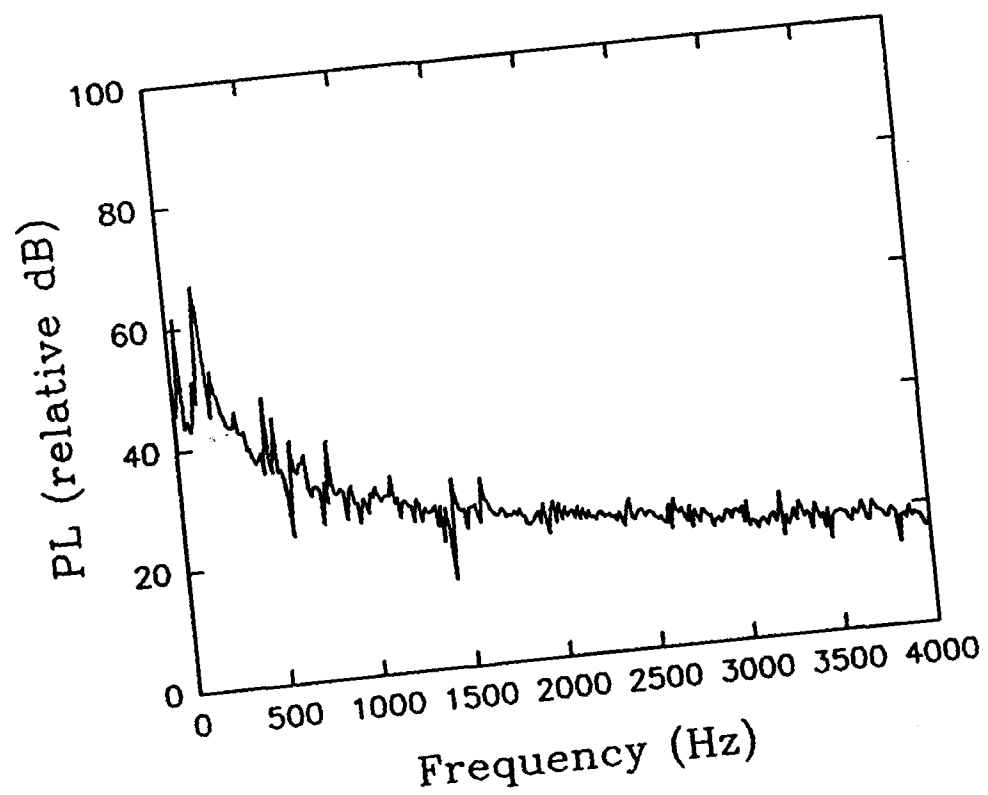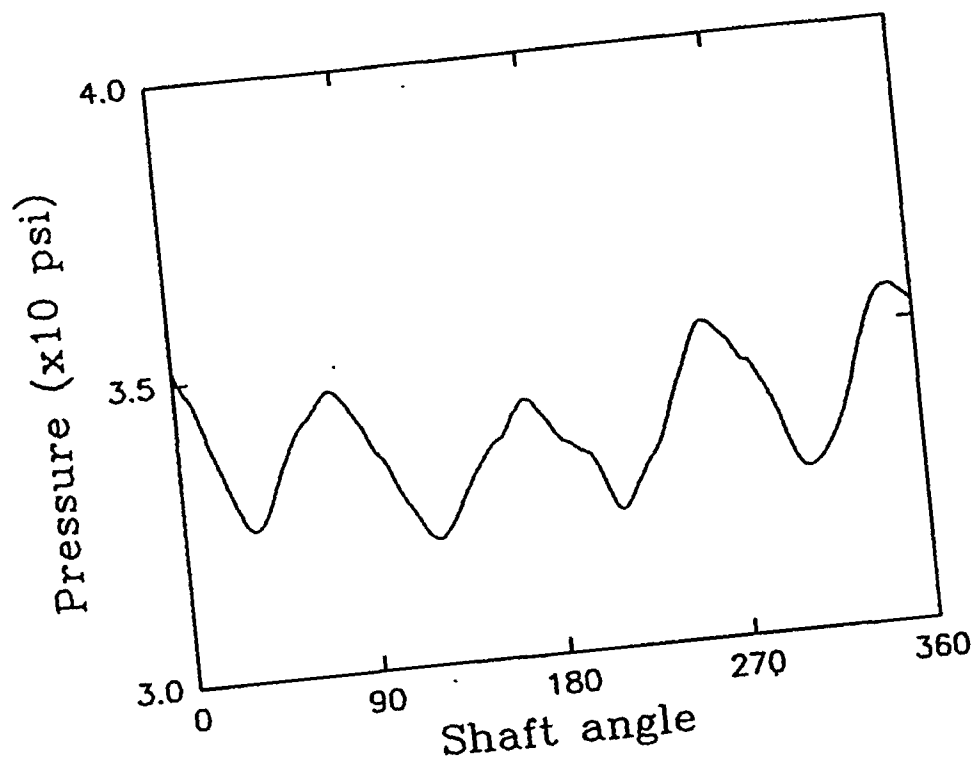
Figure 7(f)   Pressure Distribution and Frequency Spectra Obtained at 2340 rpm at Location 6.
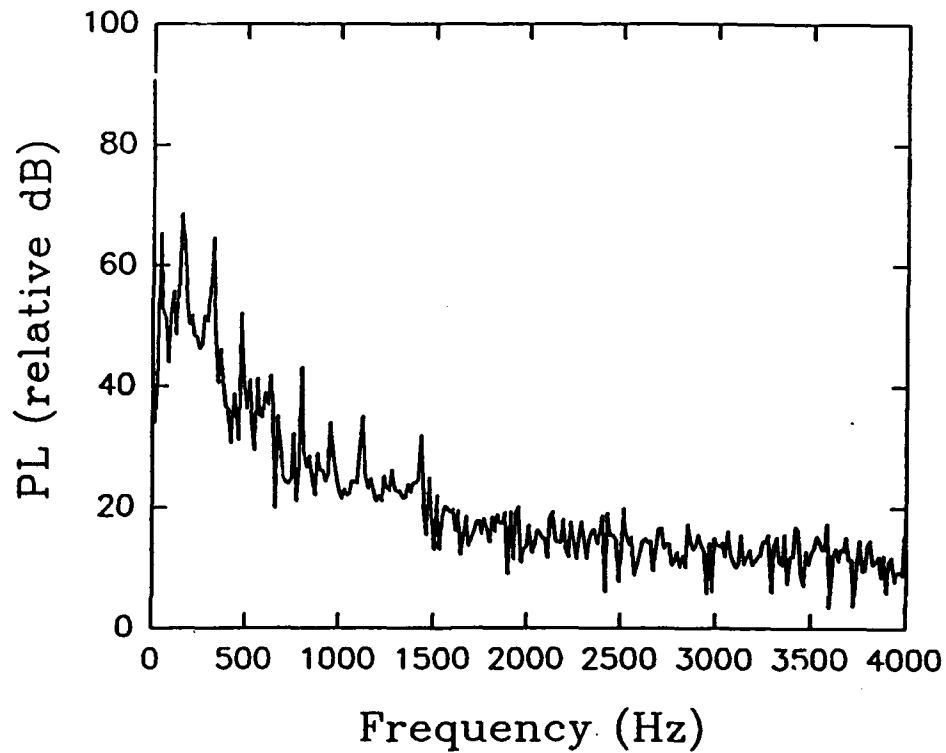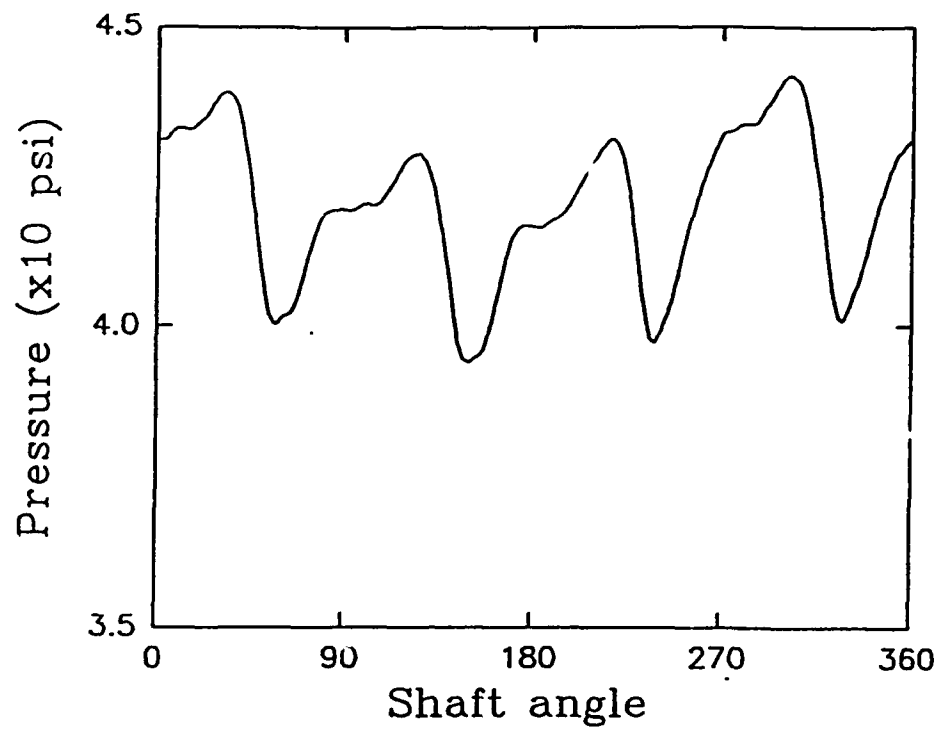
Figure 7(g)   Pressure Distribution and Frequency Spectra Obtained
at 2340 rpm at Location 7.
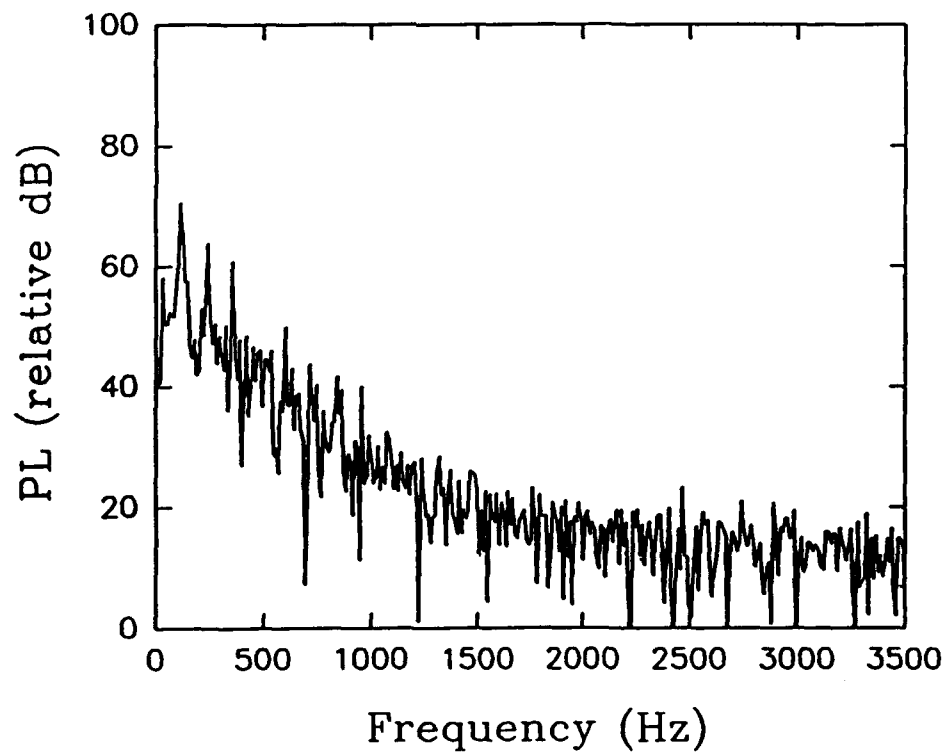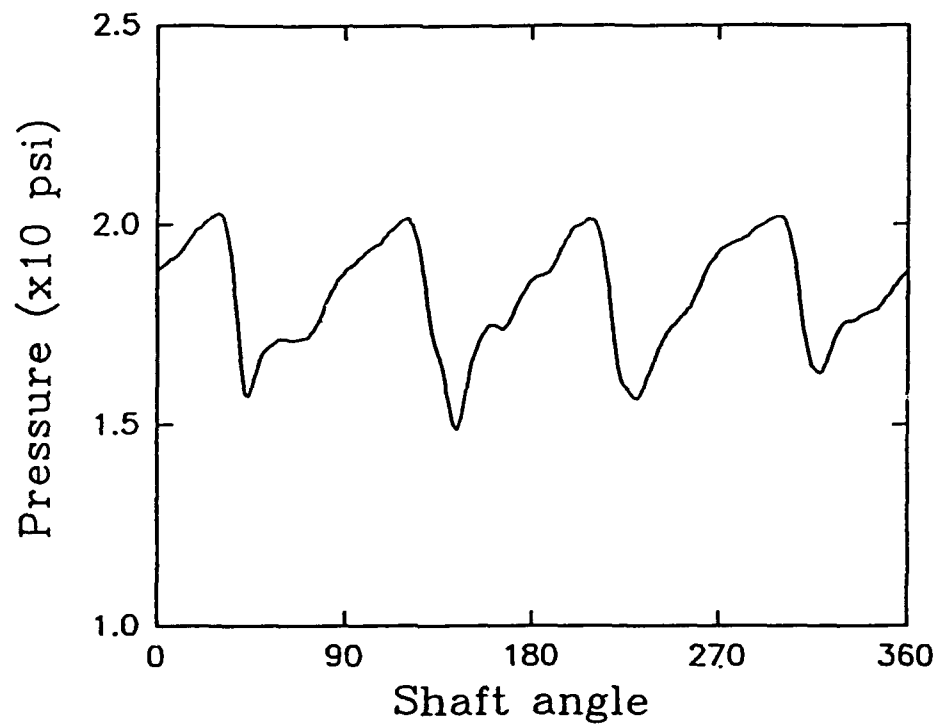
Figure 8(a)   Pressure Distribution and Frequency Spectra Obtained at 1770 rpm at Location 1.
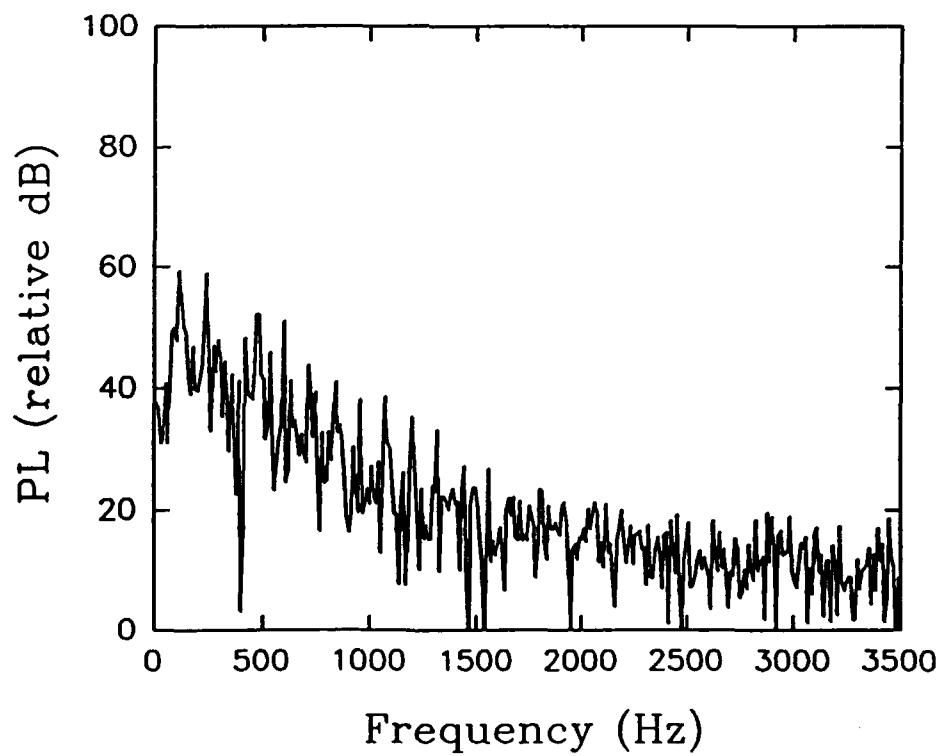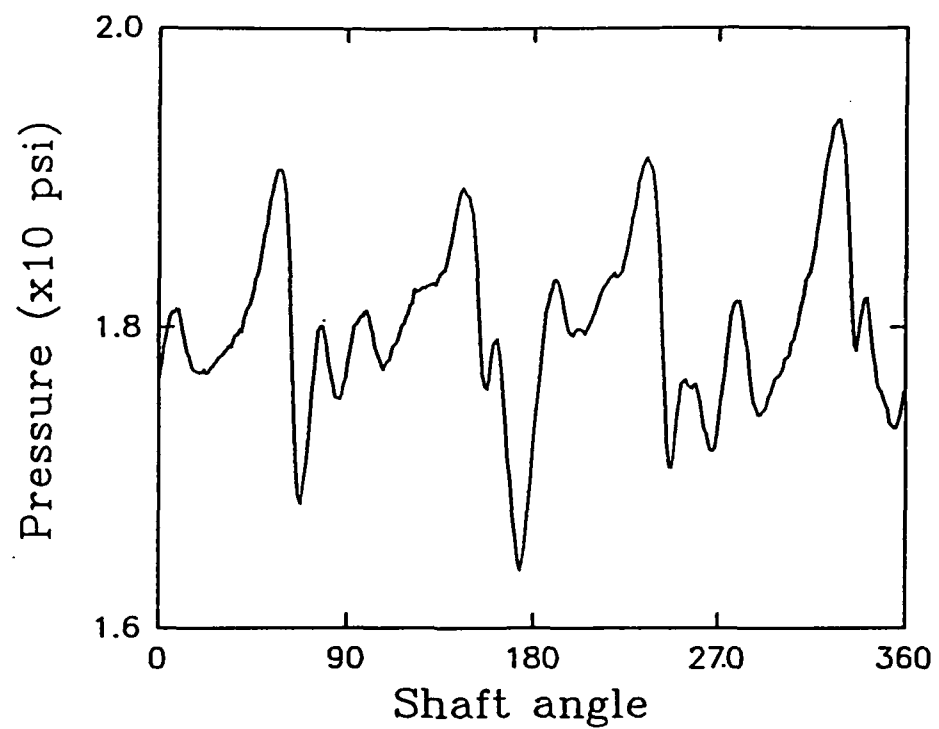
Figure 8(b)   Pressure Distribution and Frequency Spectra Obtained
at 1770 rpm at Location 2.
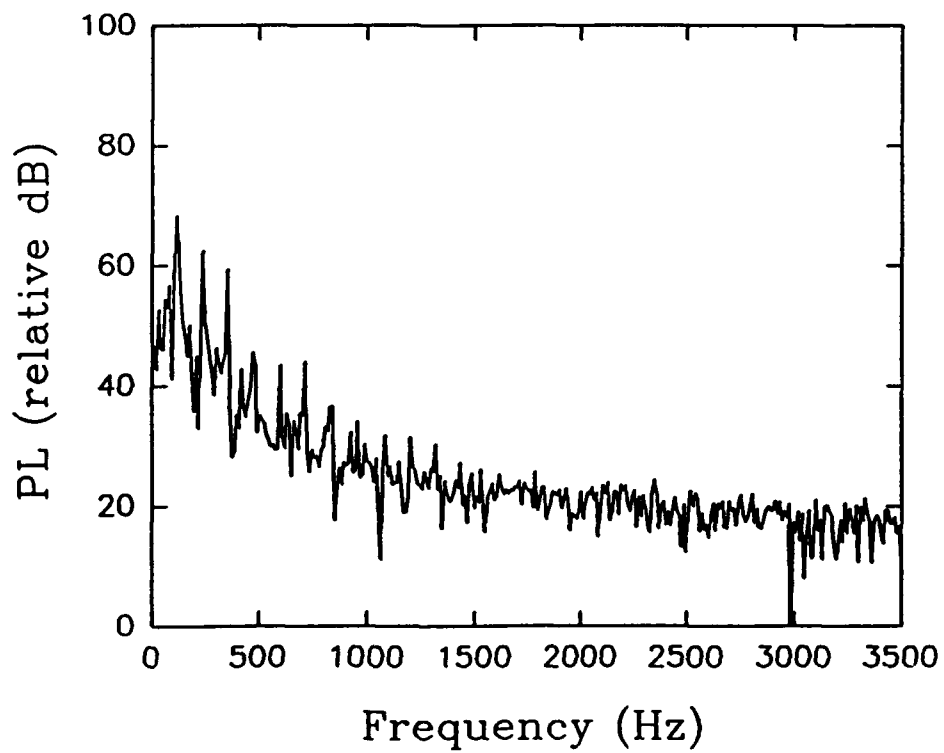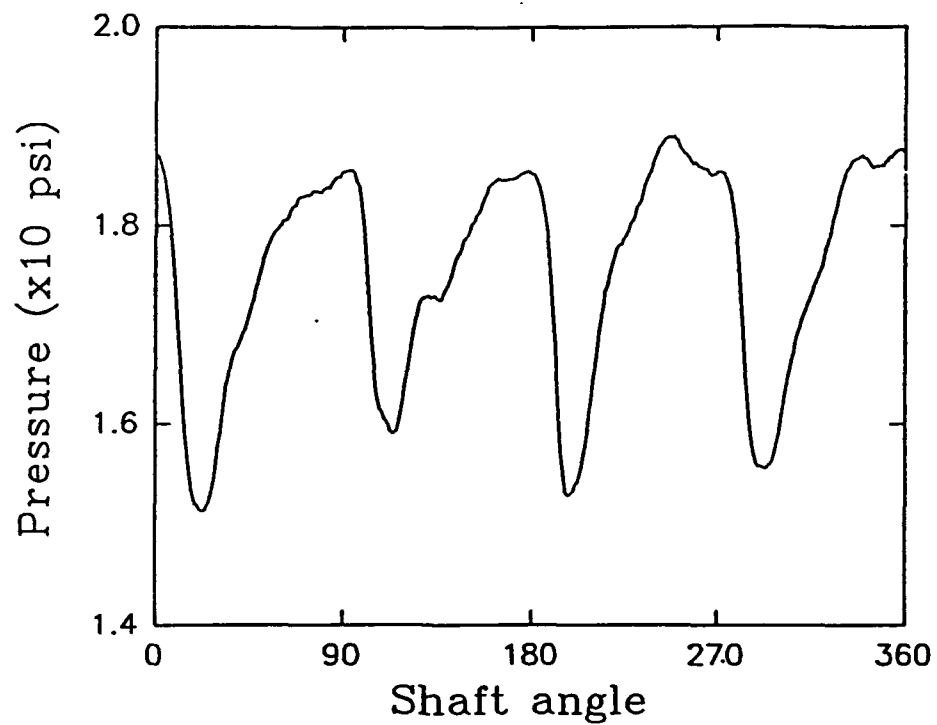
Figure 8(c)   Pressure Distribution and Frequency Spectra Obtained
at 1770 rpm at Location 3.
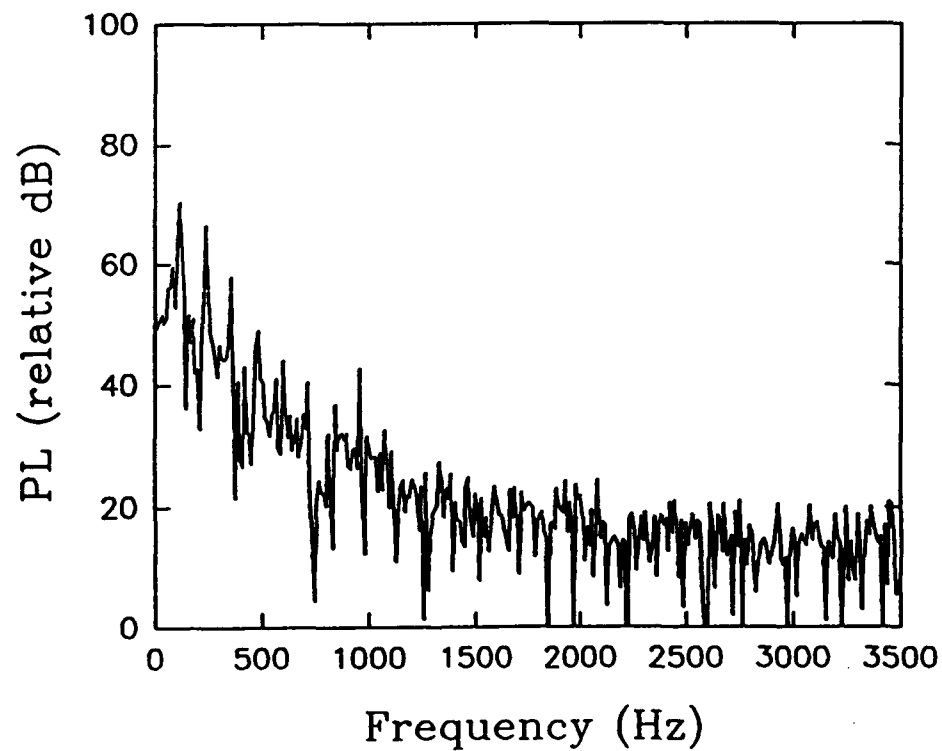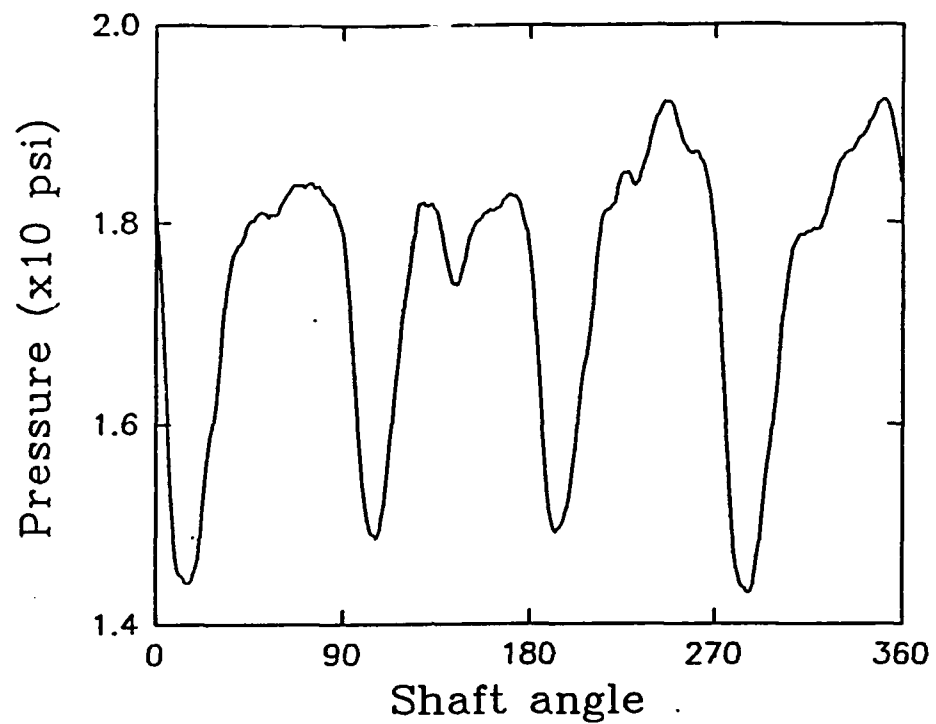
Figure 8(d)   Pressure Distribution and Frequency Spectra Obtained
at 1770 rpm at Location 4.

Figure 8(e)   Pressure Distribution and Frequency Spectra Obtained
               at 1770 rpm at Location 5.
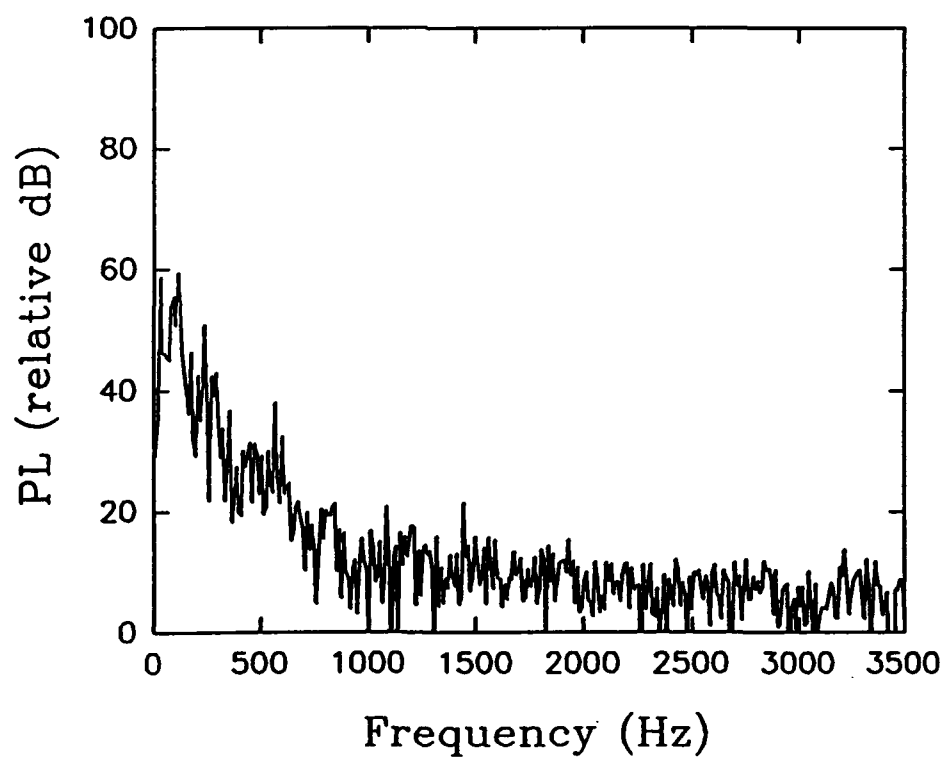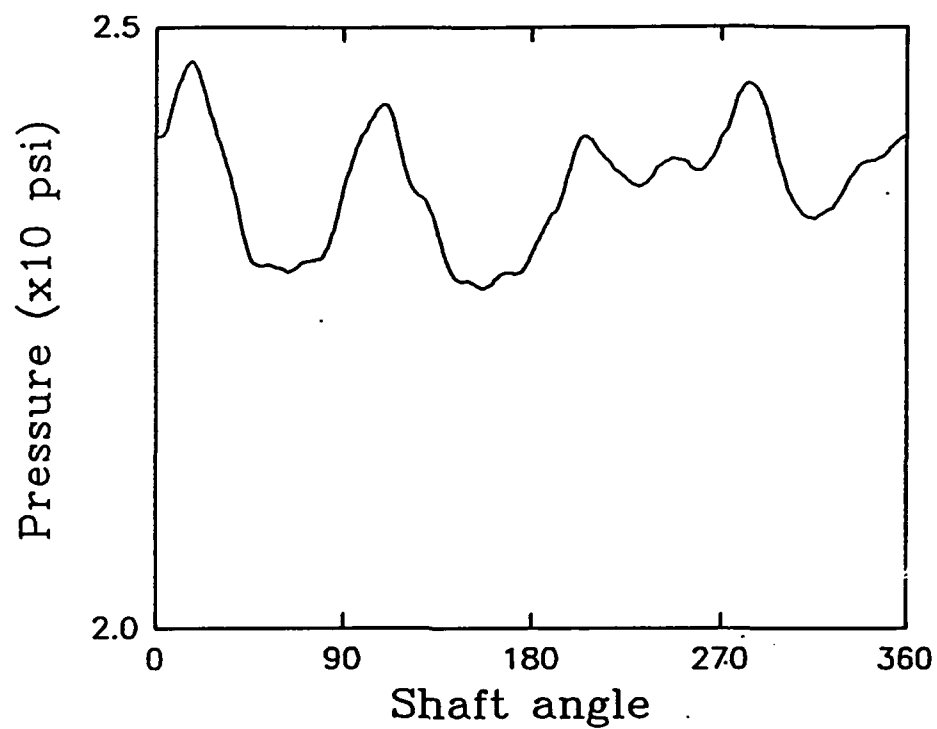
Figure 8(f)   Pressure Distribution and Frequency Spectra Obtained
at 1770 rpm at Location 6.
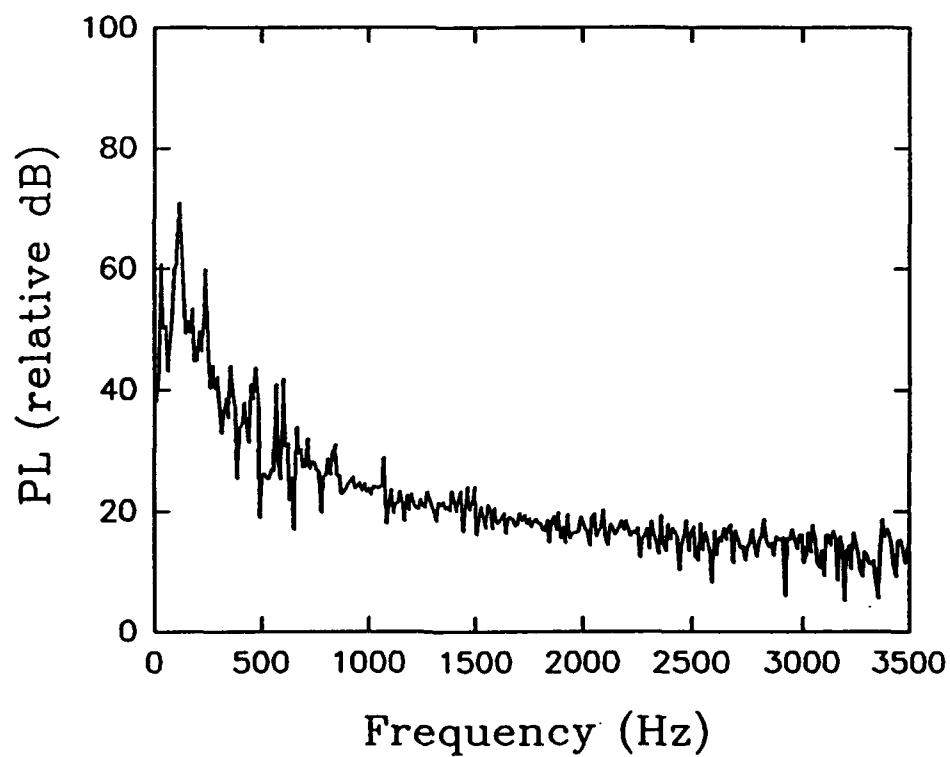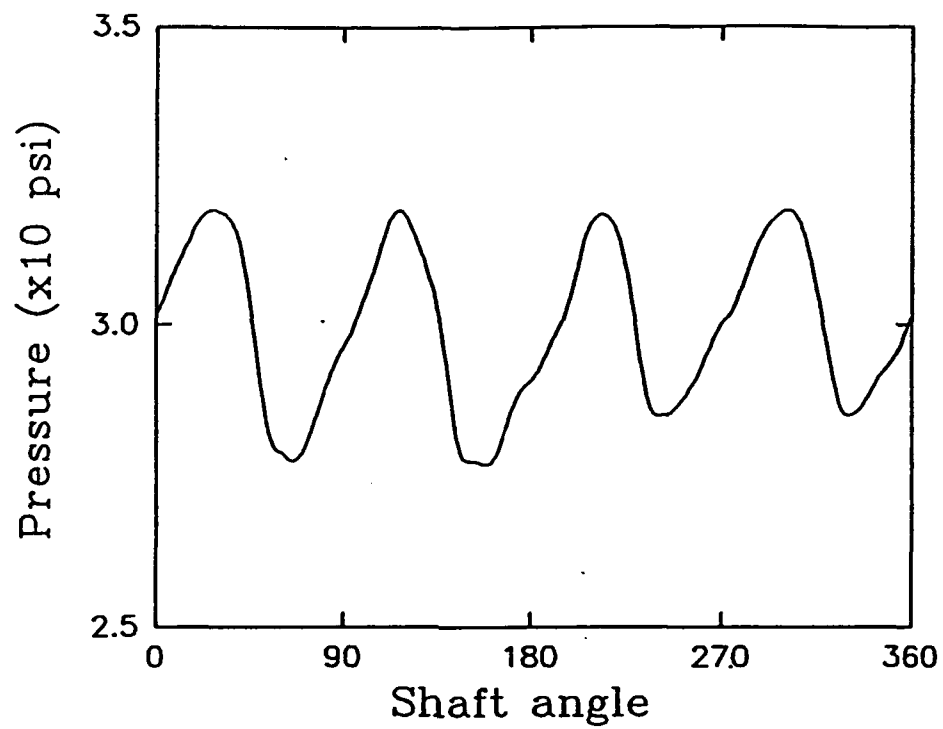
Figure 8(g)   Pressure Distribution and Frequency Spectra Obtained
                at 1770 rpm at Location 7.
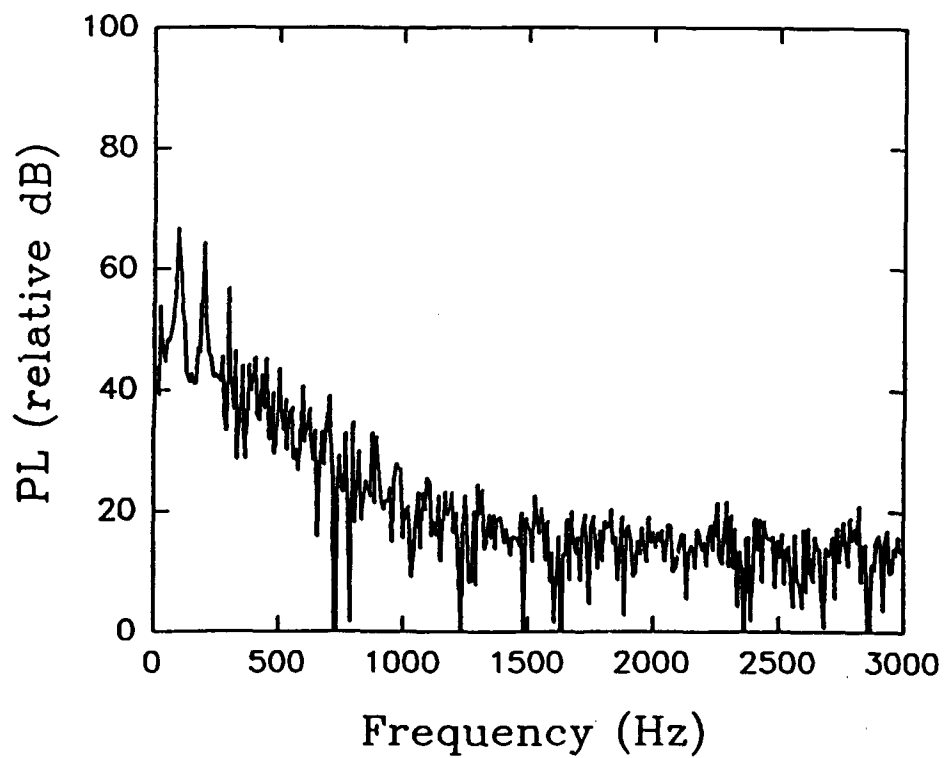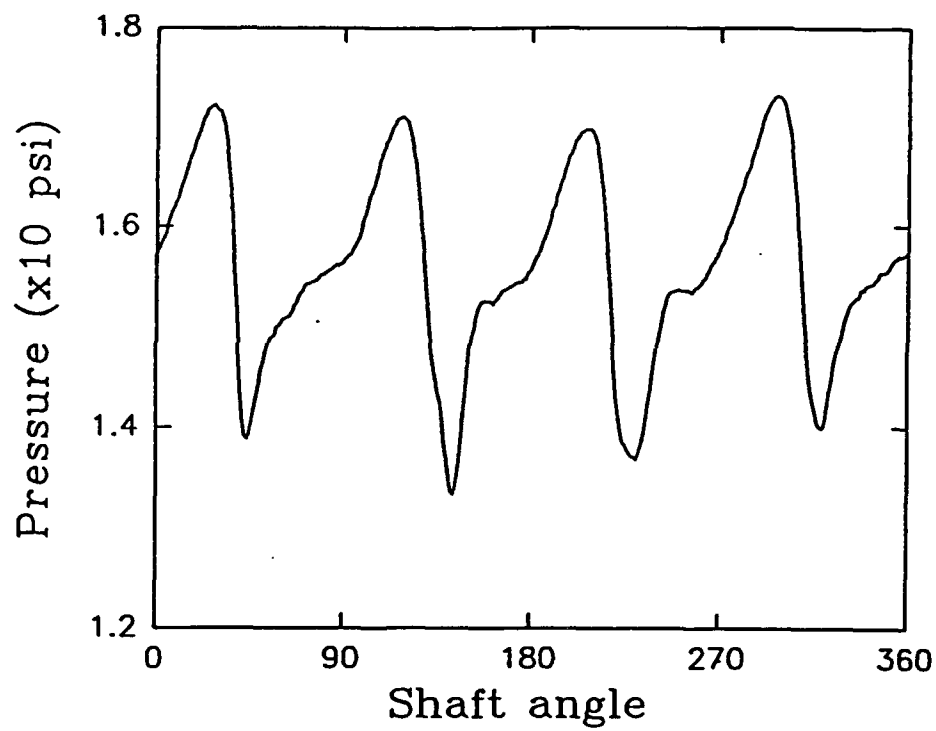
Figure 9(a)   Pressure Distribution and Frequency Spectra Obtained
at 1470 rpm at Location 1.
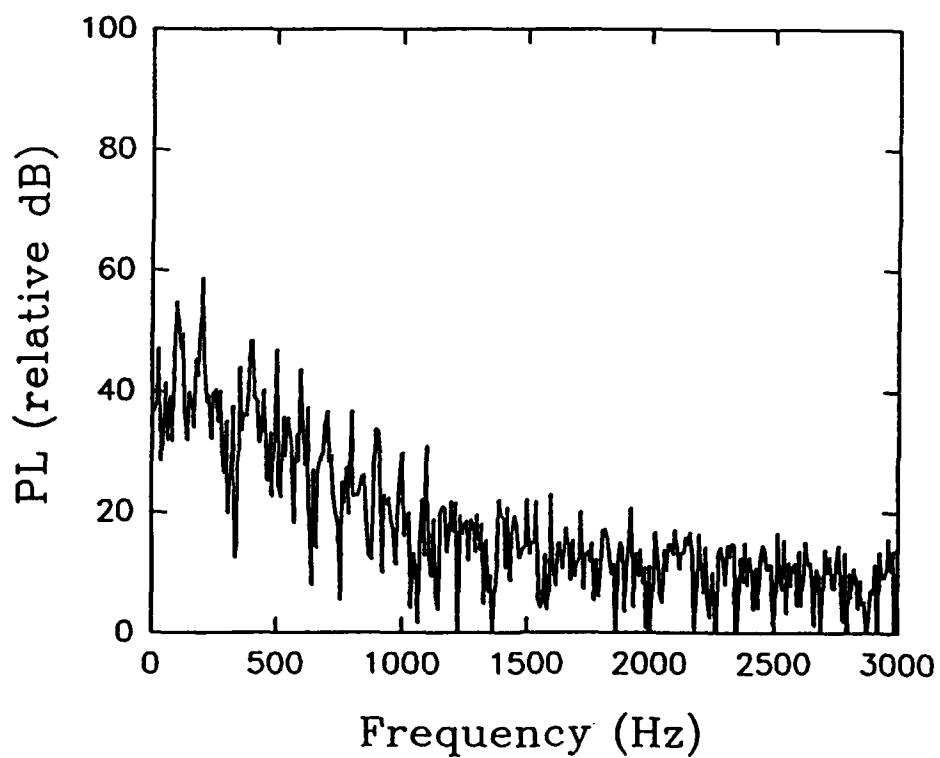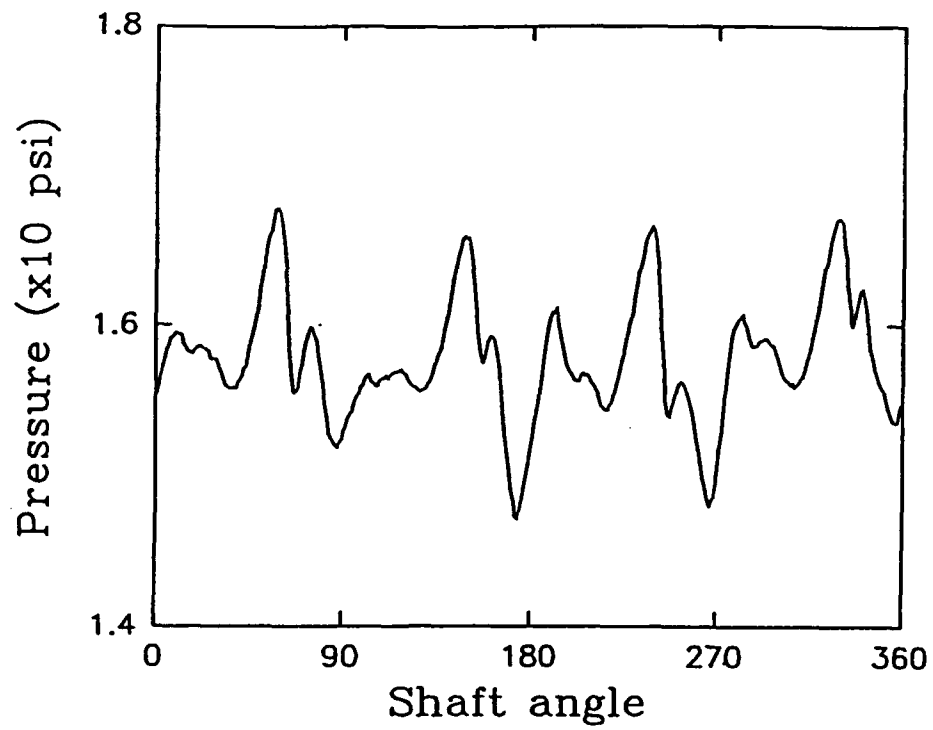
Figure 9(b)   Pressure Distribution and Frequency Spectra Obtained at 1470 rpm at Location 2.
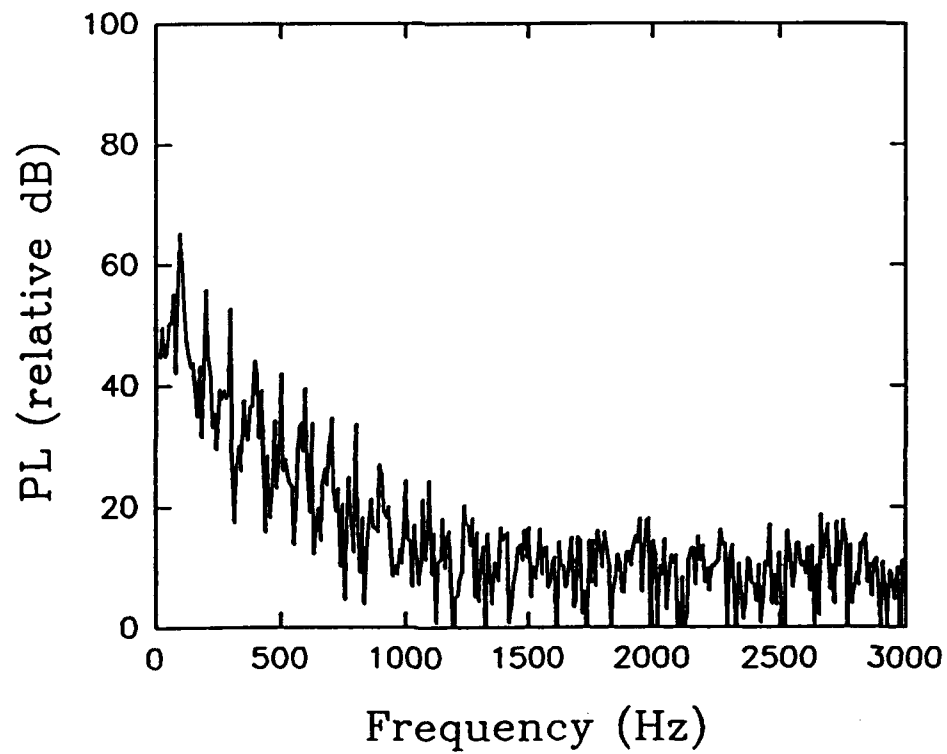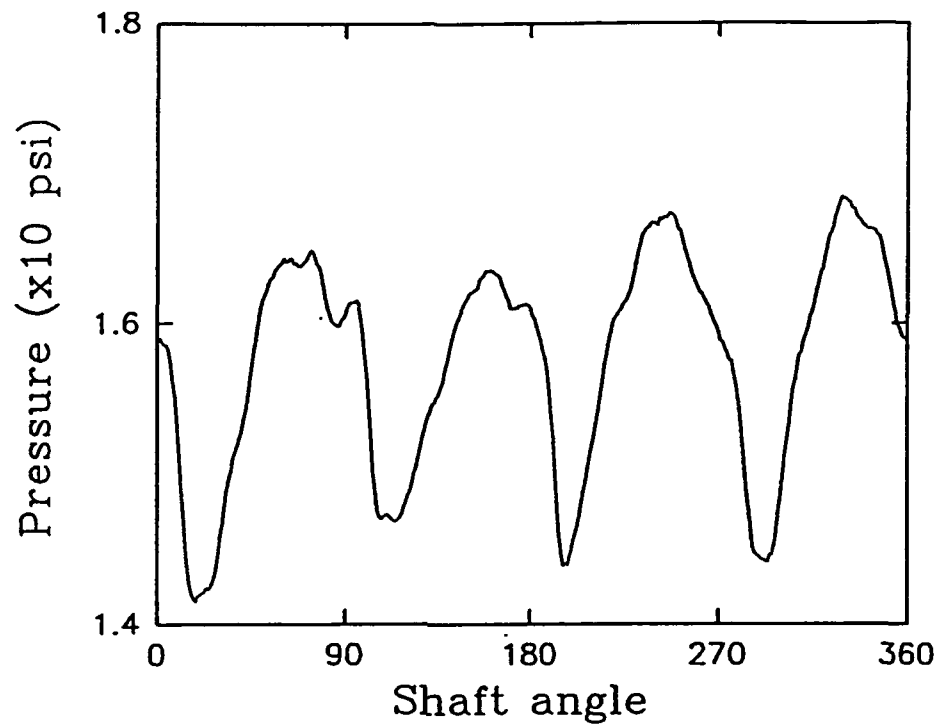
Figure 9(c)   Pressure Distribution and Frequency Spectra Obtained at 1470 rpm at Location 3.
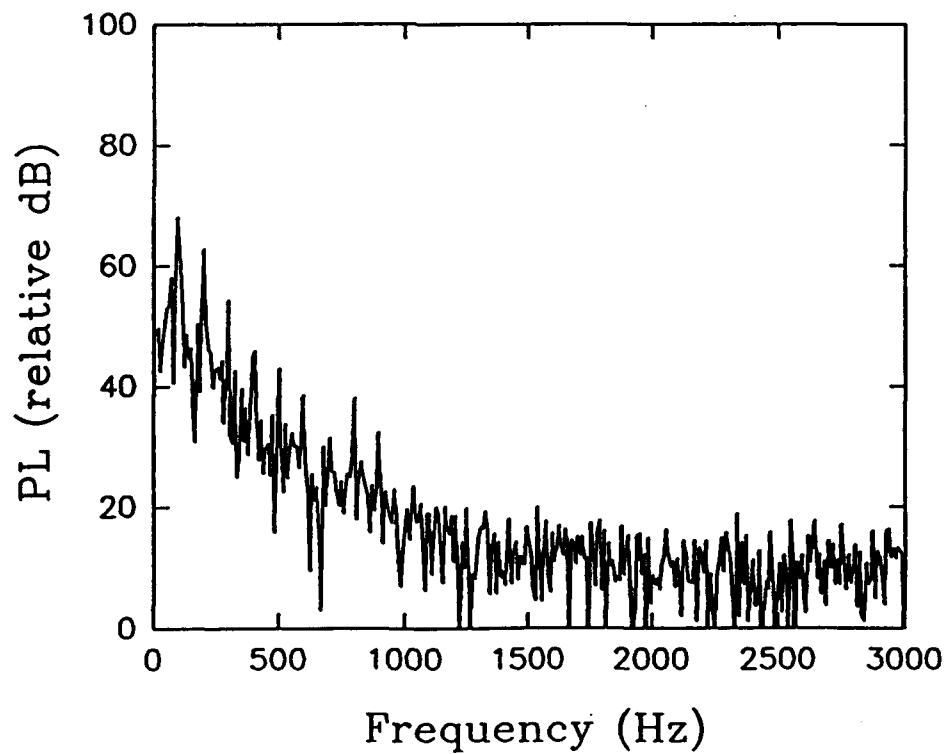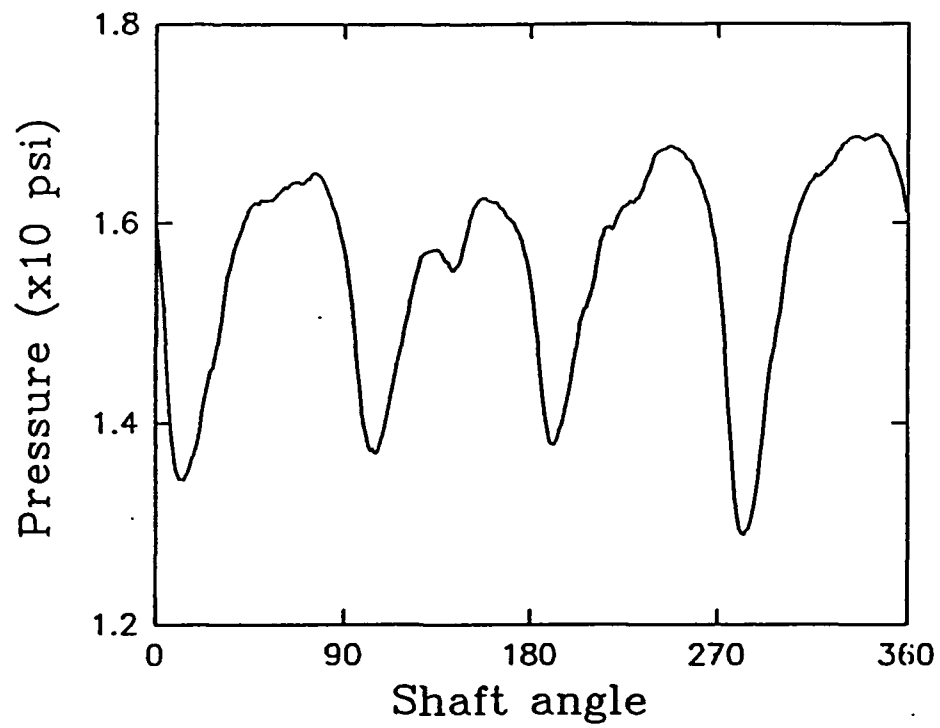
Figure 9(d)   Pressure Distribution and Frequency Spectra Obtained
                at 1470 rpm at Location 4.
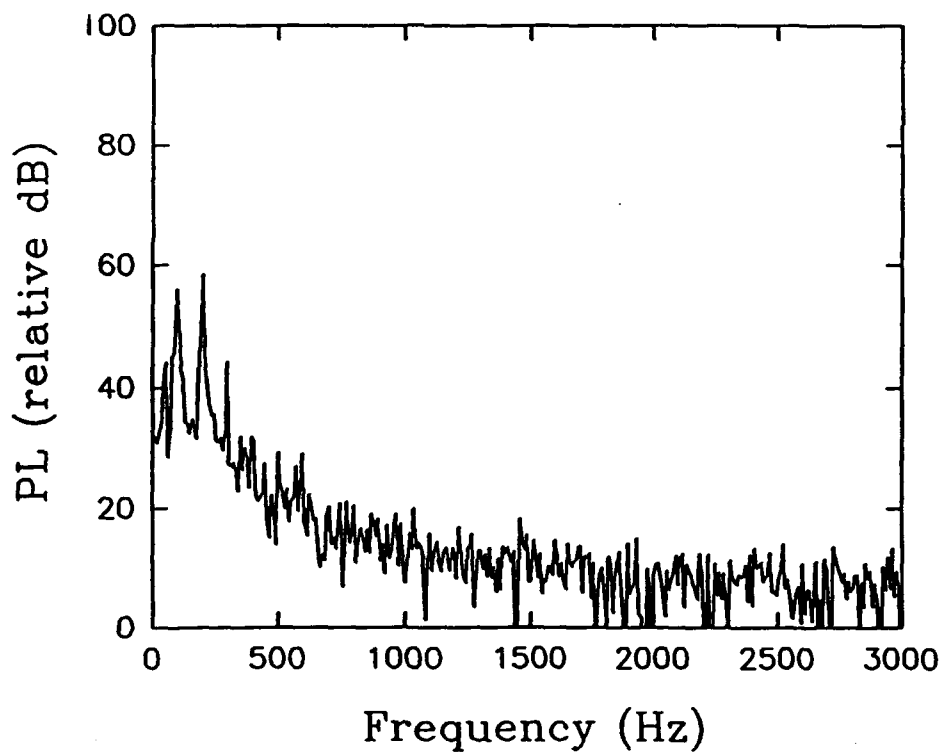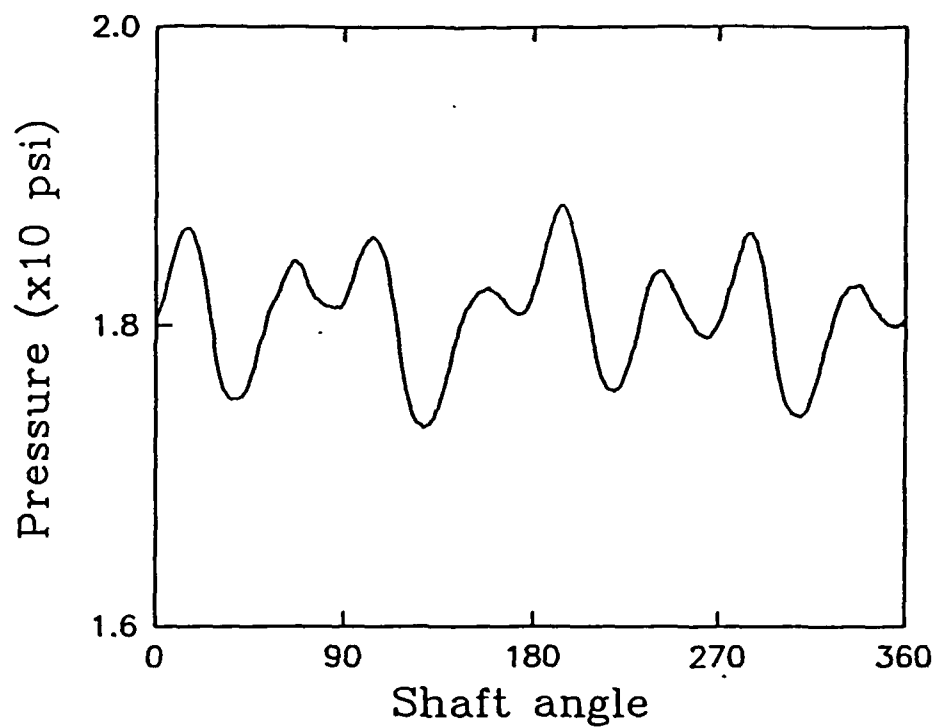
Figure 9(e)   Pressure Distribution and Frequency Spectra Obtained
at 1470 rpm at Location 5.
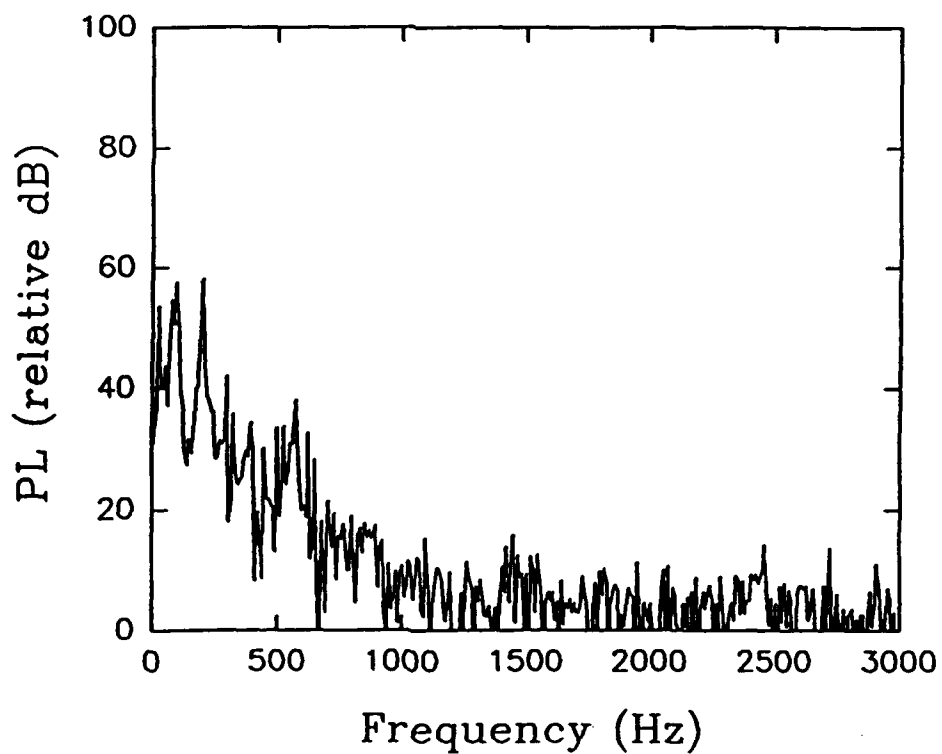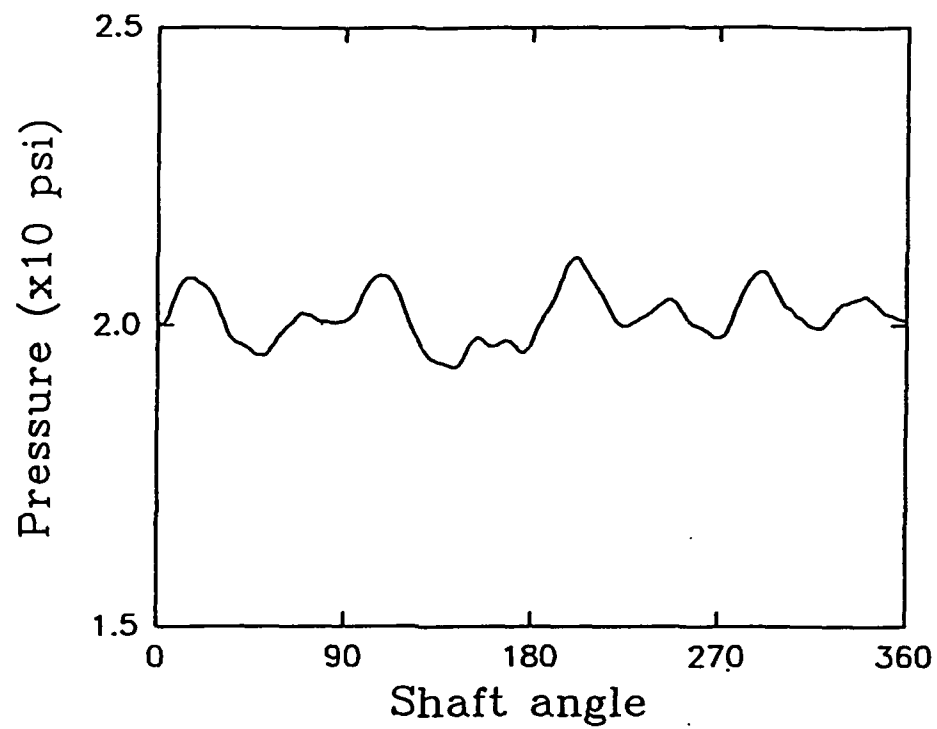
Figure 9(f) Pressure Distribution and Frequency Spectra Obtained at 1470 rpm at Location 6.
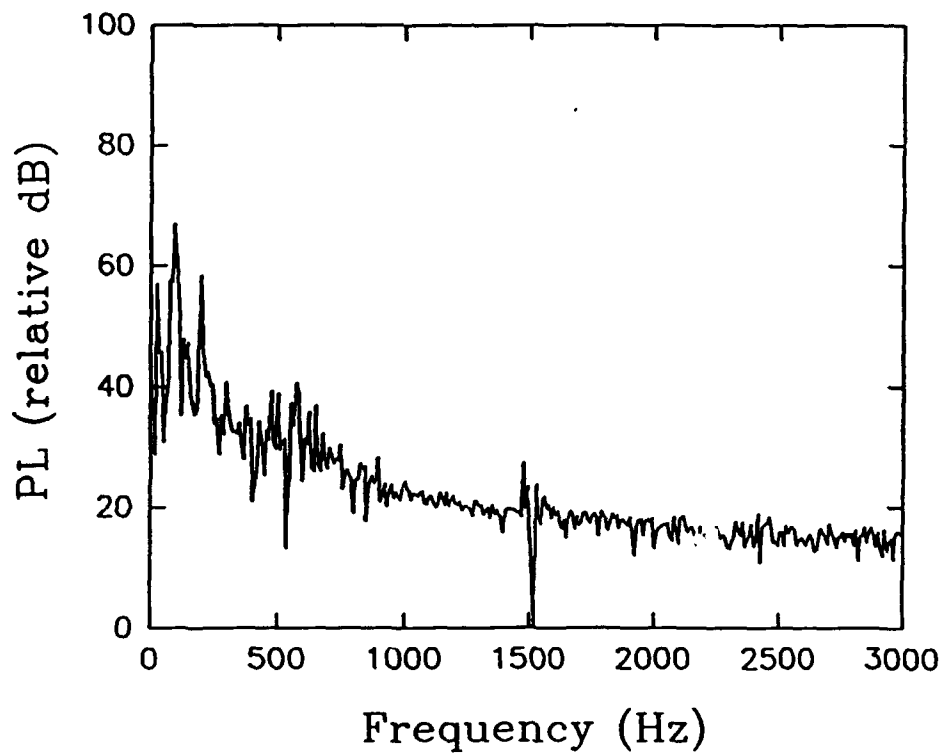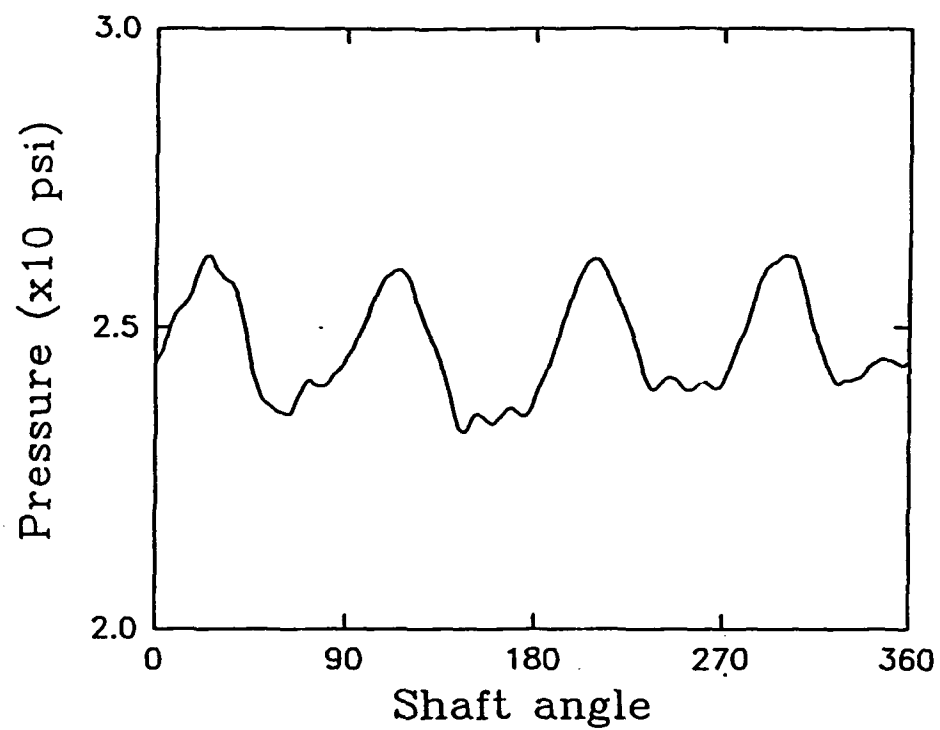
Figure 9(g)   Pressure Distribution and Frequency Spectra Obtained
at 1470 rpm at Location 7.
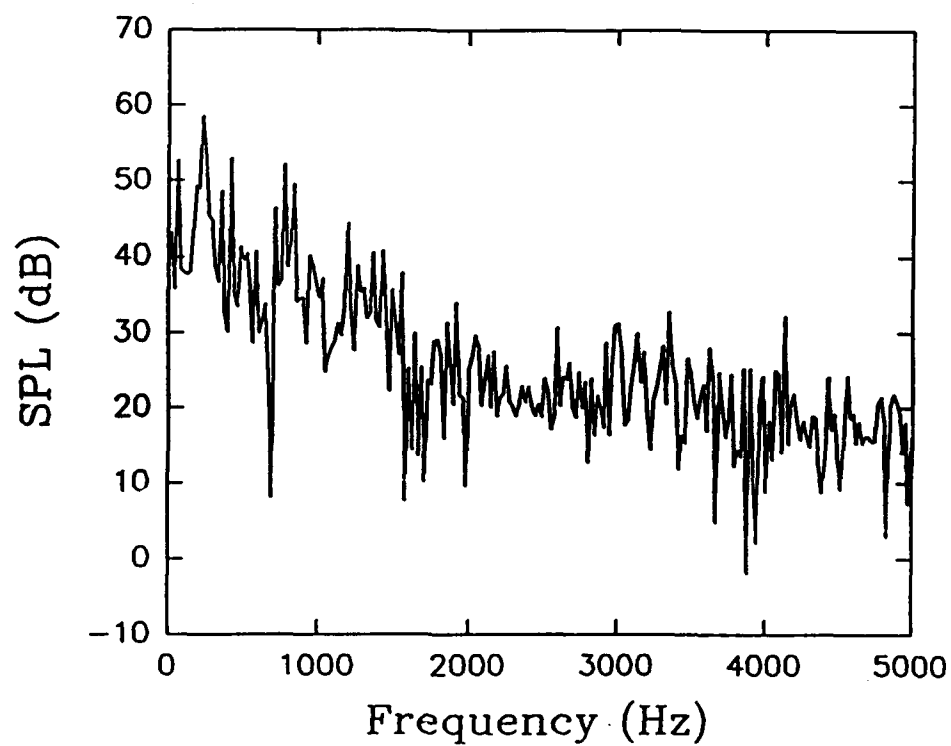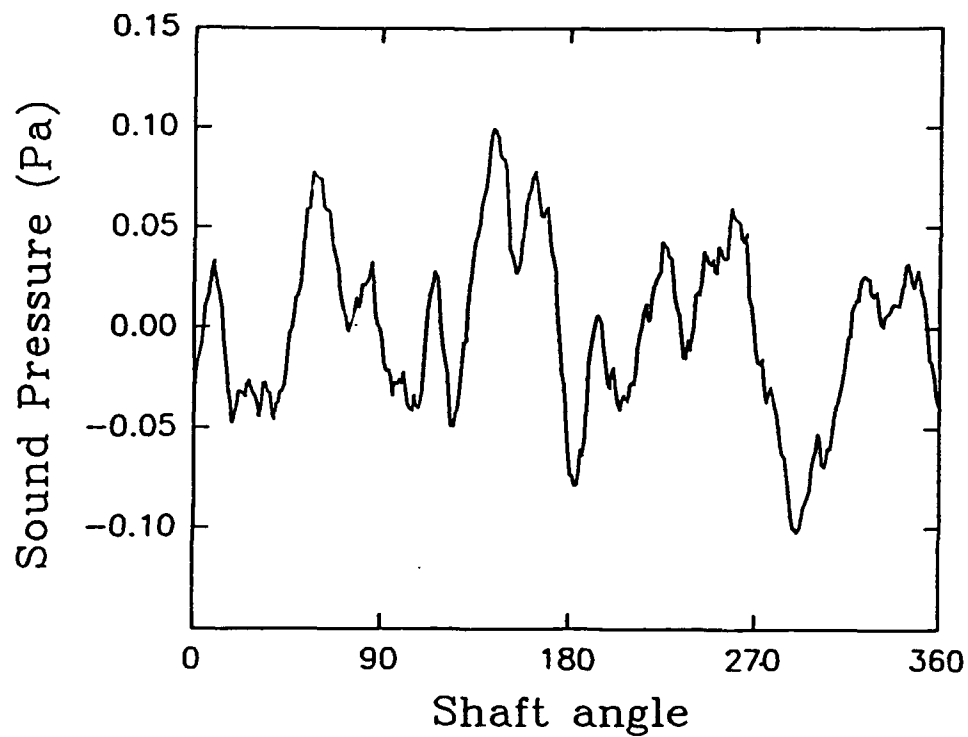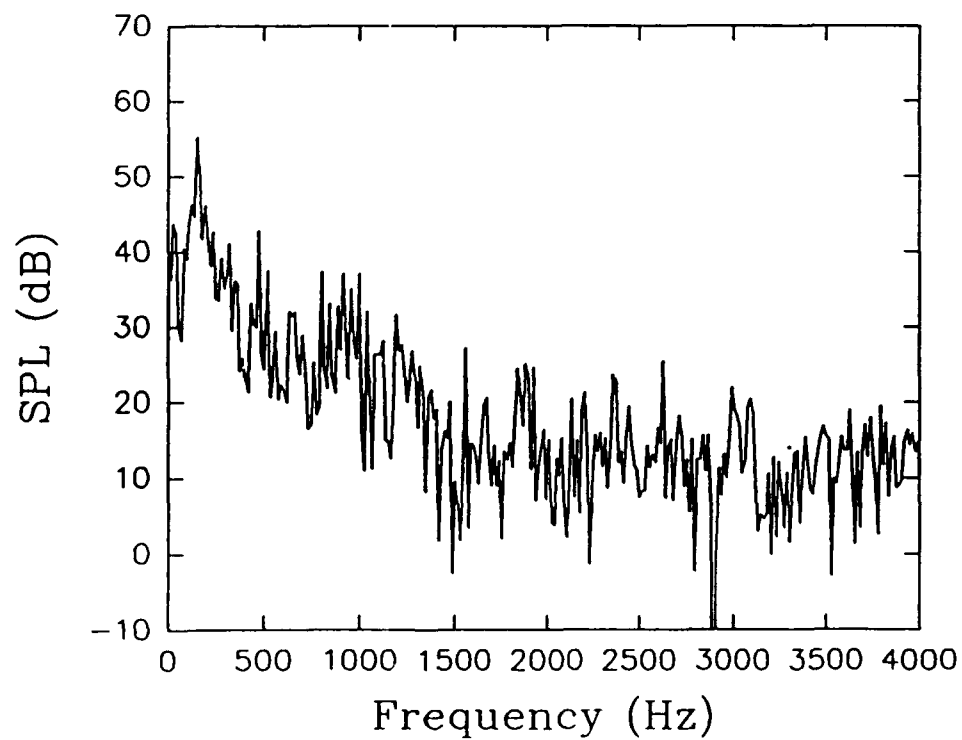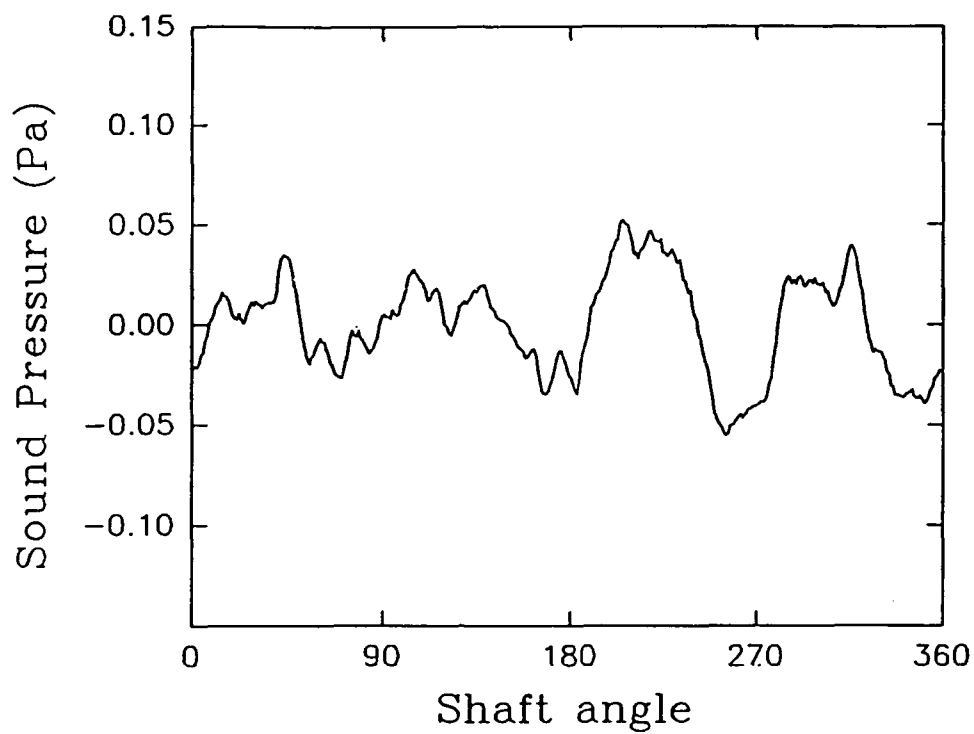
Figure 10(a)   Airborne Noise Characteristics and Frequency Spectra
Obtained with the Acrylic Casing at 3510 rpm at Location 1.
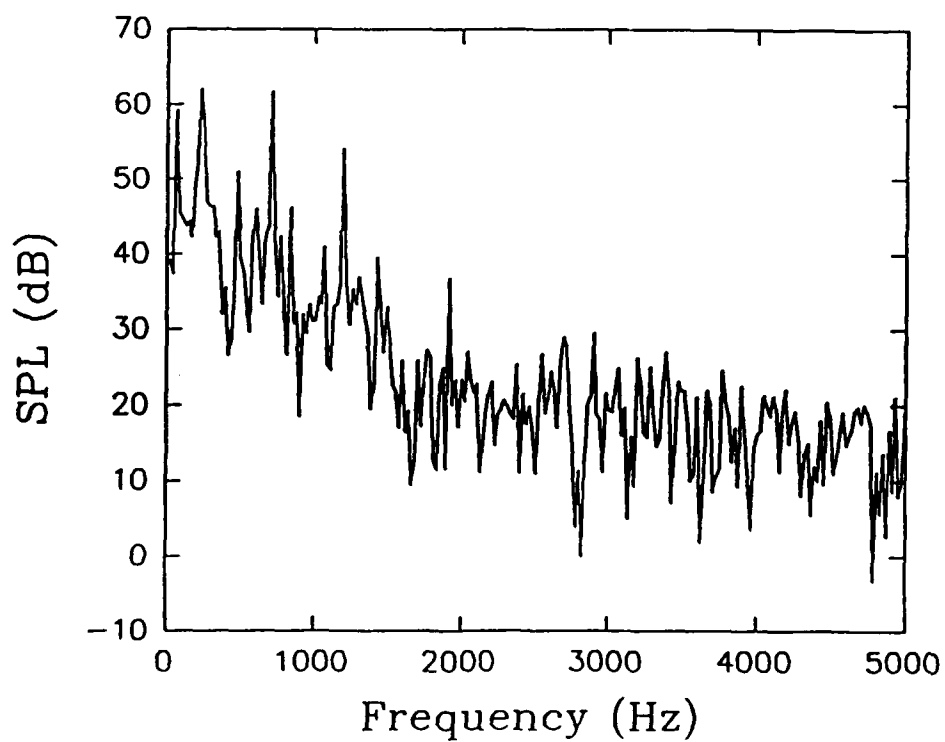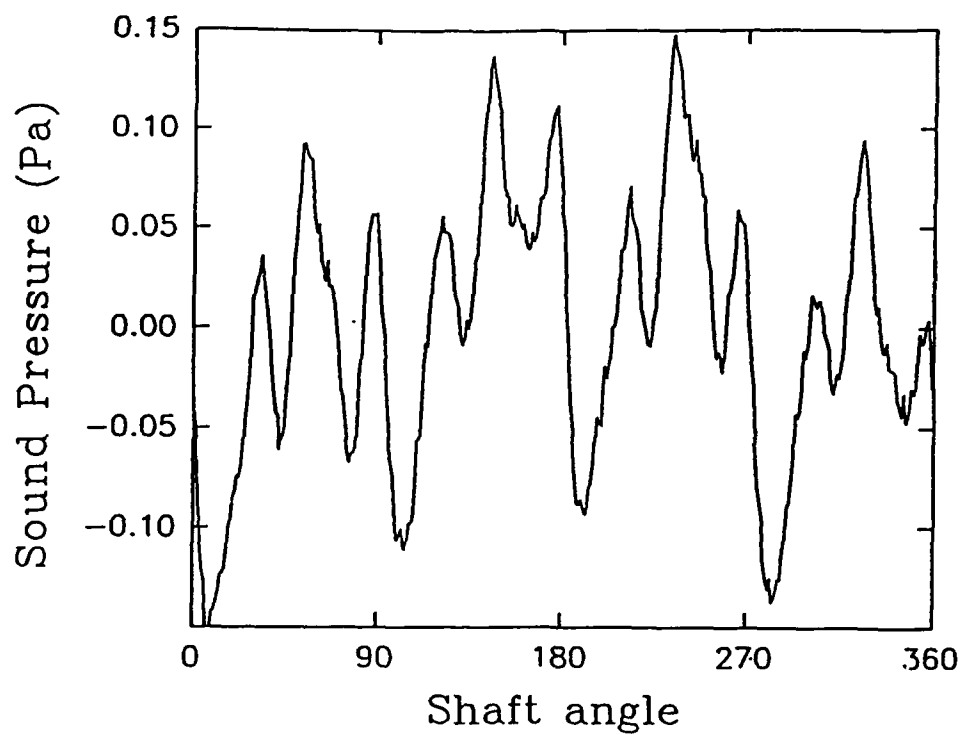
Figure 10(b) Airborne Noise Characteristics and Frequency Spectra
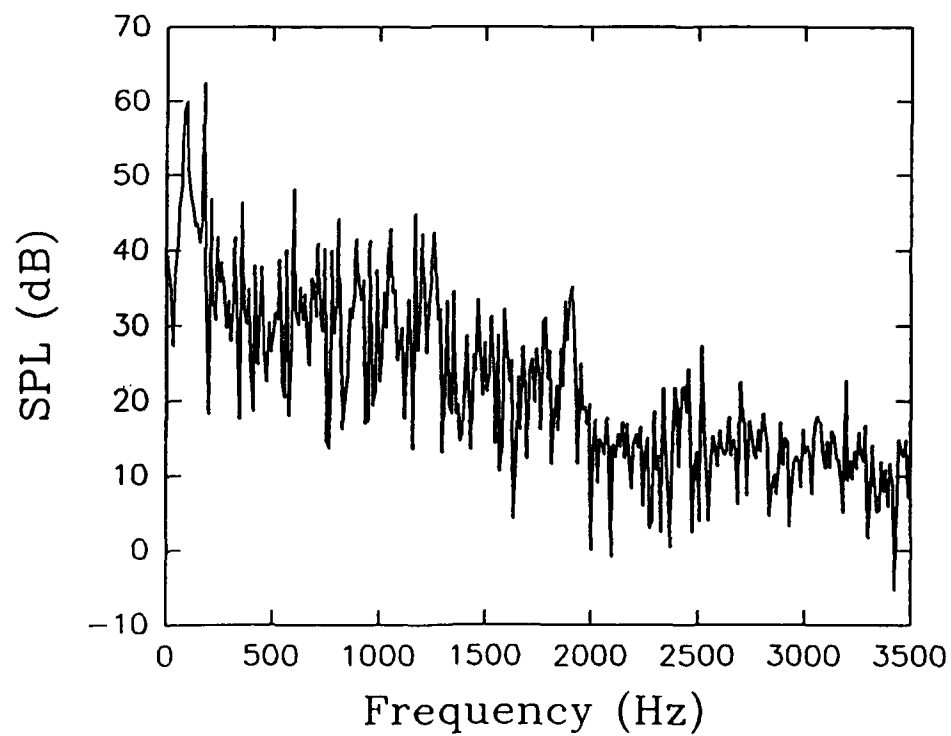Obtained with the Acrylic Casing at 3510 rpm at Location 2.
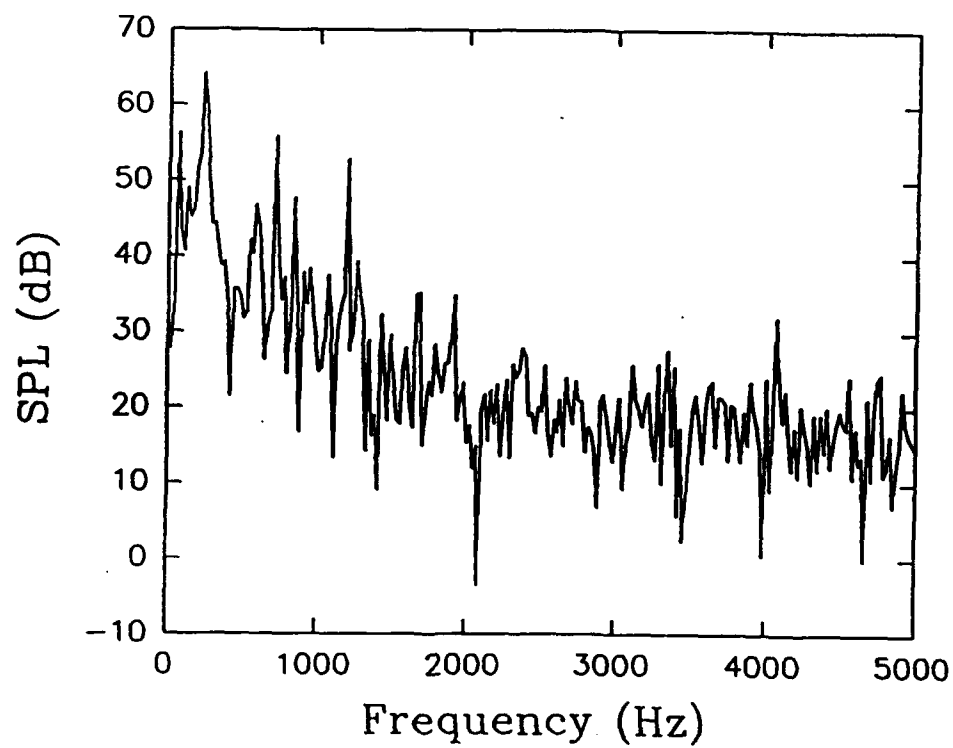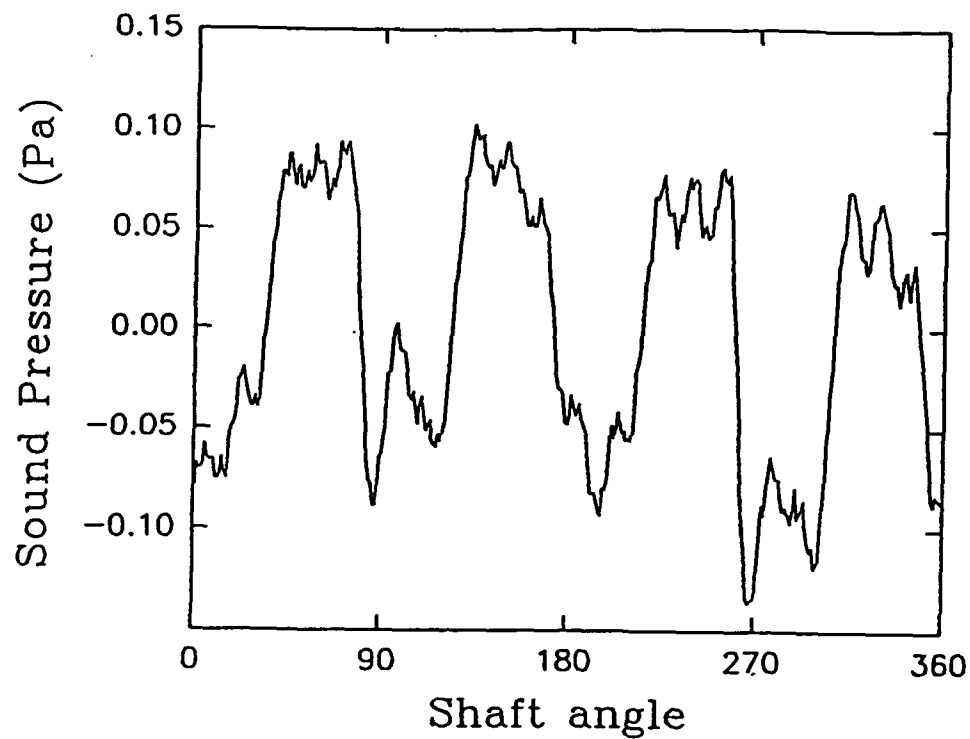
Figure 10(c)   Airborne Noise Characteristics and Frequency Spectra
Obtained with the Acrylic Casing at 3510 rpm at Location 3.
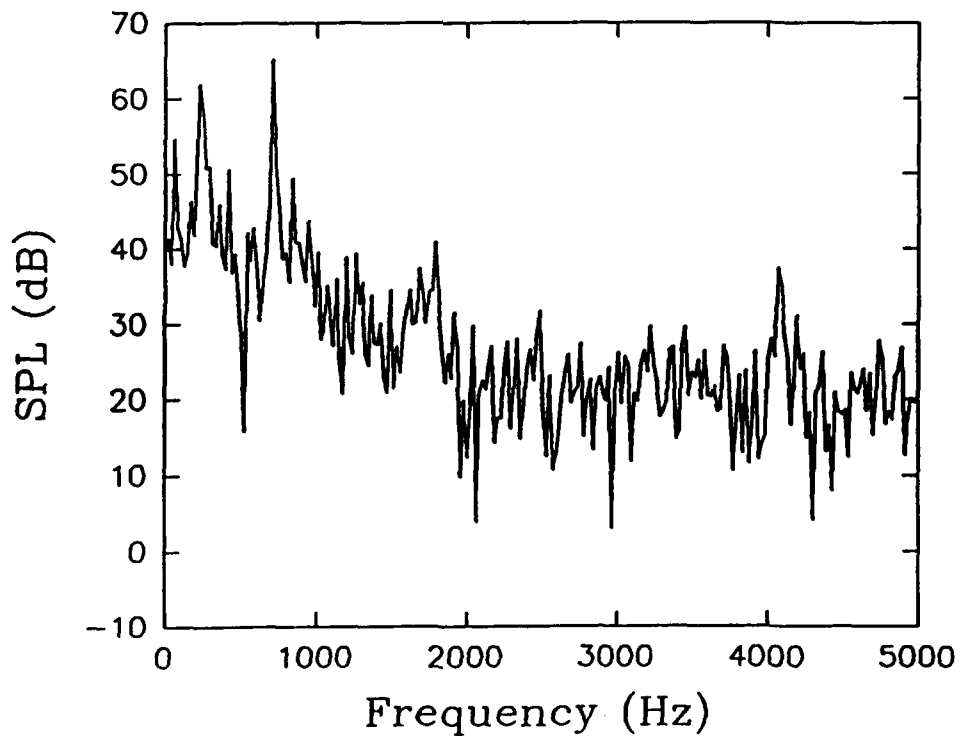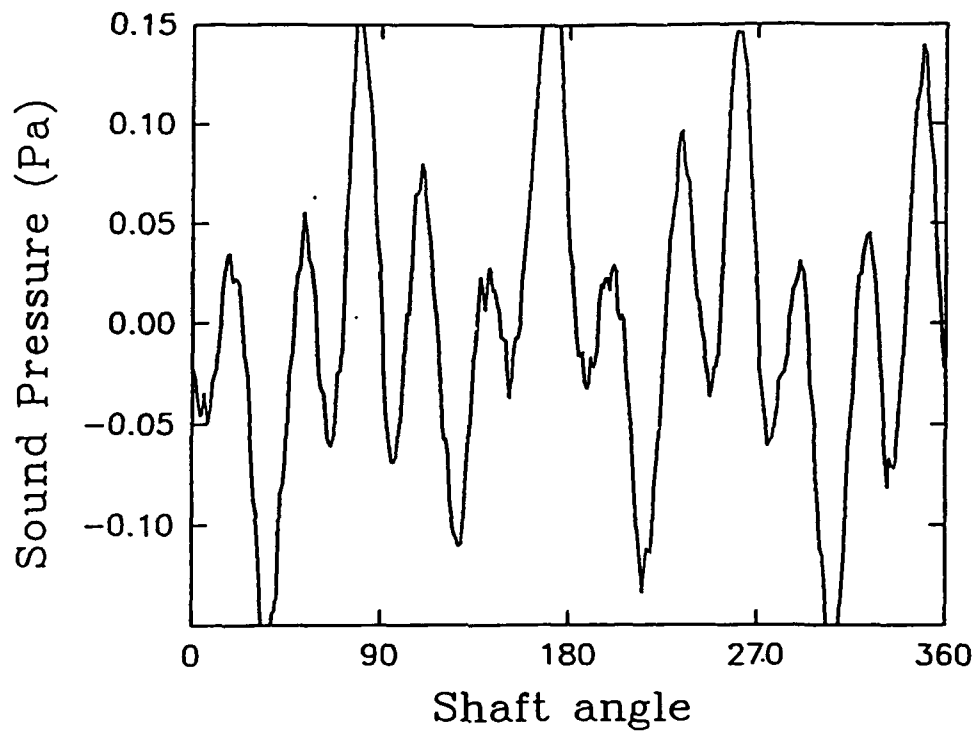
Figure 10(d)   Airborne Noise Characteristics and Frequency Spectra
Obtained with the Acrylic Casing at 3510 rpm at Location 4.
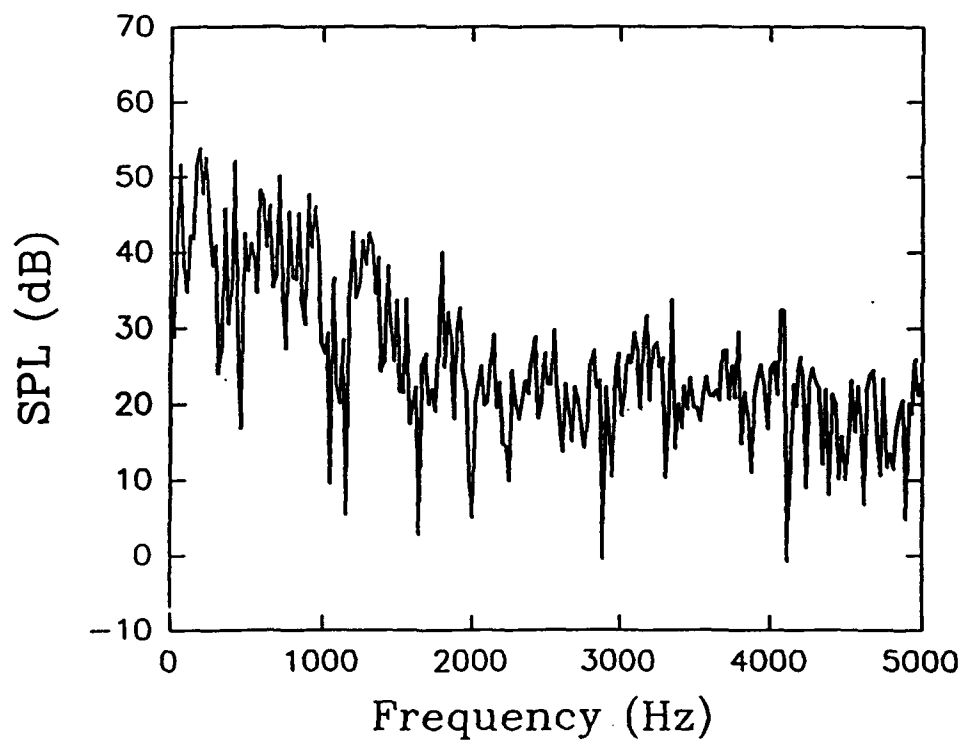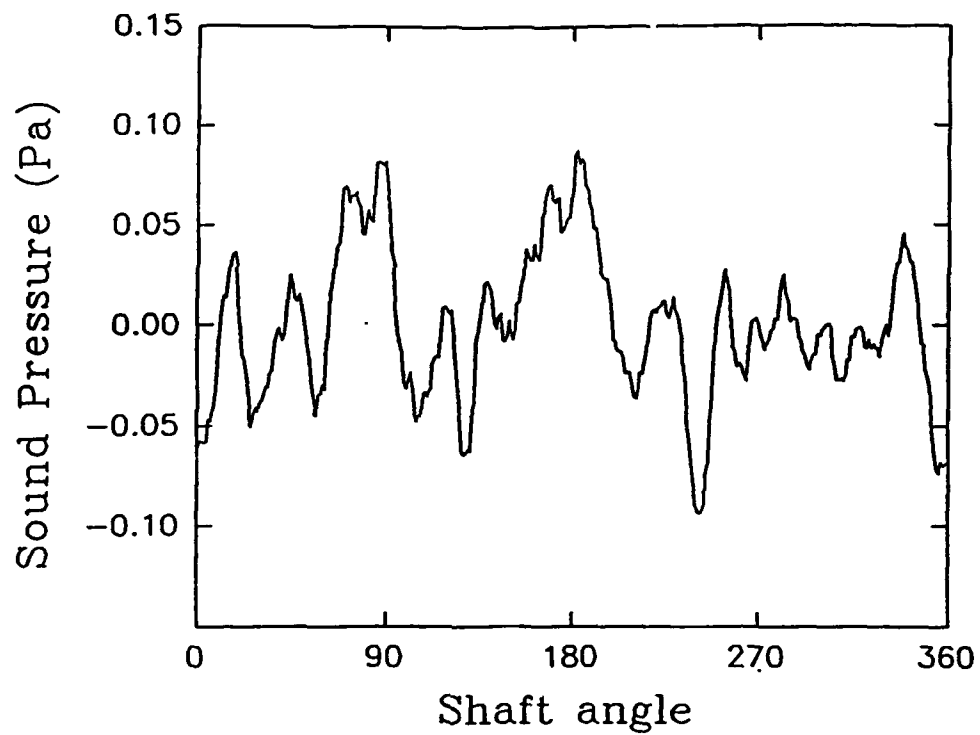
Figure 11(a)   Airborne Noise Characteristics and Frequency Spectra
                Obtained with the Acrylic Casing and the aid of a
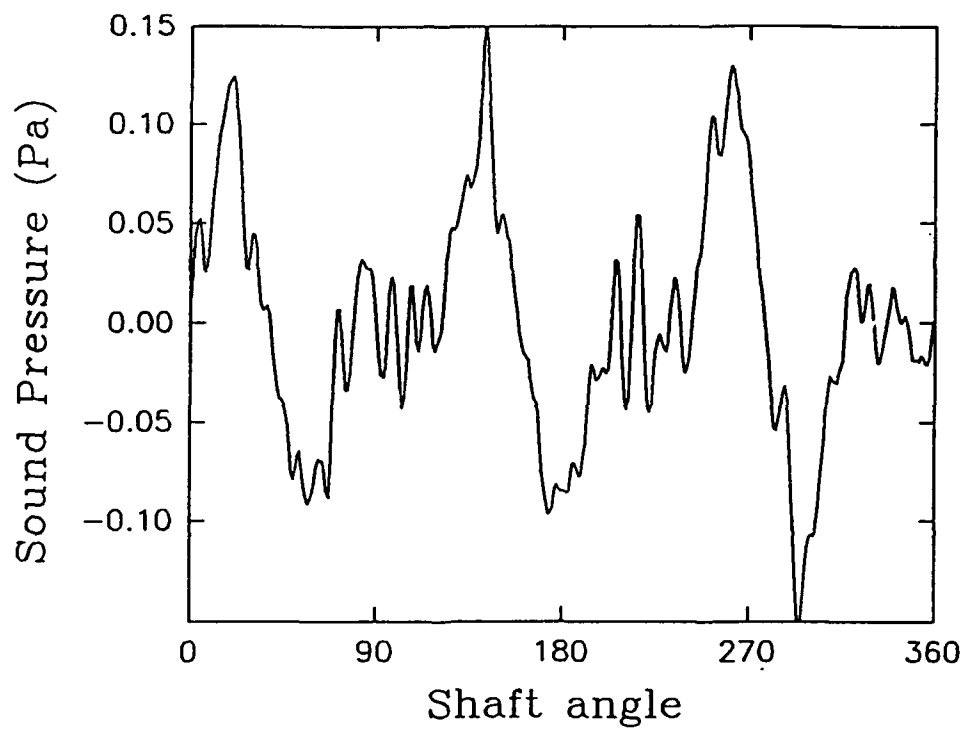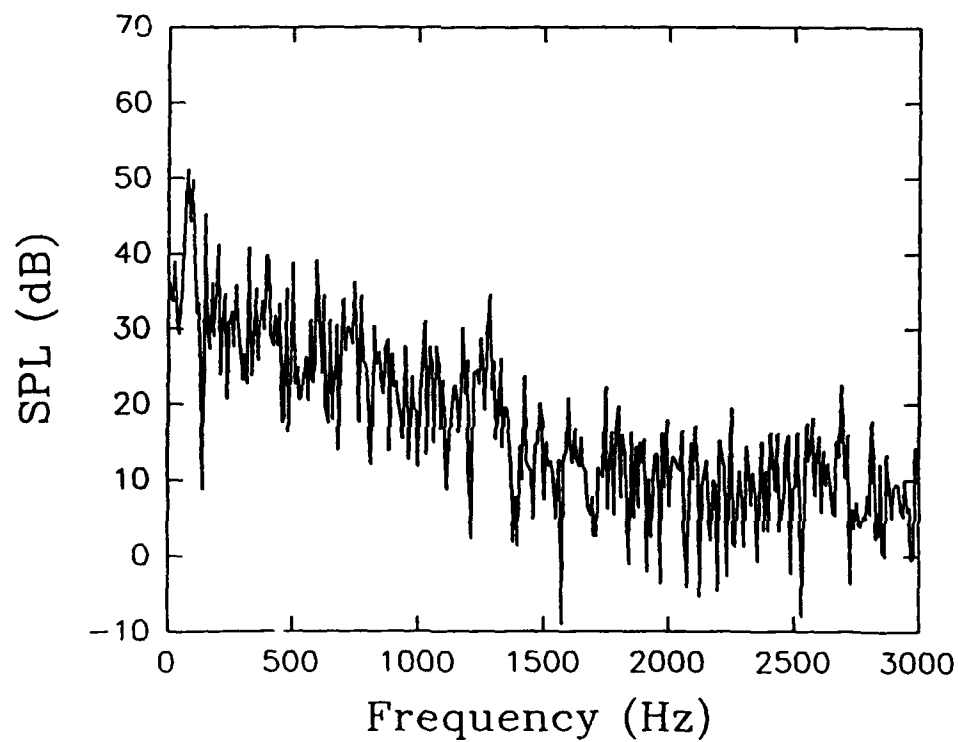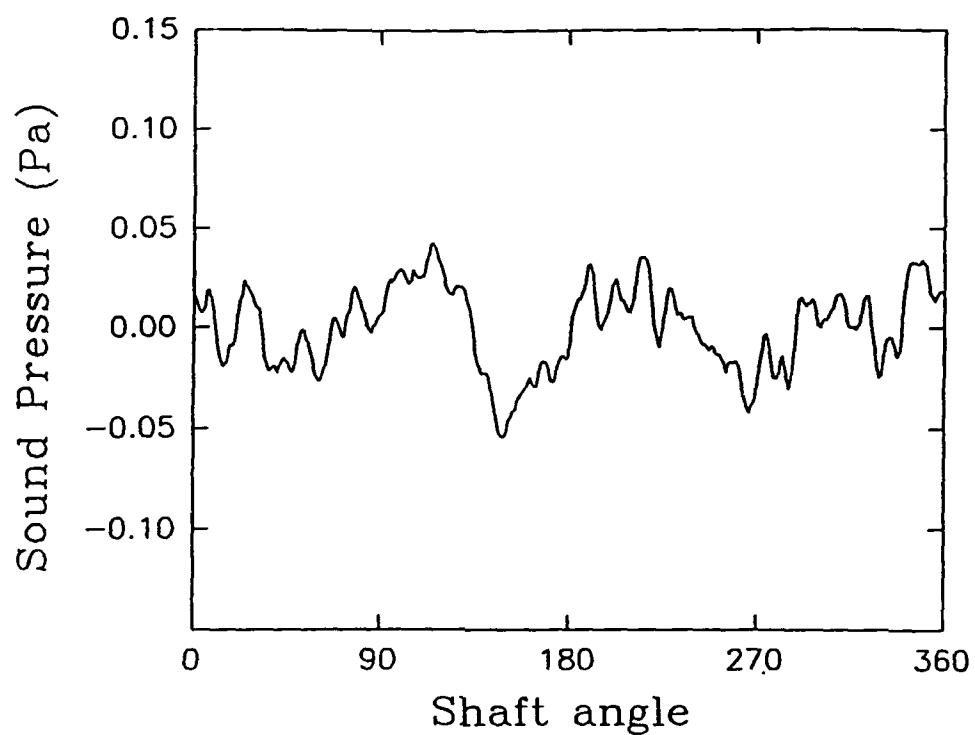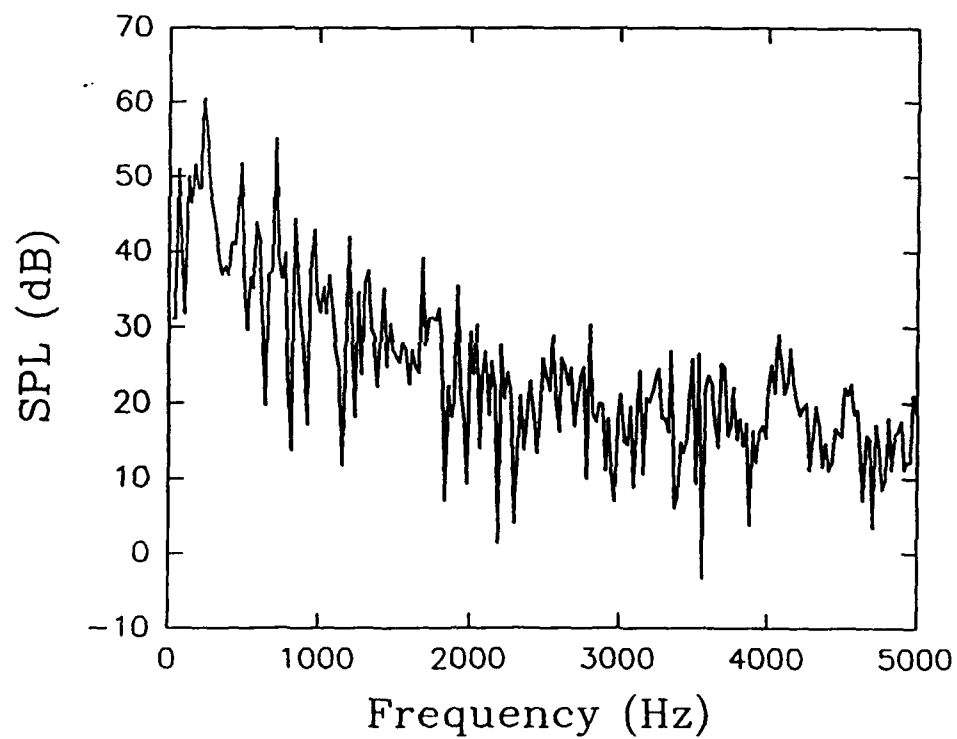   Controller at 3510 rpm at Location 1.
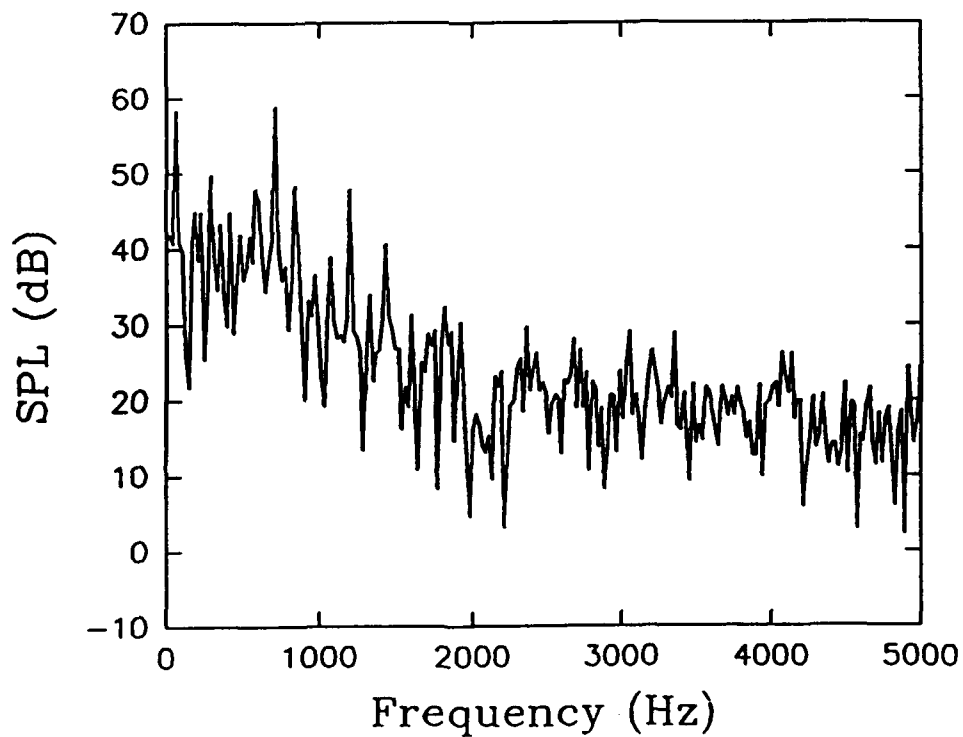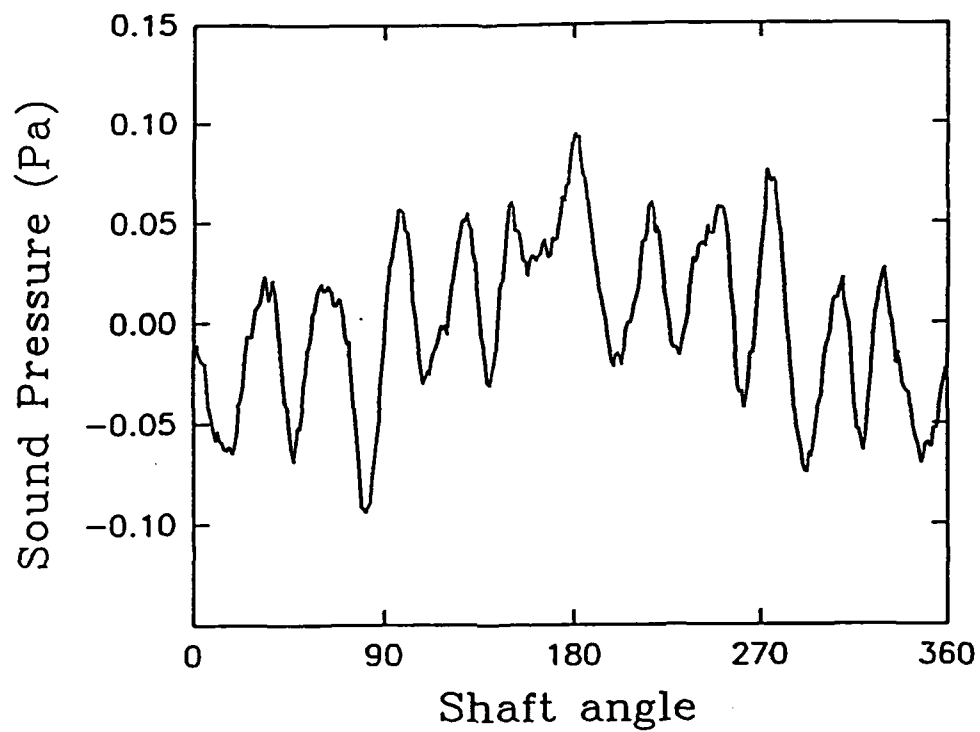
Figure 11(b)   Airborne Noise Characteristics and Frequency Spectra
Obtained with the Acrylic Casing and the aid of a
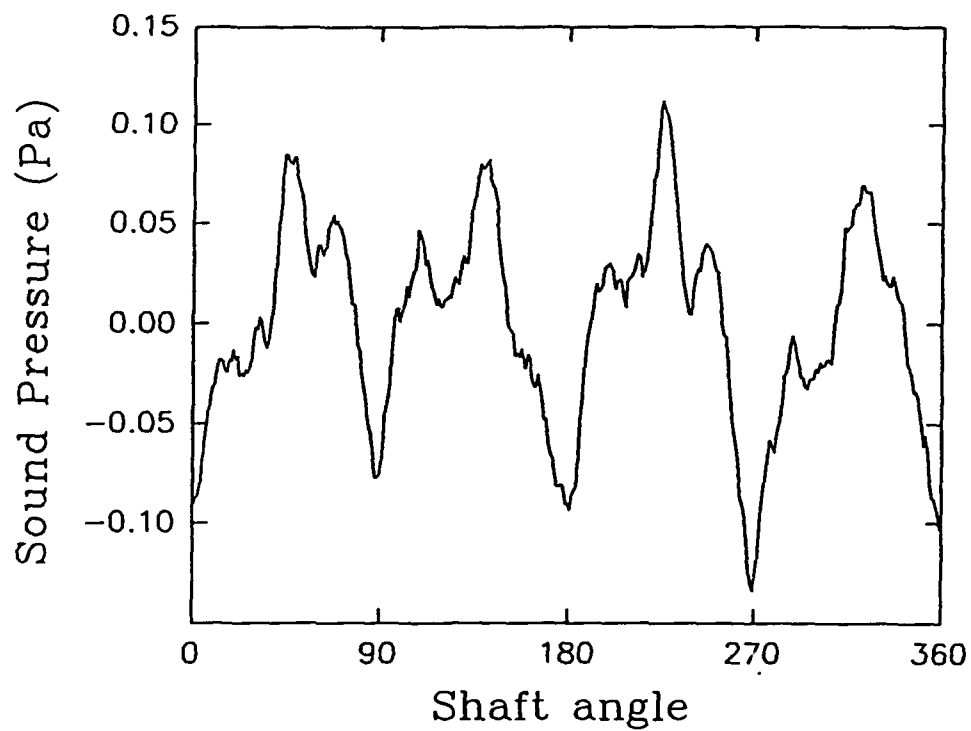Controller at 3510 rpm at Location 2.
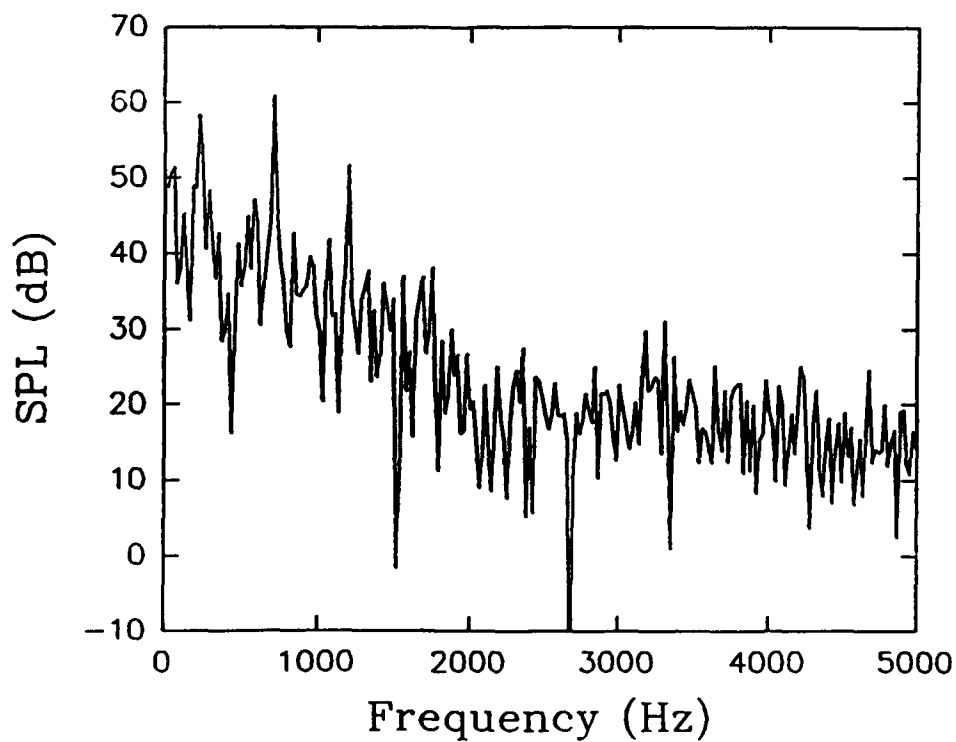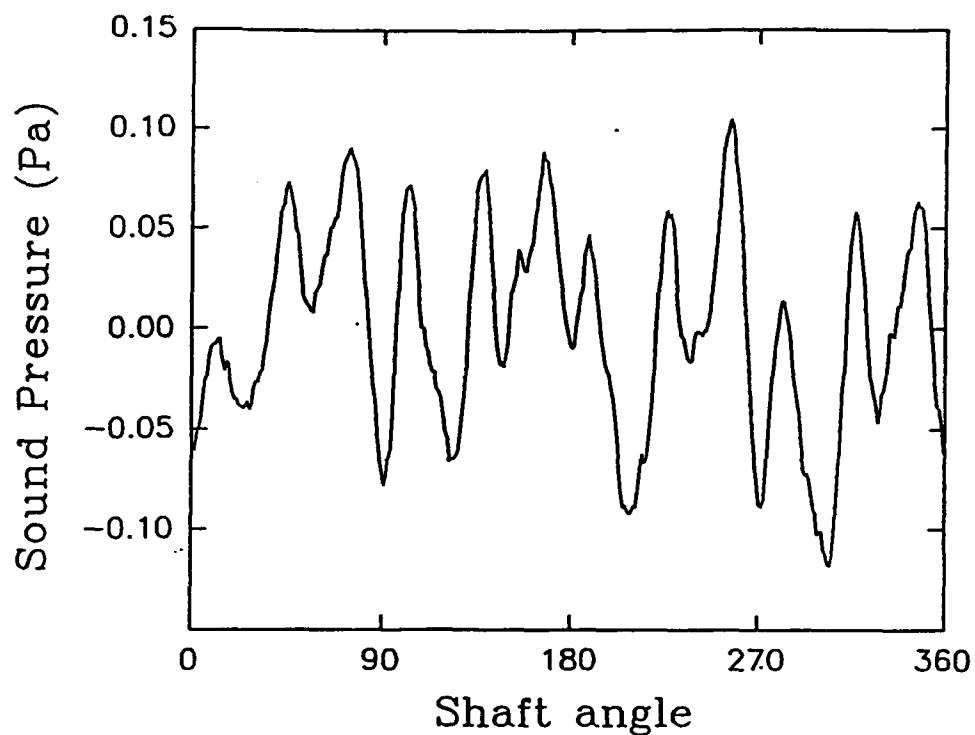
Figure 11(c)   Airborne Noise Characteristics and Frequency Spectra
Obtained with the Acrylic Casing and the aid of a
Controller at 3510 rpm at Location 3.
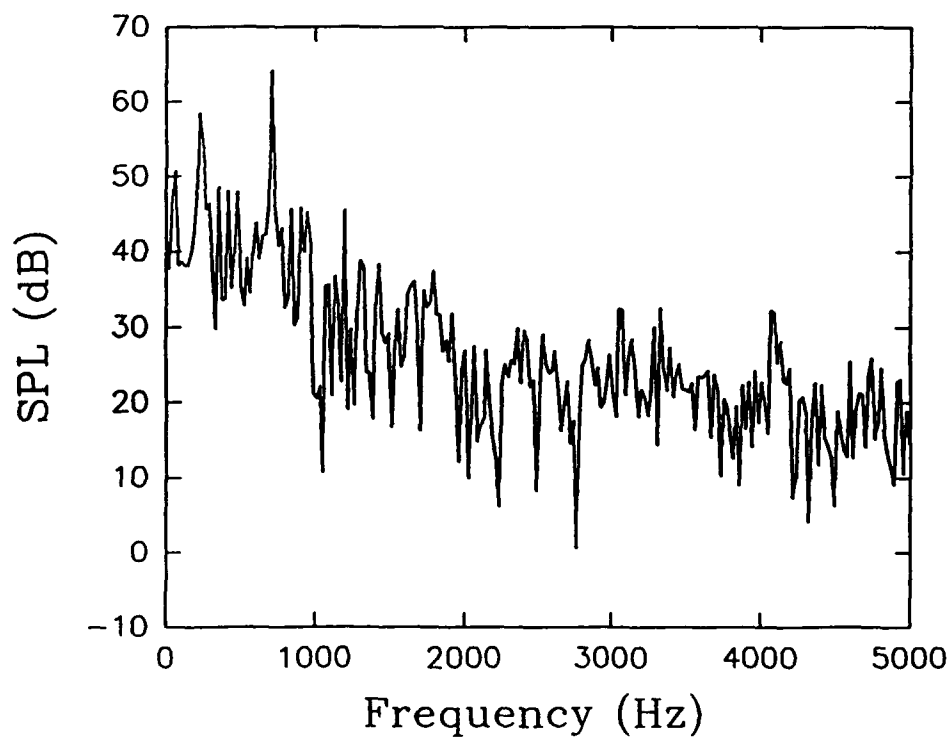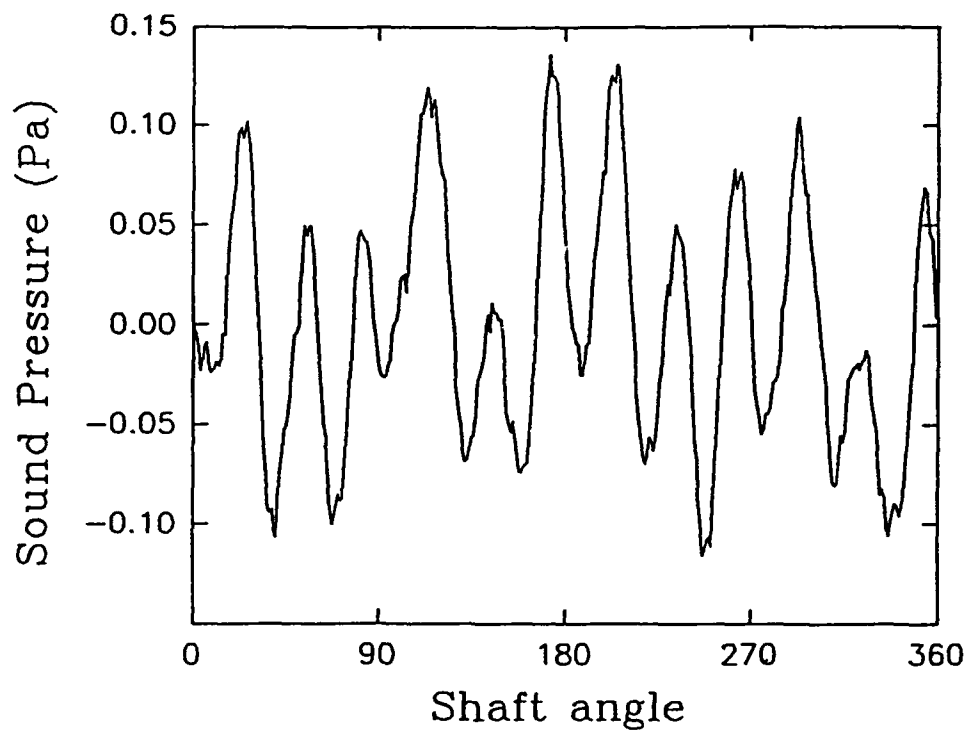
Figure 11(d)   Airborne Noise Characteristics and Frequency Spectra
Obtained with the Acrylic Casing and the aid of a
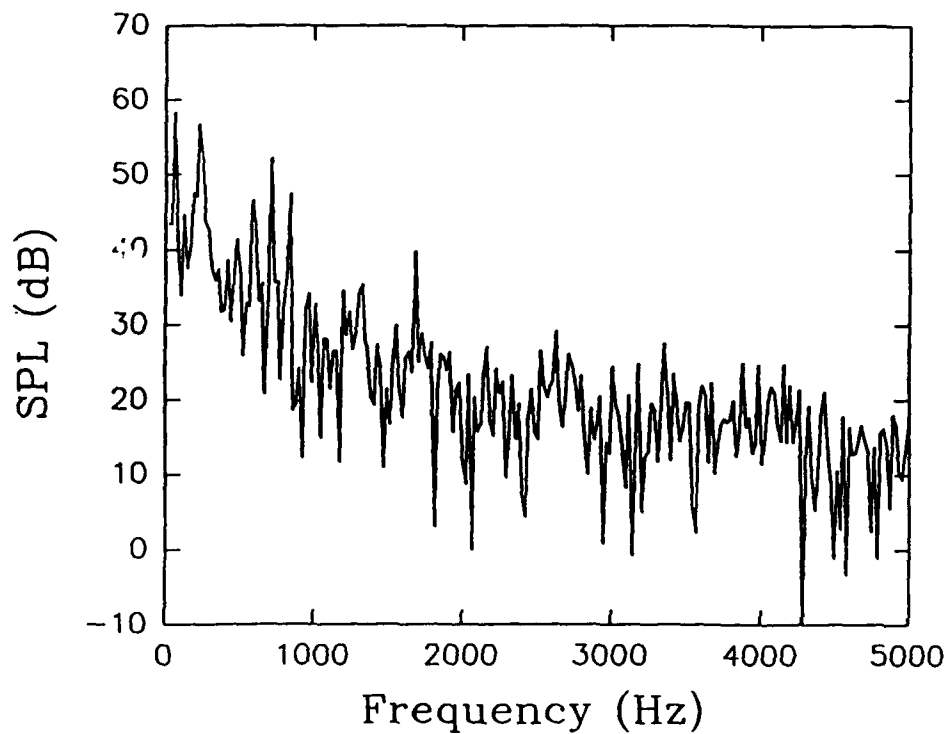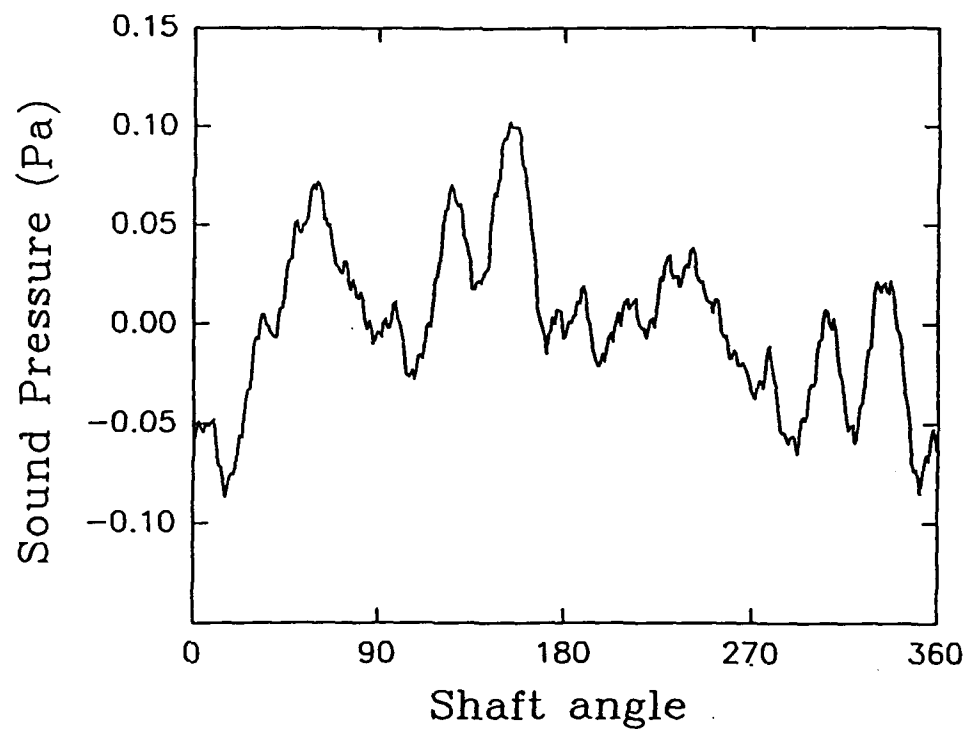Controller at 3510 rpm at Location 4.
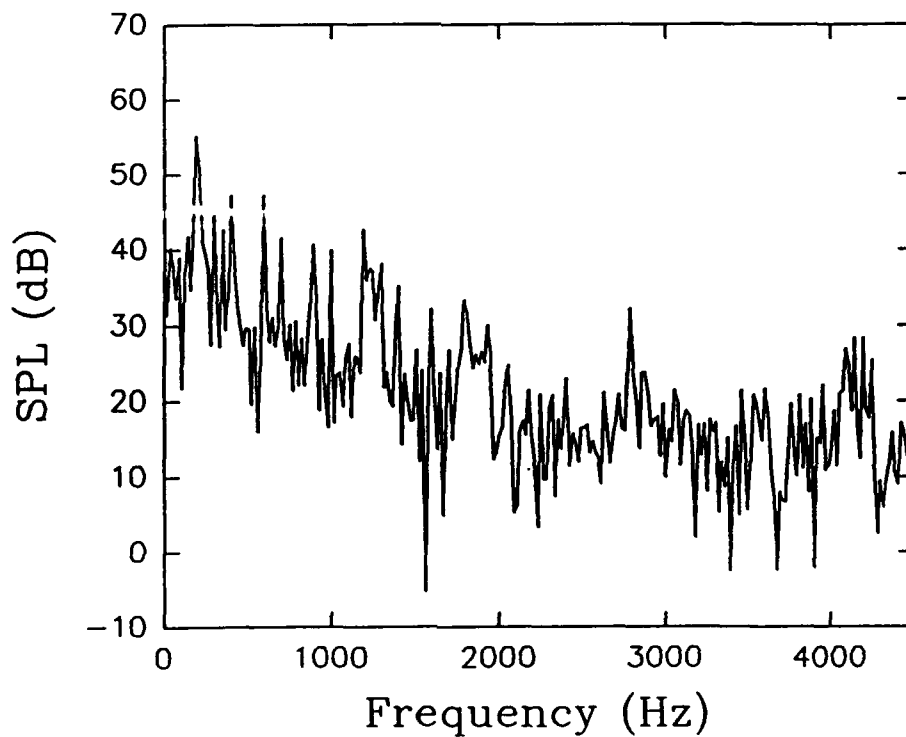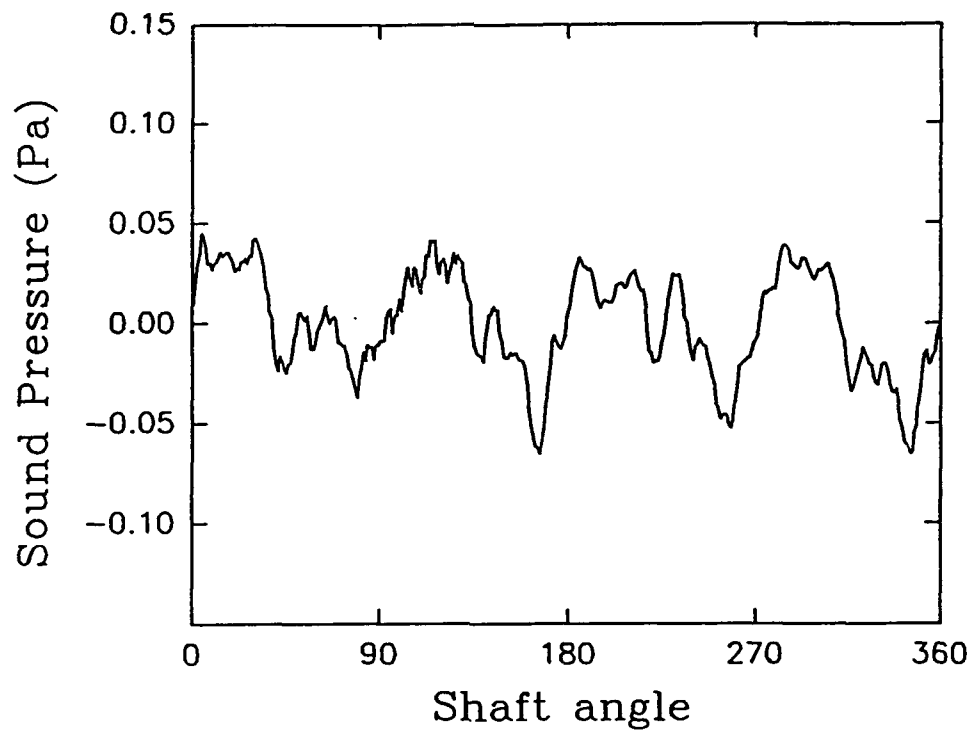
Figure 12(a)   Airborne Noise Characteristics and Frequency Spectra
                Obtained with the Acrylic Casing and the aid of a
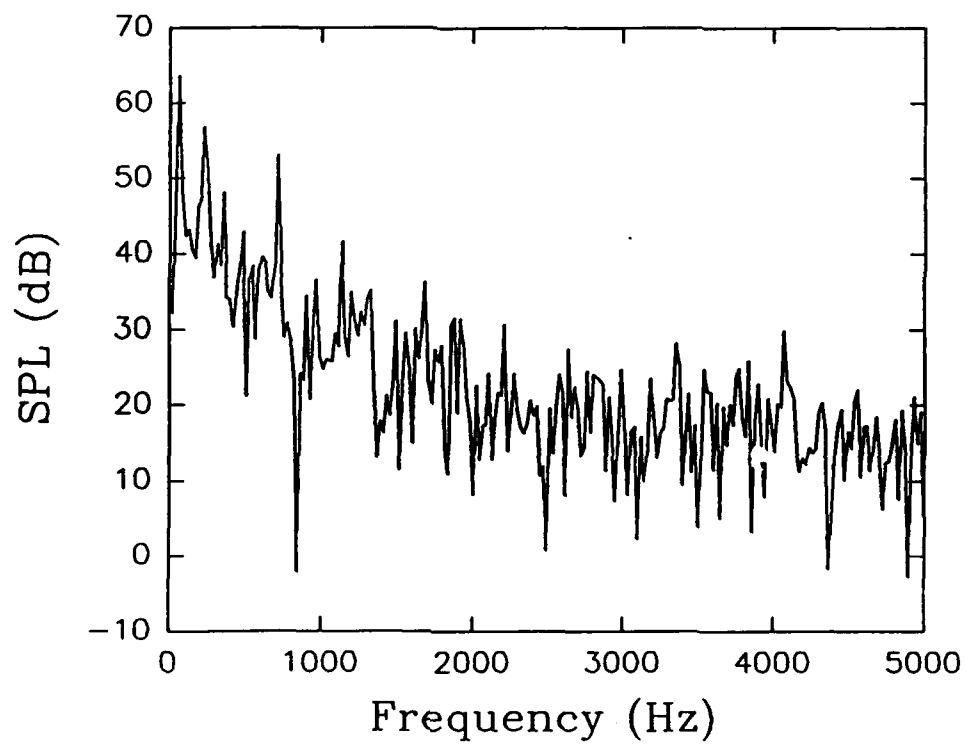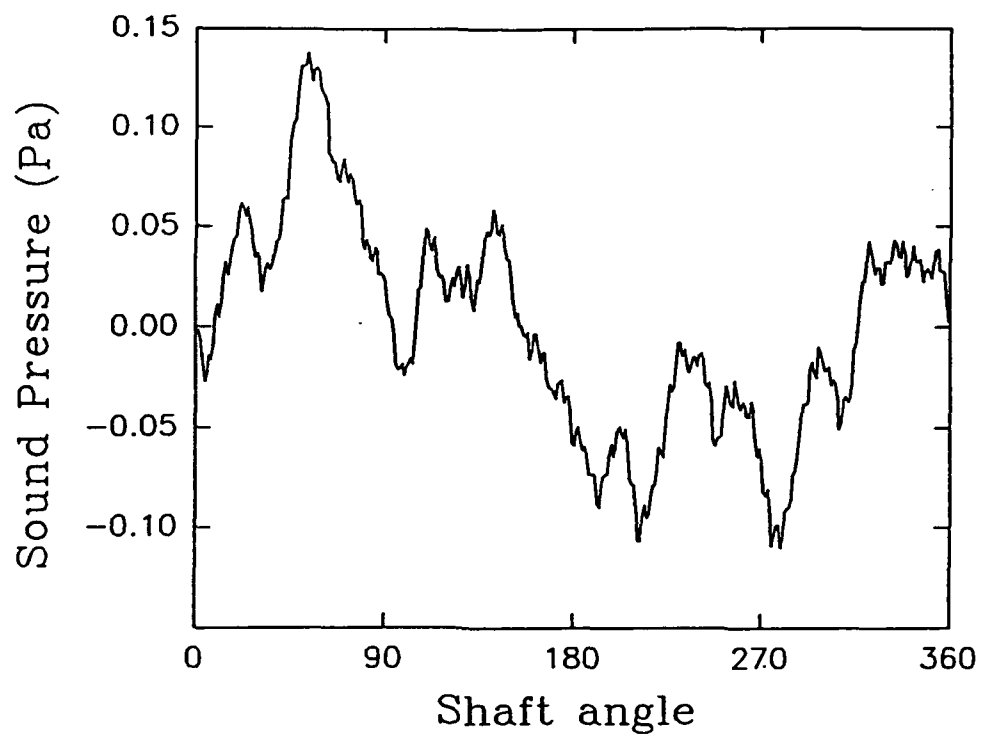   Controller at 2920 rpm at Location 1.
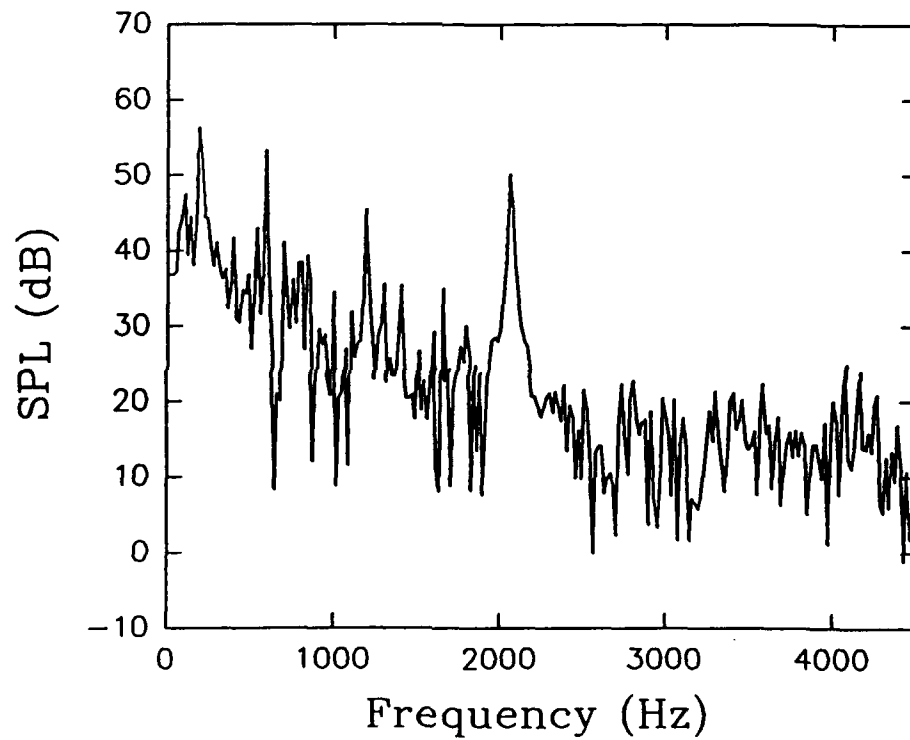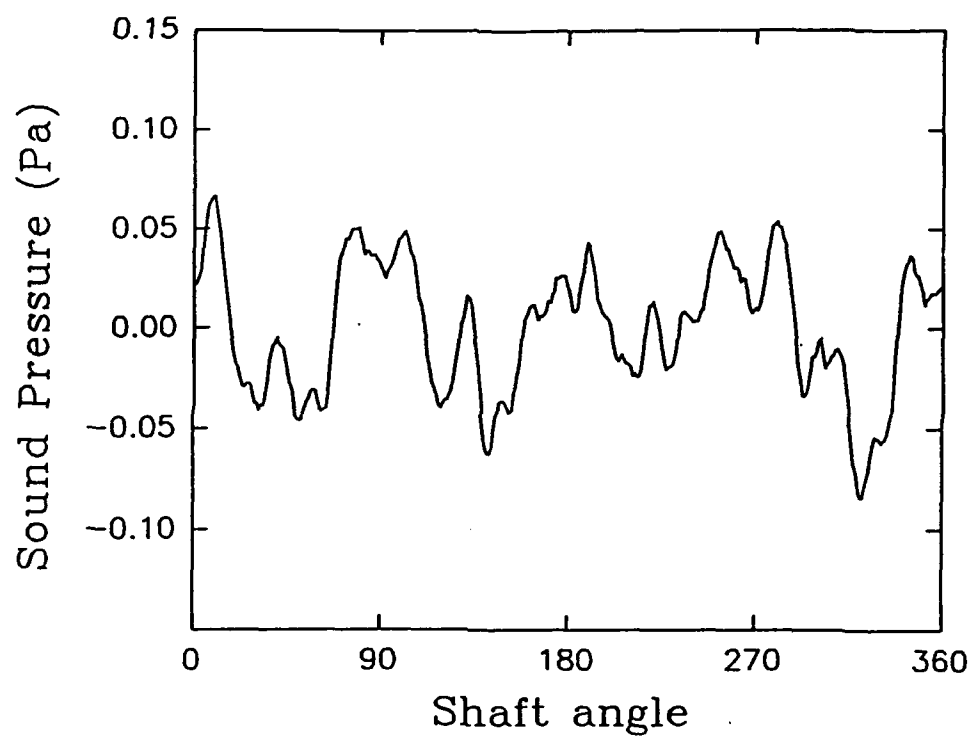
Figure 12(b)   Airborne Noise Characteristics and Frequency Spectra
Obtained with the Acrylic Casing and the aid of a
Controller at 2920 rpm at Location 2.
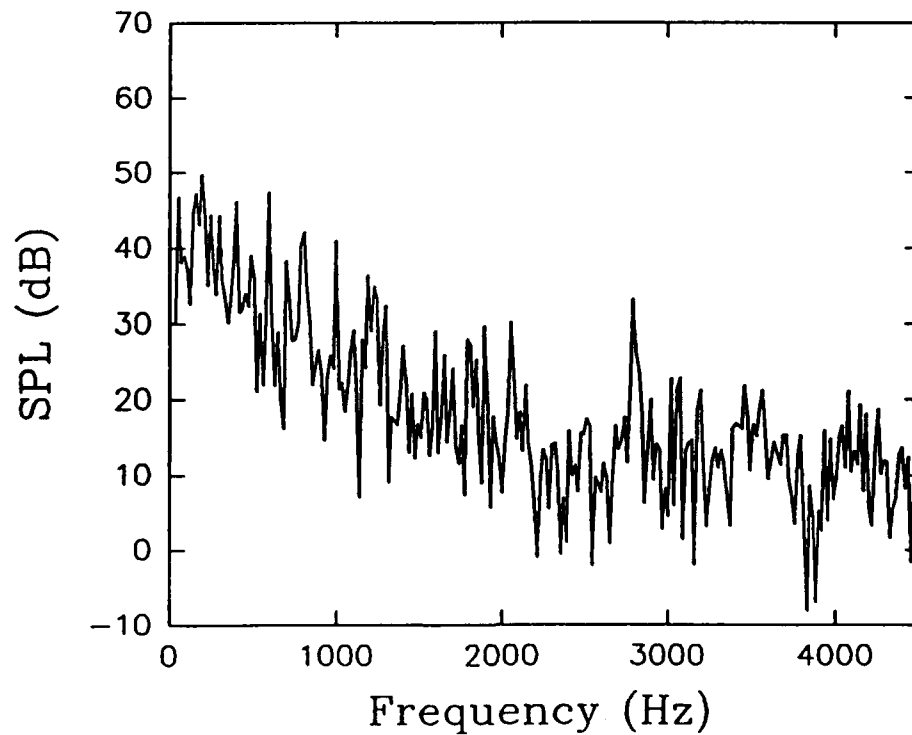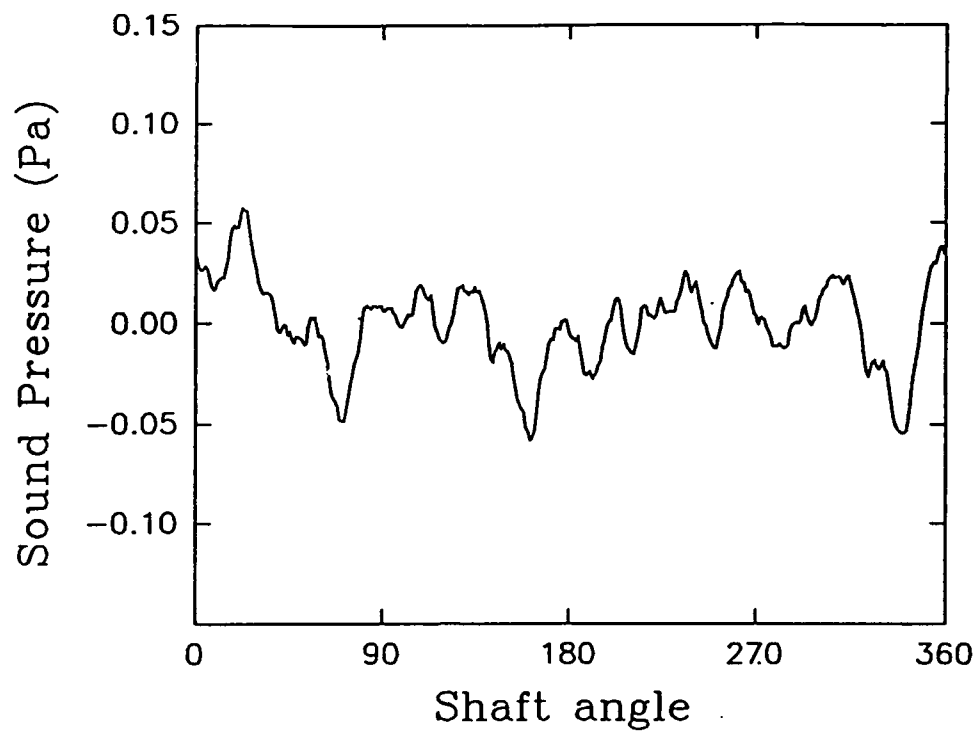
Figure 12(c)   Airborne Noise Characteristics and Frequency Spectra
Obtained with the Acrylic Casing and the aid of a
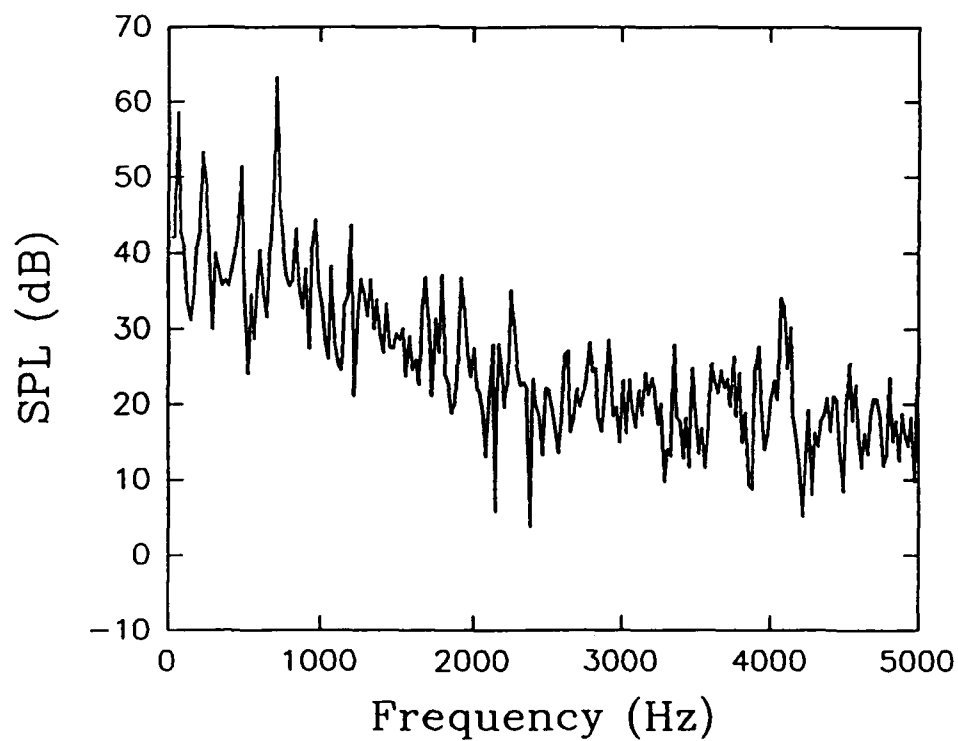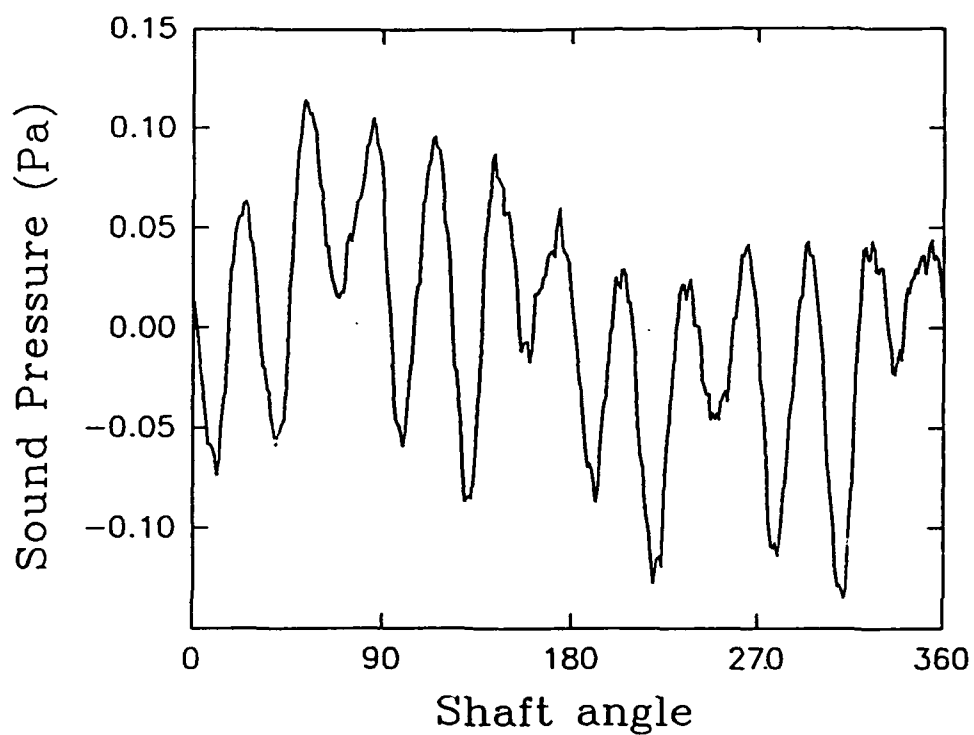Controller at 2920 rpm at Location 3.
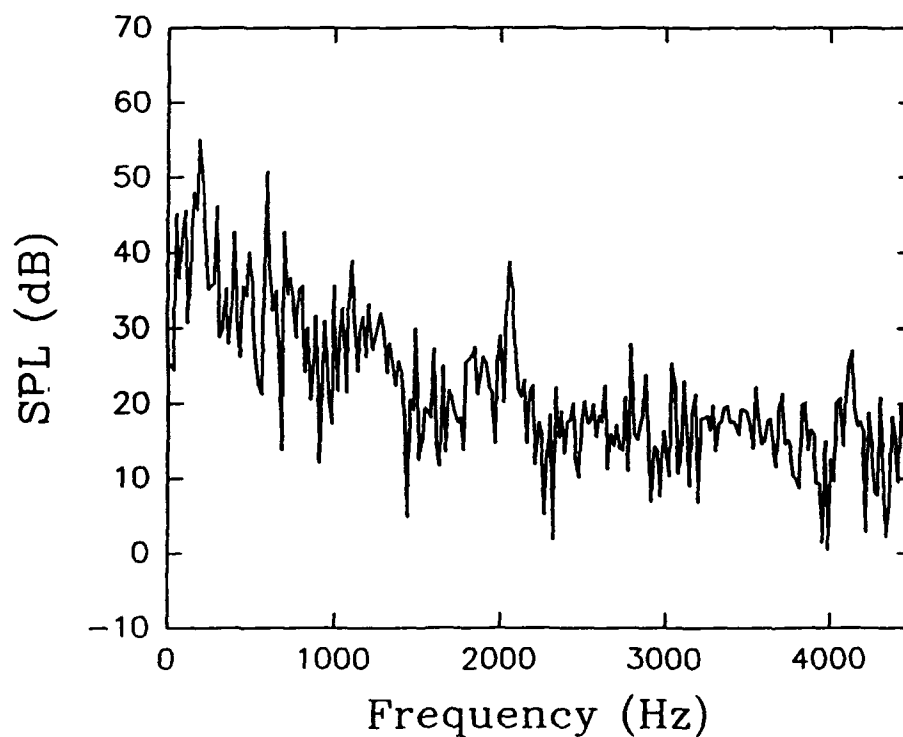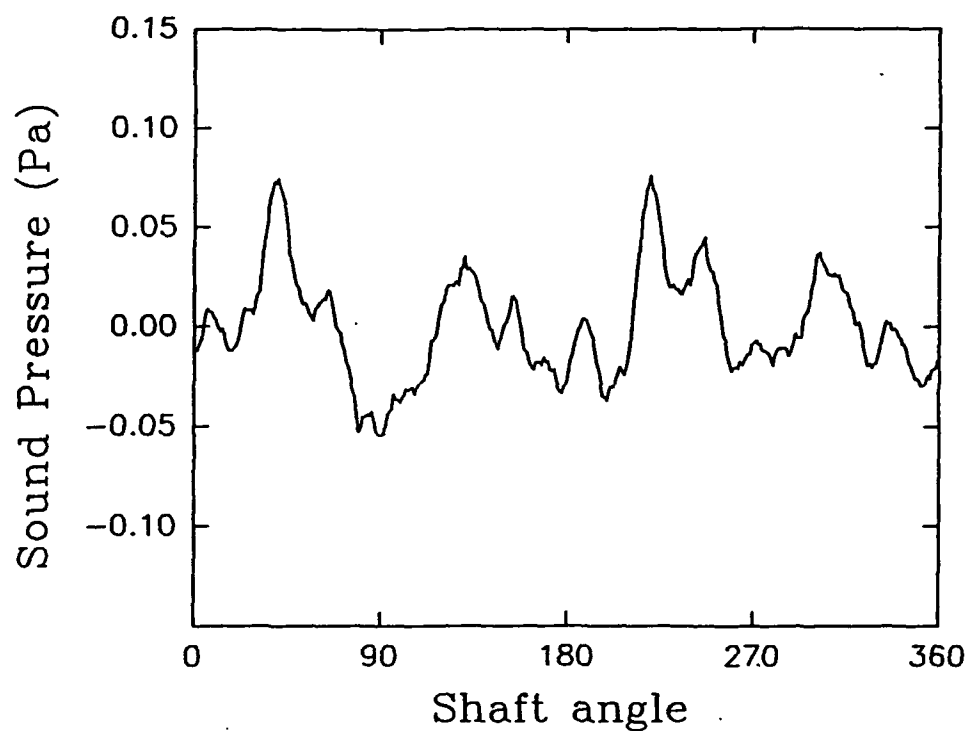
Figure 12(d)   Airborne Noise Characteristics and Frequency Spectra
Obtained with the Acrylic Casing and the aid of a
Controller at 2920 rpm at Location 4.
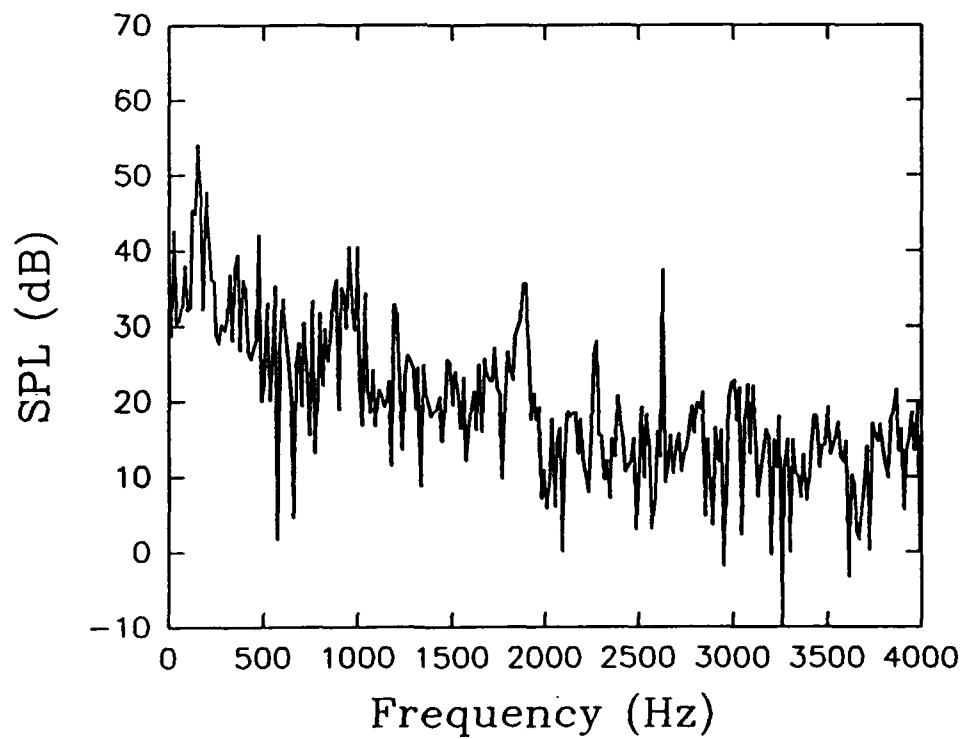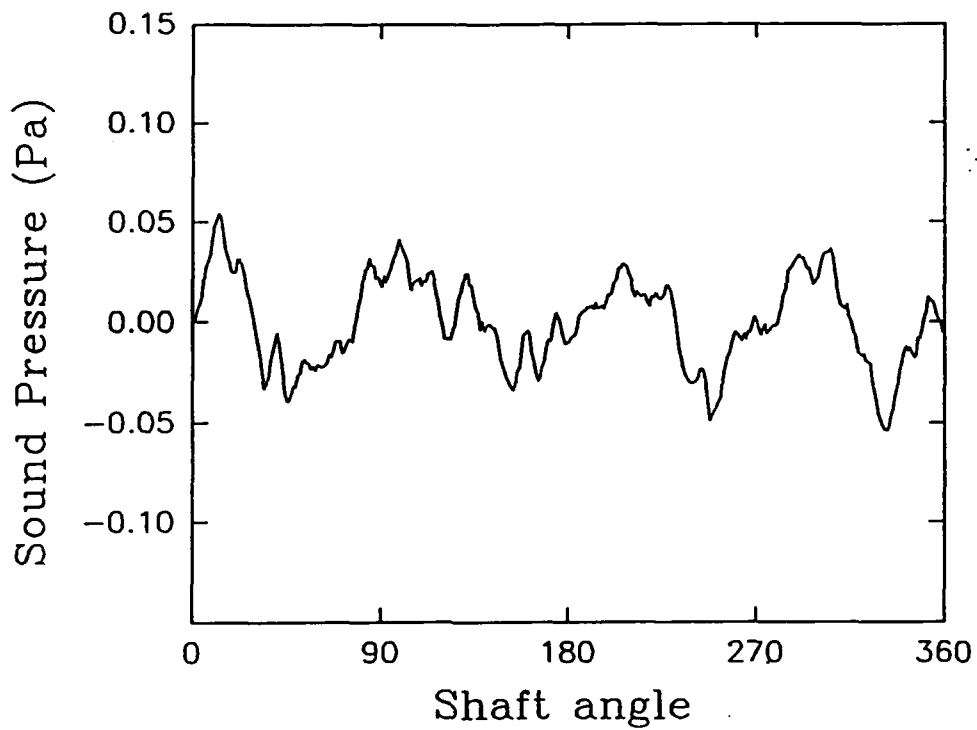
Figure 13(a)   Airborne Noise Characteristics and Frequency Spectra
                Obtained with the Acrylic Casing and the aid of a
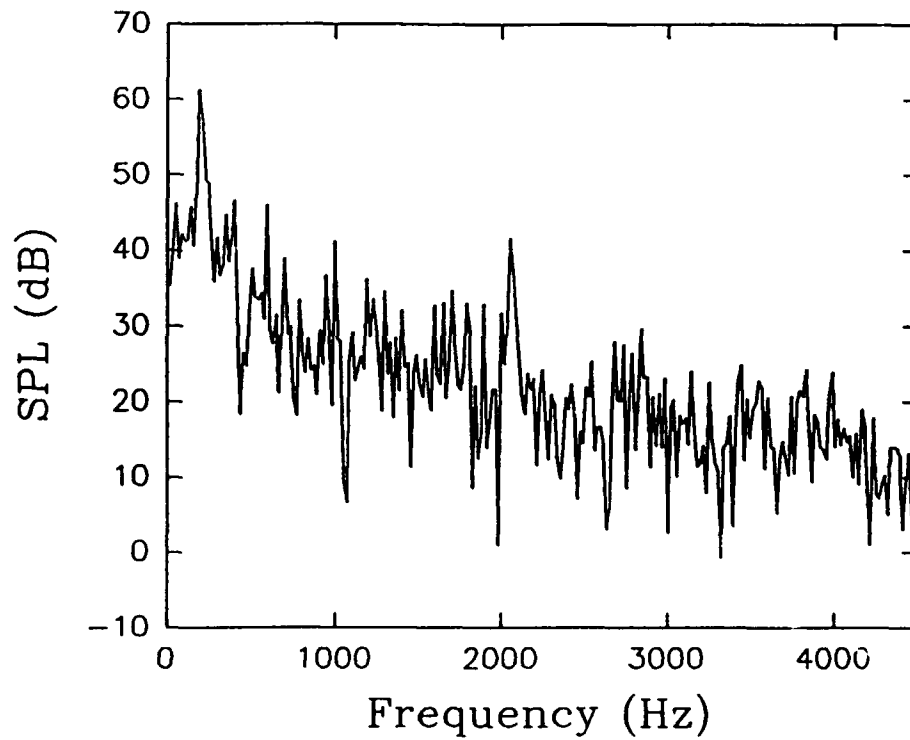   Controller at 2340 rpm at Location 1.
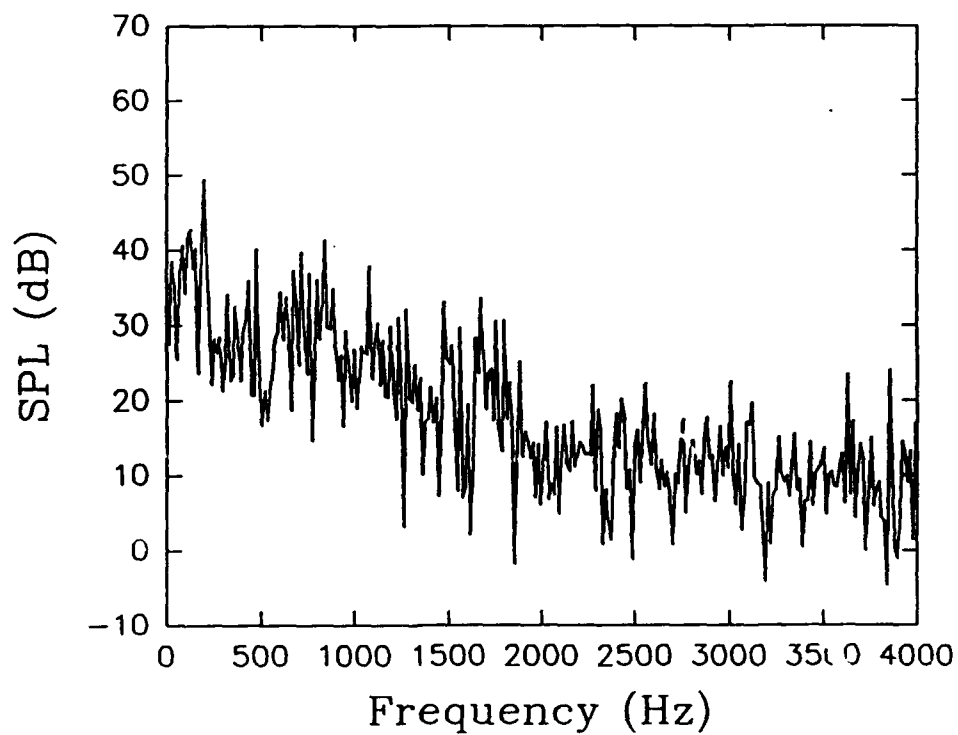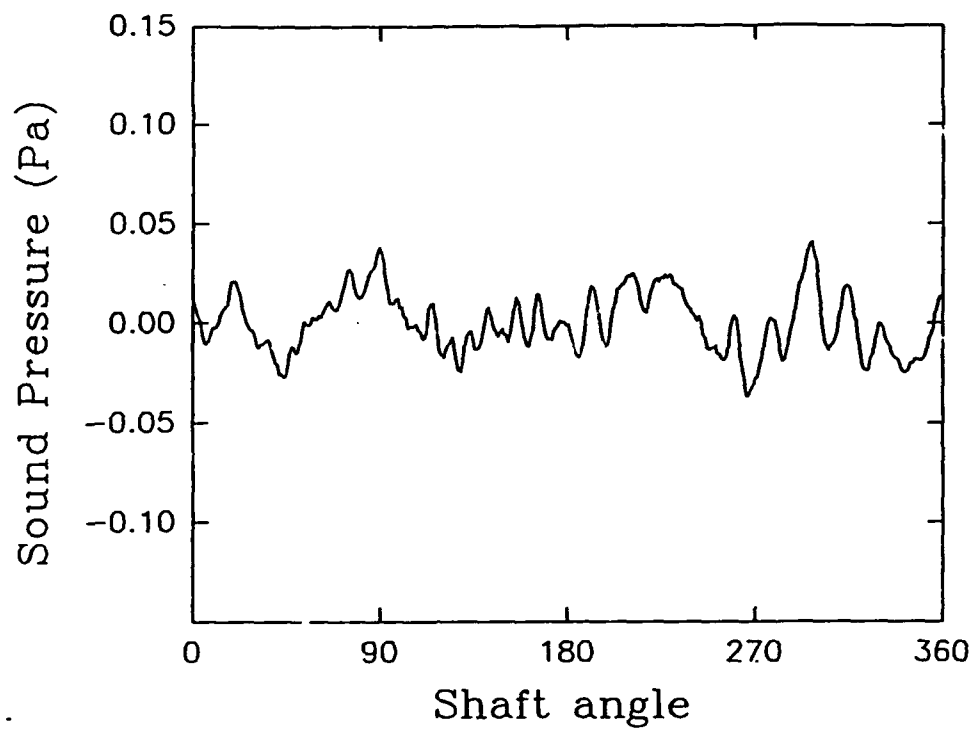
Figure 13(b)   Airborne Noise Characteristics and Frequency Spectra
Obtained with the Acrylic Casing and the aid of a
Controller at 2340 rpm at Location 2.
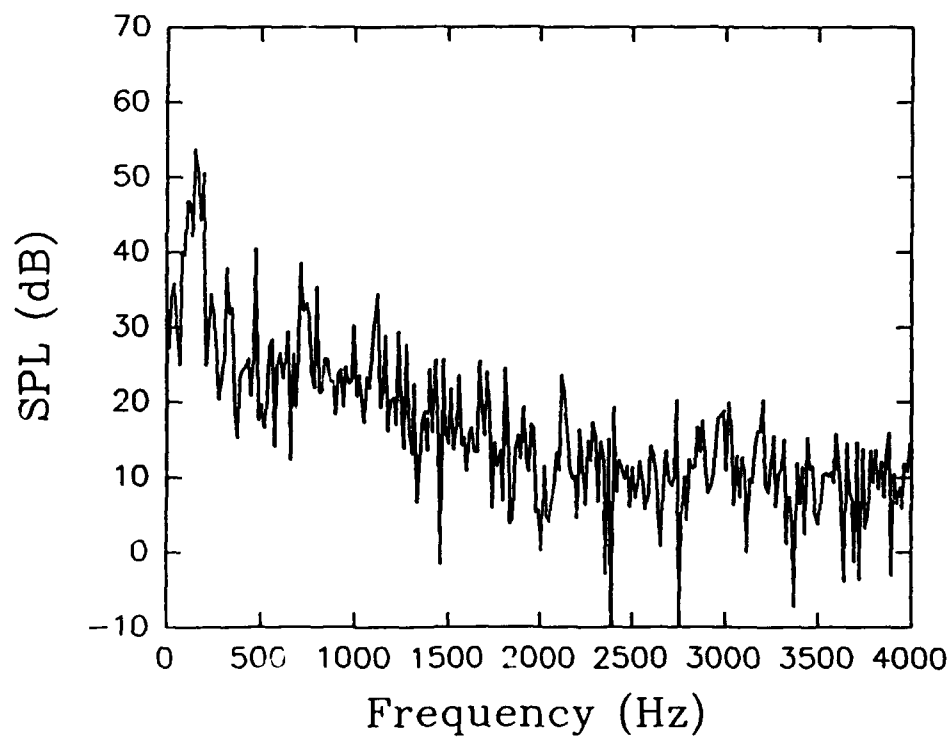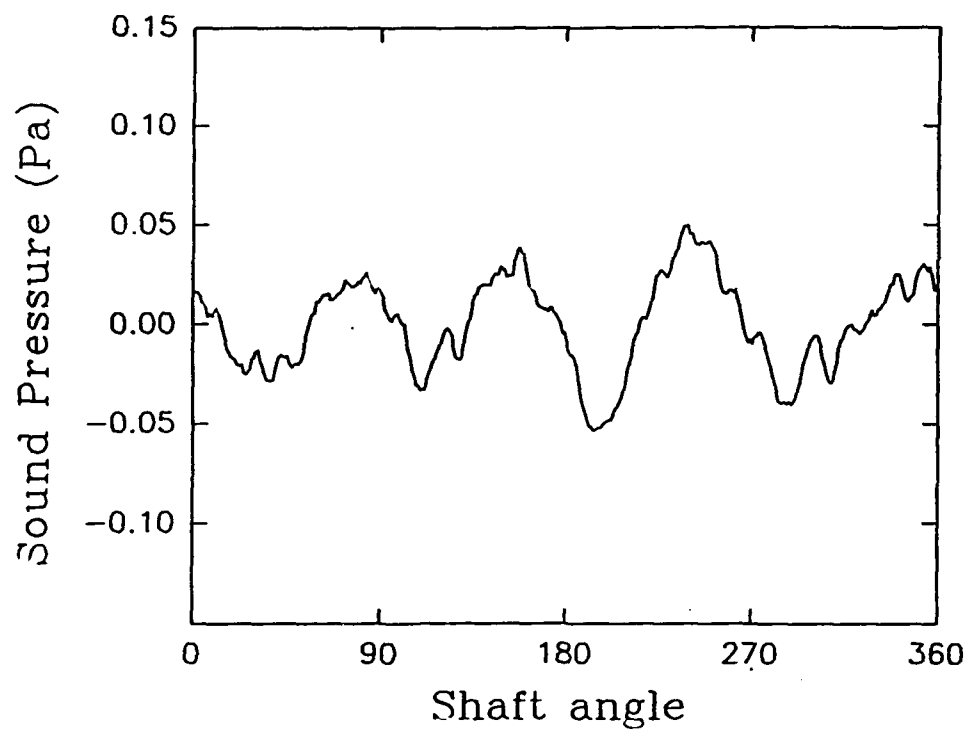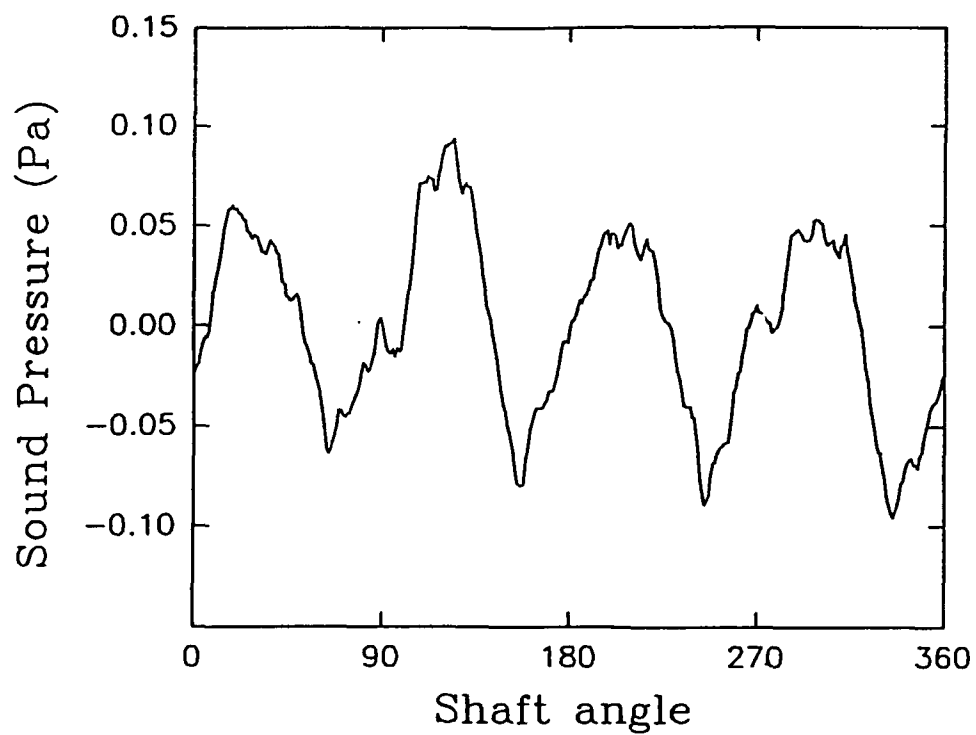
Figure 13(c)   Airborne Noise Characteristics and Frequency Spectra
                Obtained with the Acrylic Casing and the aid of a
                Controller at 2340 rpm at Location 3.
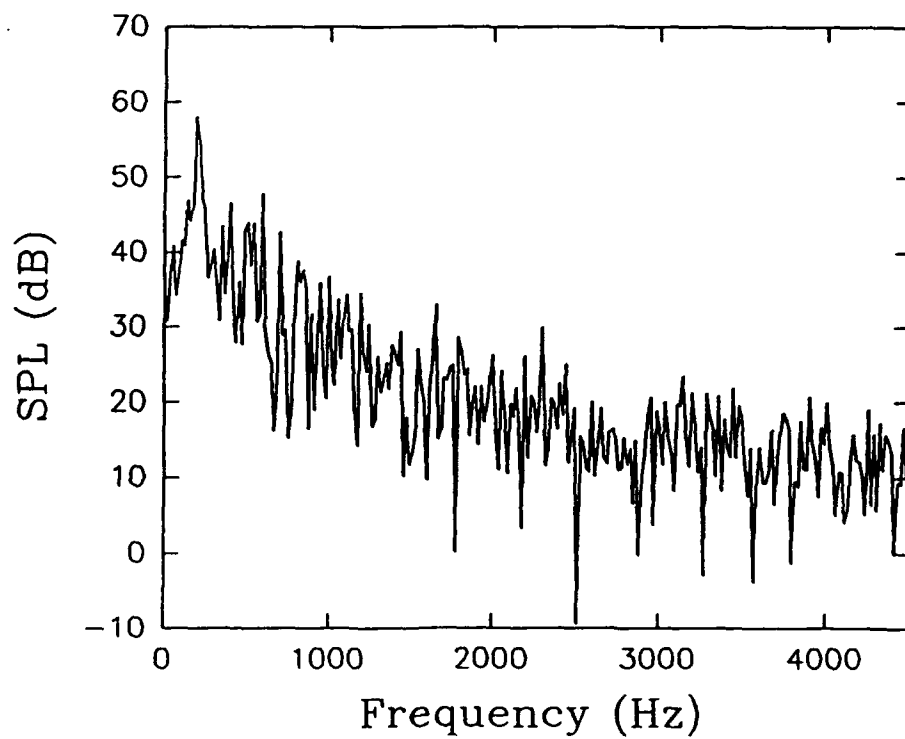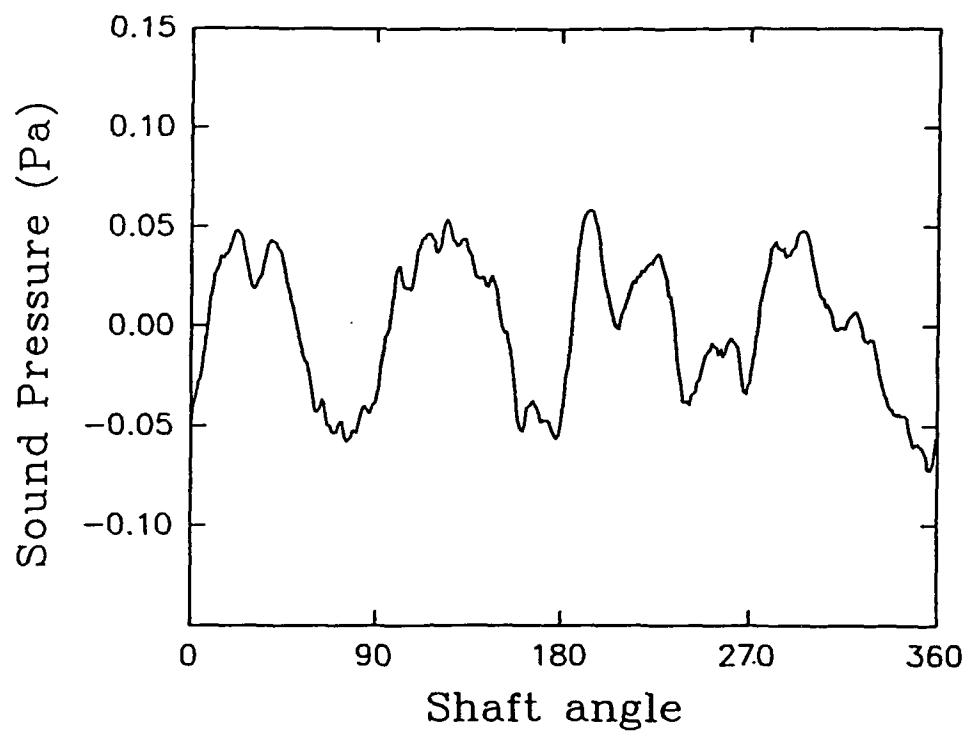
Figure 13(d)   Airborne Noise Characteristics and Frequency Spectra
               Obtained with the Acrylic Casing and the aid of a
               Controller at 2340 rpm at Location 4.
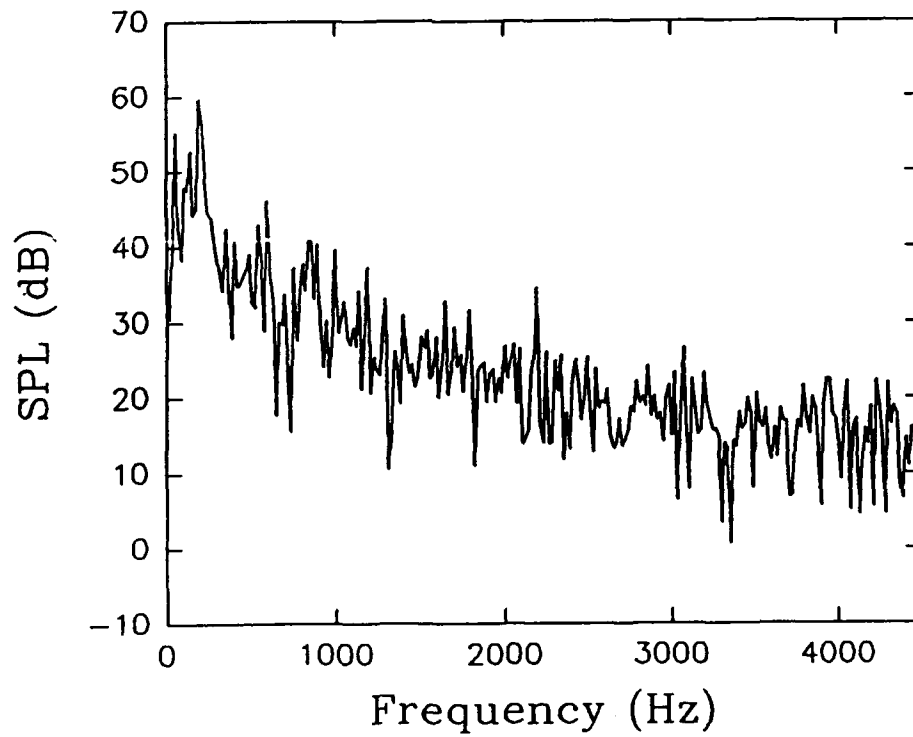
Figure 14   Airborne Noise Characteristics and Frequency Spectra
                 Obtained with the Acrylic Casing and the aid of a
                 Controller at 1770 rpm at Location 1.

Figure 15   Airborne Noise Characteristics and Frequency Spectra
Obtained with the Acrylic Casing and the aid of a
Controller at 1470 rpm at Location 1.
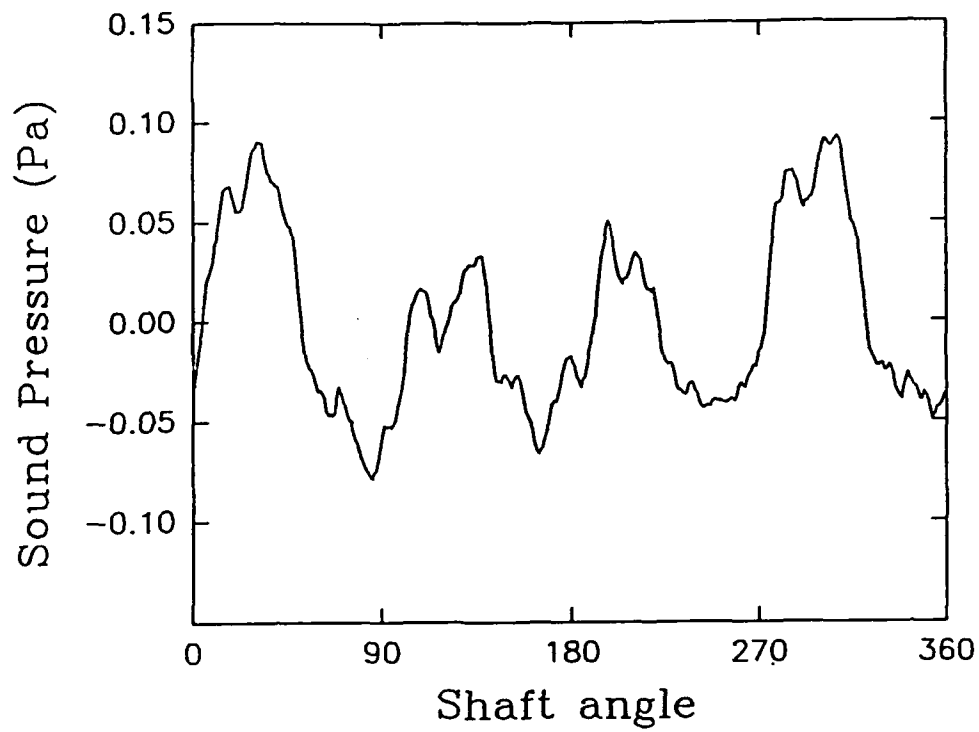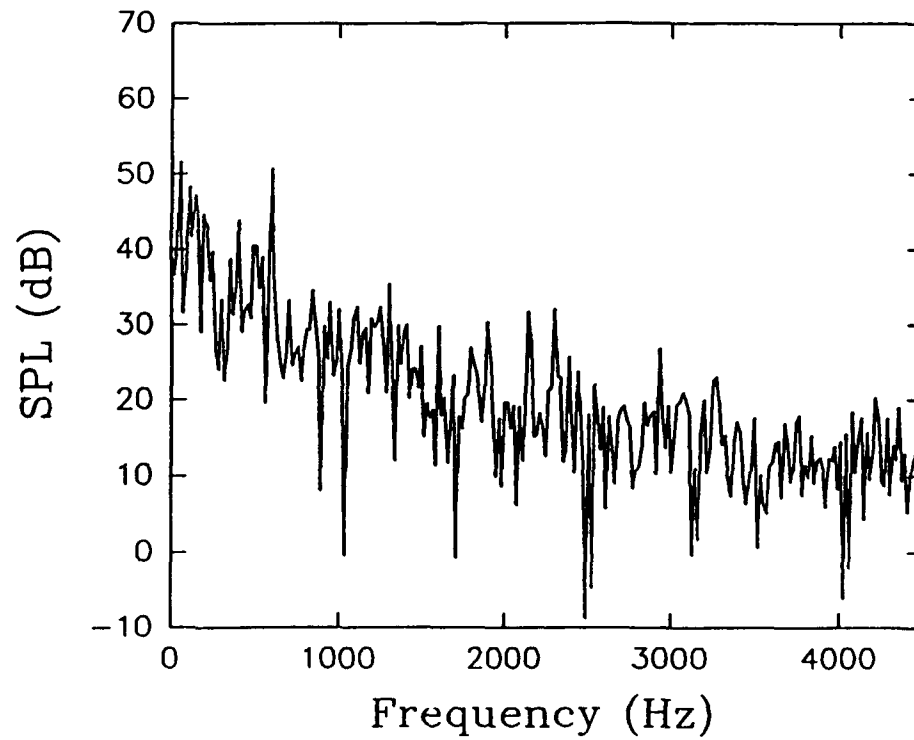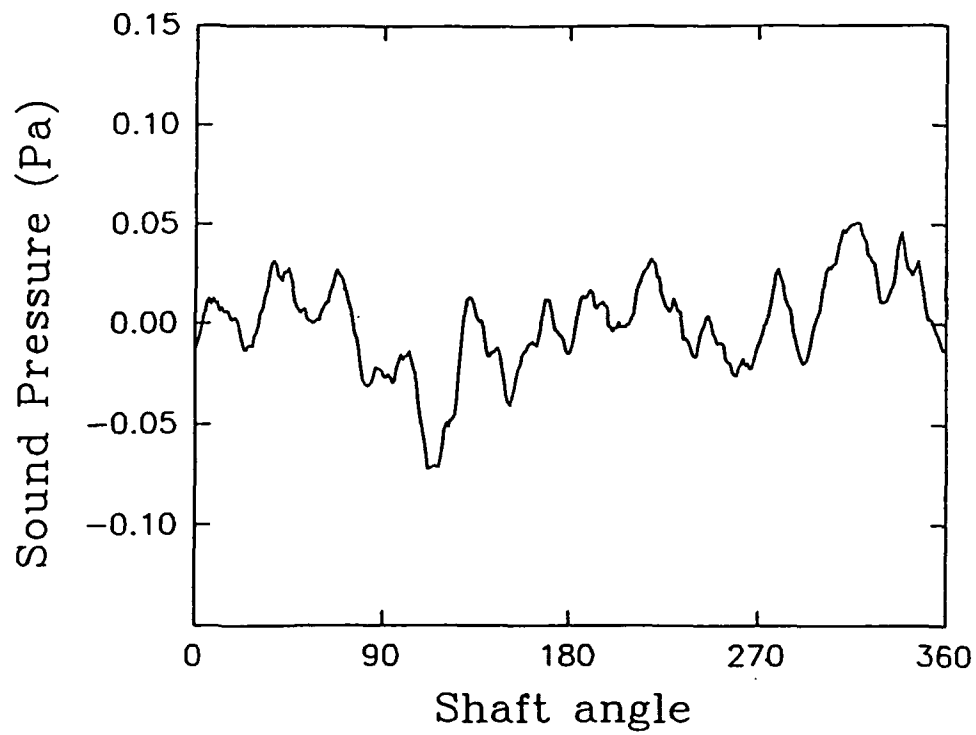
Figure 16(a)   Airborne Noise Characteristics and Frequency Spectra
Obtained with the Metal Casing and the aid of a
Controller at 3510 rpm at Location 1.

Figure 16(b)   Airborne Noise Characteristics and Frequency Spectra
                Obtained with the Metal Casing and the aid of a
                Controller at 3510 rpm at Location 2.

Figure 16(c)   Airborne Noise Characteristics and Frequency Spectra
Obtained with the Metal Casing and the aid of a
Controller at 3510 rpm at Location 3.

Figure 16(d)   Airborne Noise Characteristics and Frequency Spectra
                Obtained with the Metal Casing and the aid of a
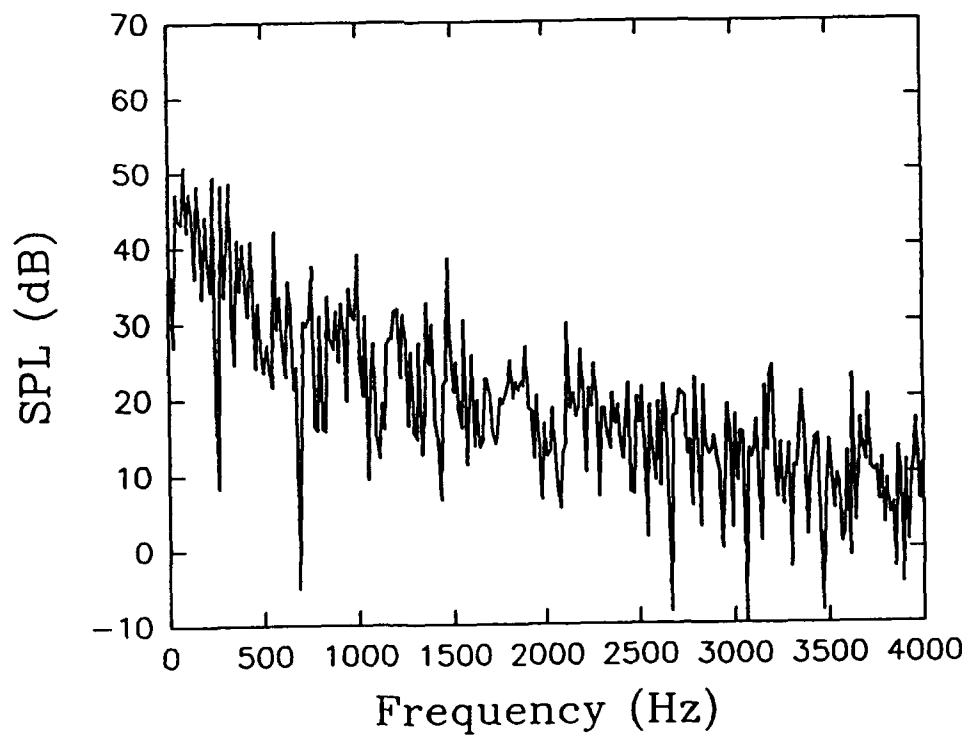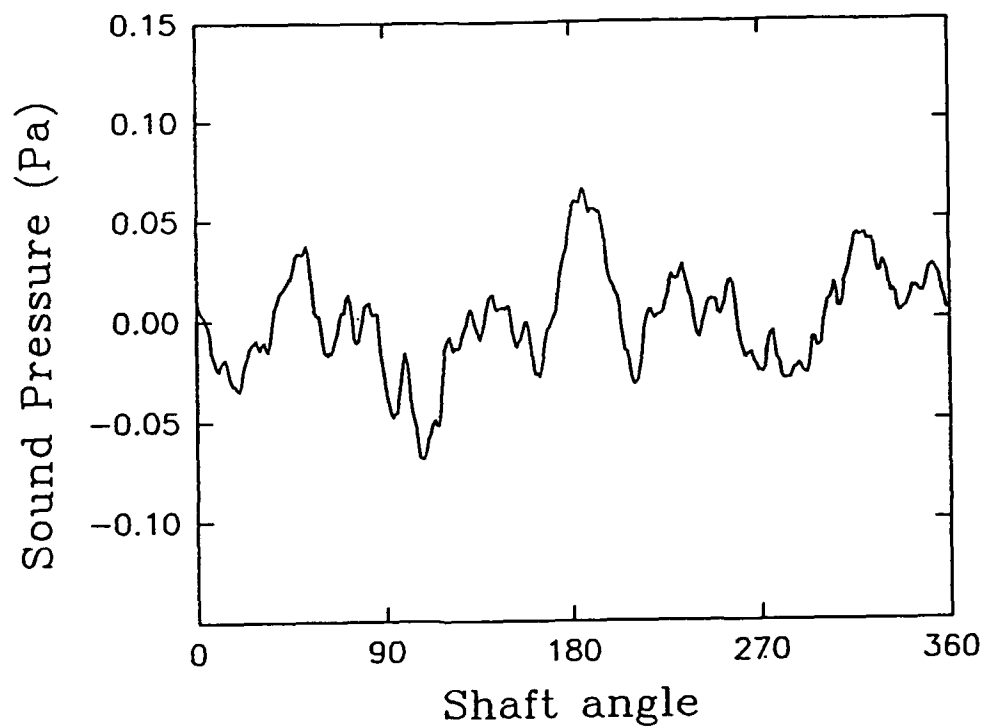   Controller at 3510 rpm at Location 4.

Figure 17(a)   Airborne Noise Characteristics and Frequency Spectra
                Obtained with the Metal Casing and the aid of a
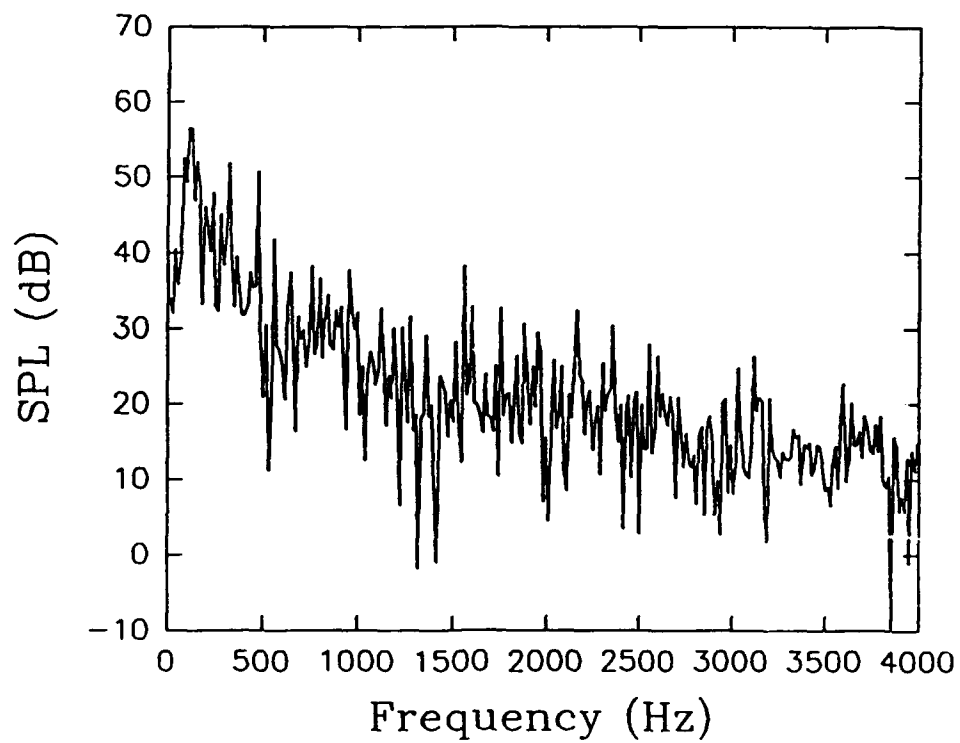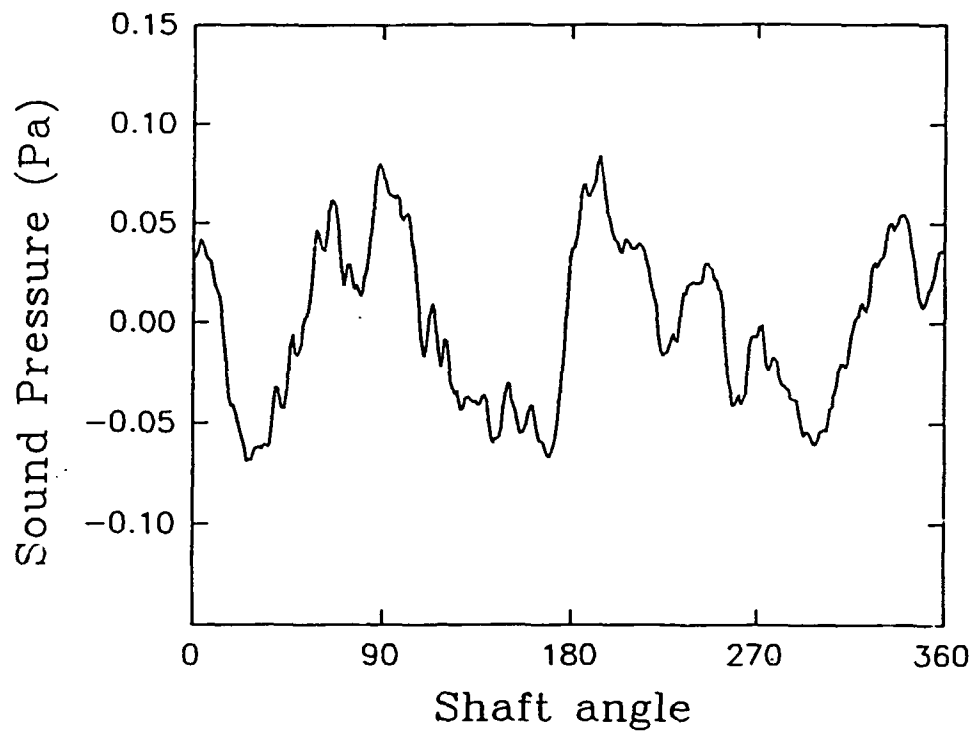   Controller at 2920 rpm at Location 1.

Figure 17(b) . Airborne Noise Characteristics and Frequency Spectra
Obtained with the Metal Casing and the aid of a
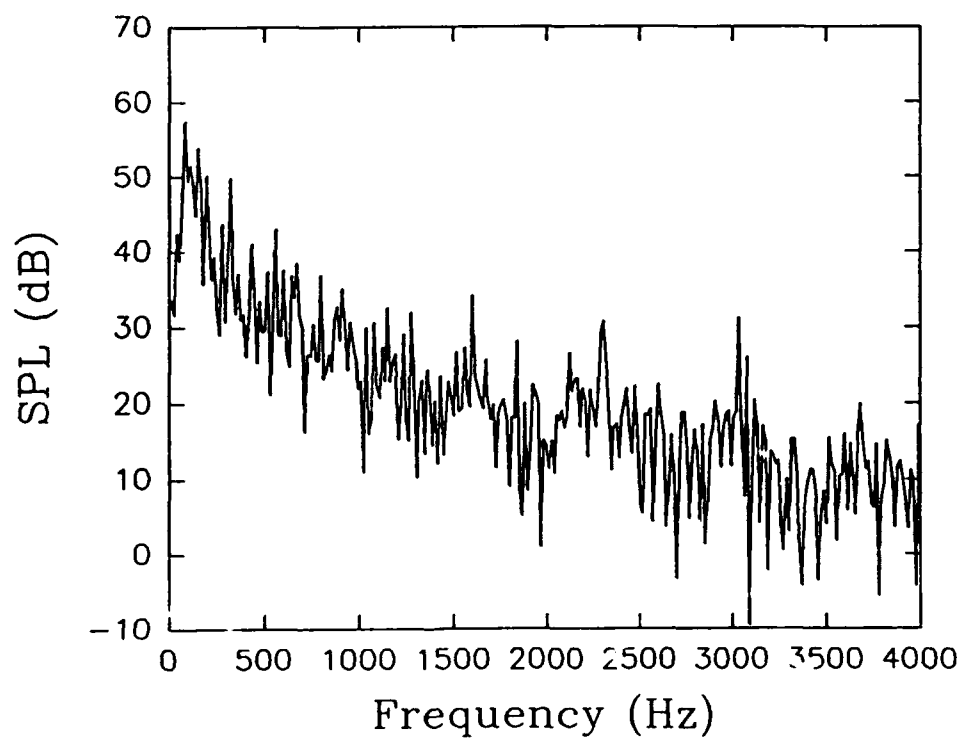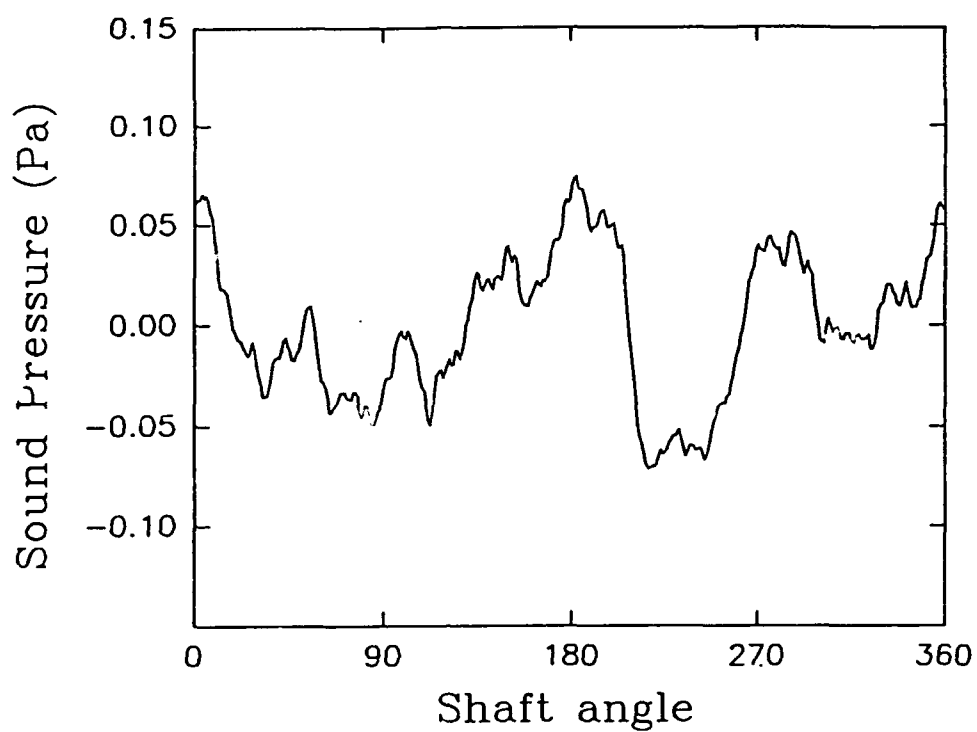Controller at 2920 rpm at Location 2.

Figure 17(c) Airborne Noise Characteristics and Frequency Spectra Obtained with the Metal Casing and the aid of a Controller at 2920 rpm at Location 3.

Figure 17(d) Airborne Noise Characteristics and Frequency Spectra
Obtained with the Metal Casing and the aid of a
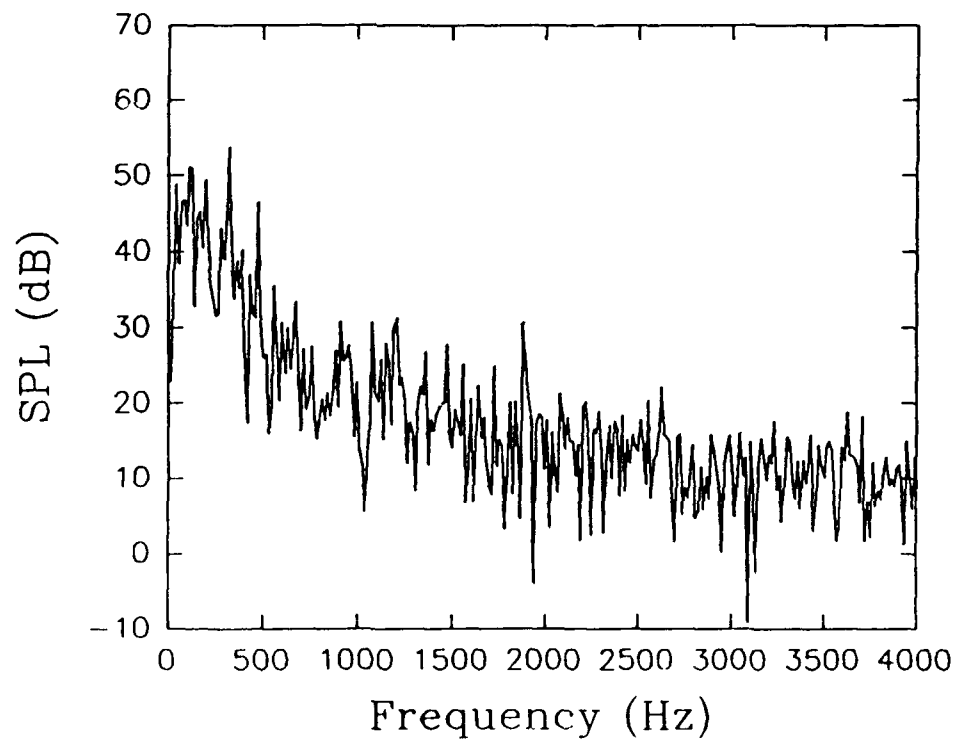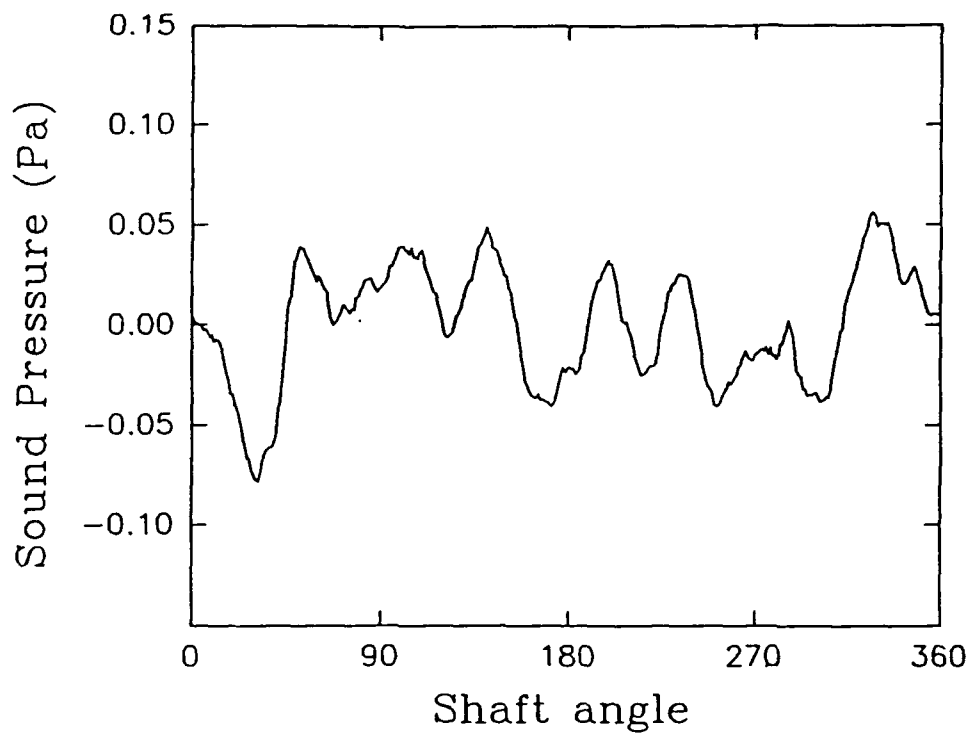Controller at 2920 rpm at Location 4.

Figure 18(a)   Airborne Noise Characteristics and Frequency Spectra
Obtained with the Metal Casing and the aid of a
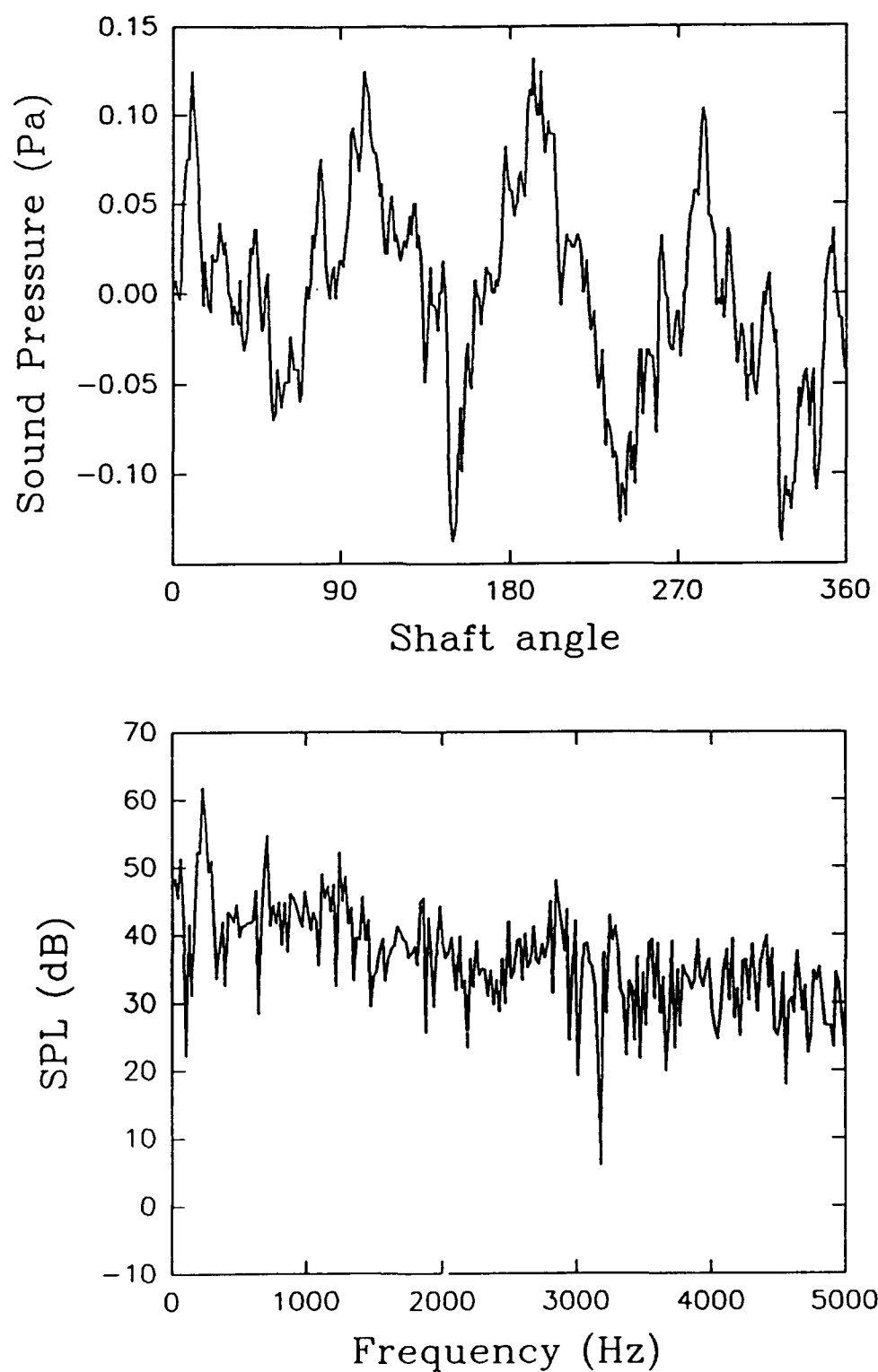Controller at 2340 rpm at Location 1.

Figure 18(b)   Airborne Noise Characteristics and Frequency Spectra
Obtained with the Metal Casing and the aid of a
Controller at 2340 rpm at Location 2.

Figure 18(c)   Airborne Noise Characteristics and Frequency Spectra
Obtained with the Metal Casing and the aid of a
Controller at 2340 rpm at Location 3.

Figure 18(d)   Airborne Noise Characteristics and Frequency Spectra
Obtained with the Metal Casing and the aid of a
Controller at 2340 rpm at Location 4.

Figure 19(a)   Instantaneous Airborne Noise Characteristics and Frequency
Spectra Obtained with the Metal Casing and the aid of a
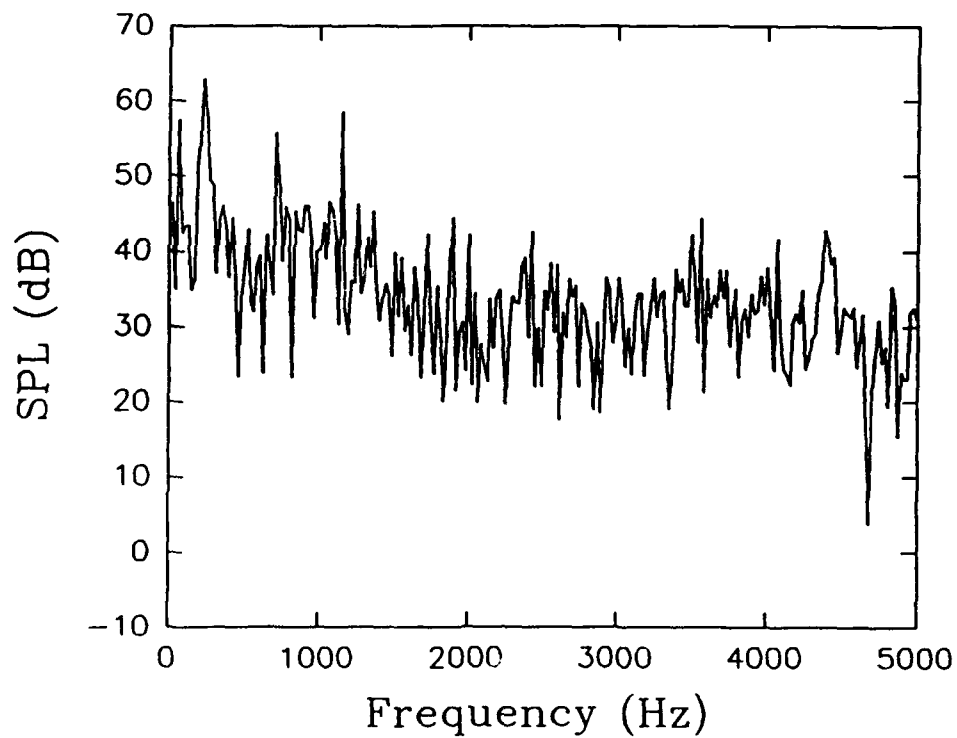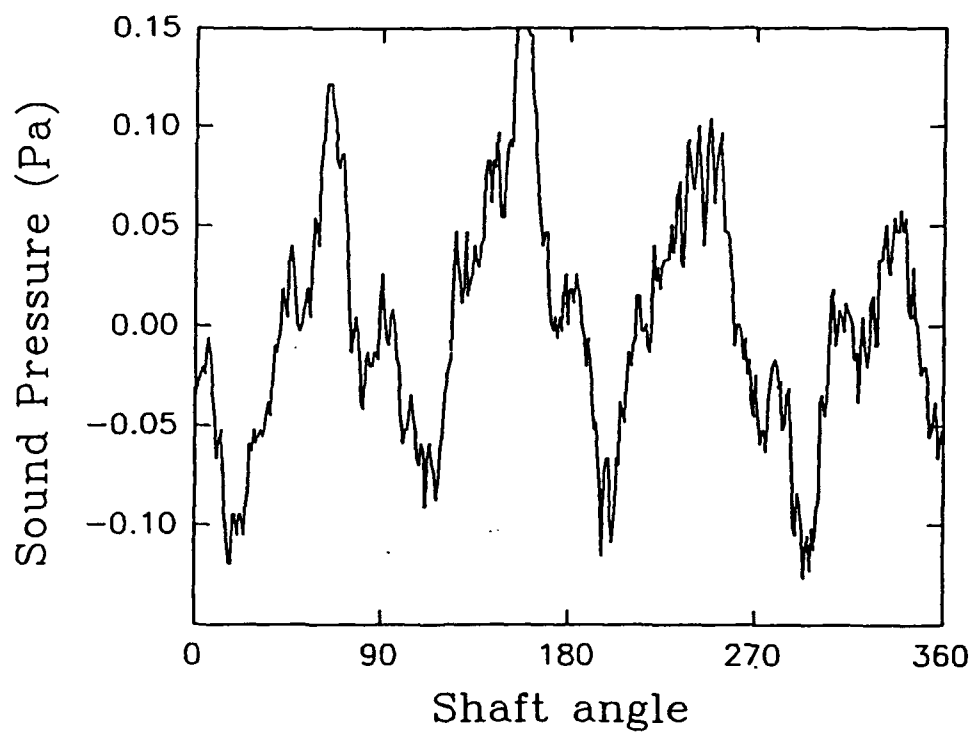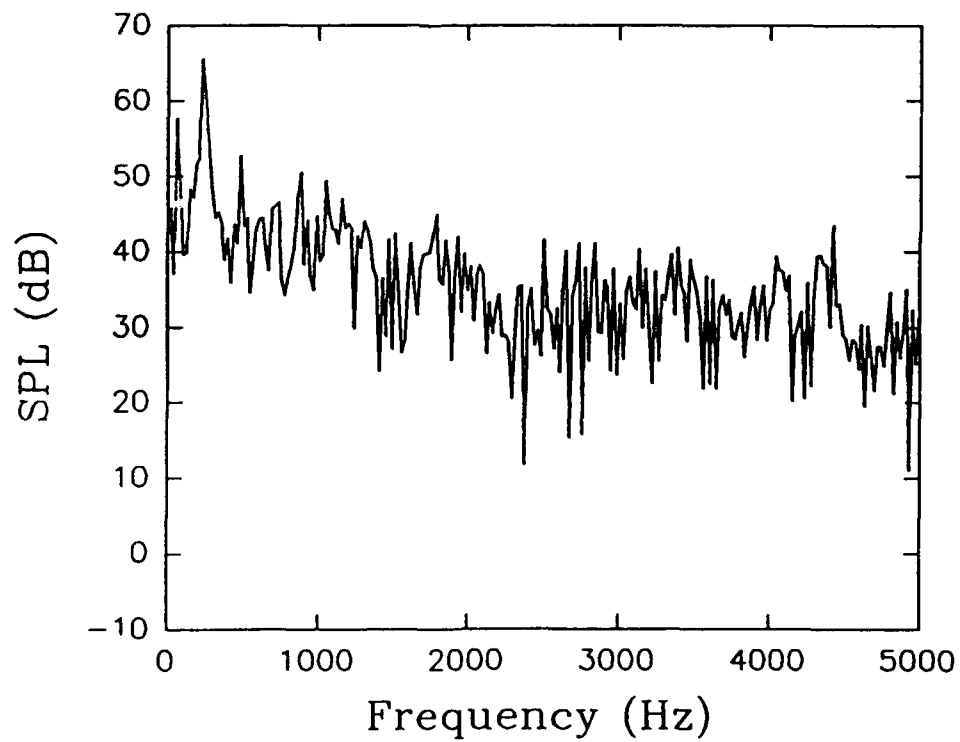Controller at 3510 rpm at Location 1.

Figure 19(b)   Instanaeous Airborne Noise Characteristics and Frequency
Spectra Obtained with the Metal Casing and the aid of a
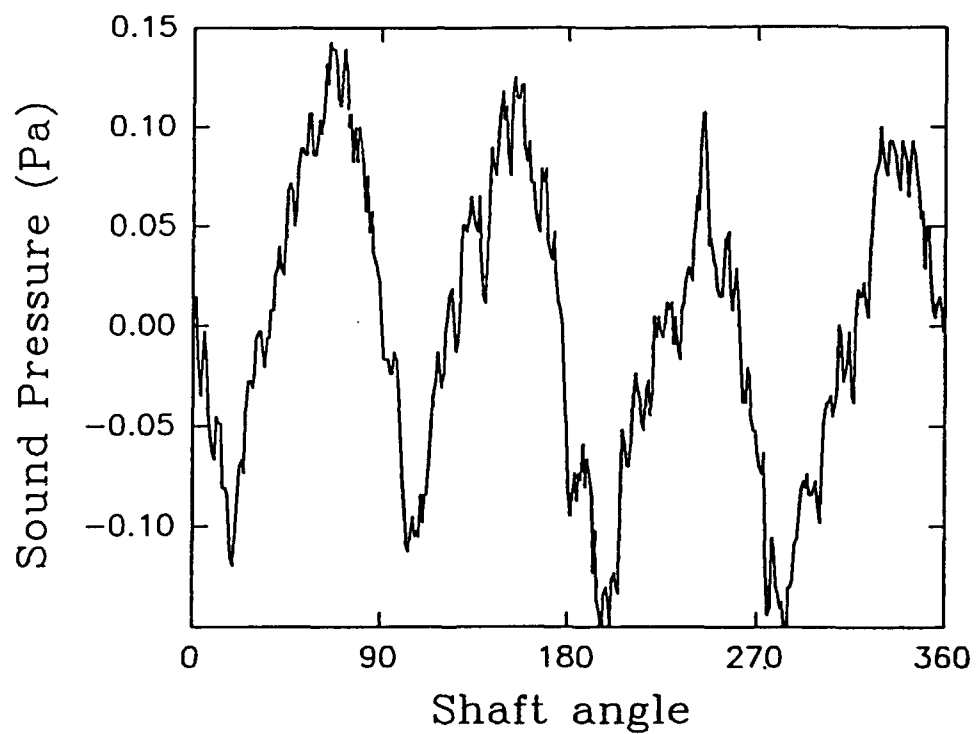Controller at 3510 rpm at Location 2.

Figure 19(c)   Instananeous Airborne Noise Characteristics and Frequency
                Spectra Obtained with the Metal Casing and the aid of a
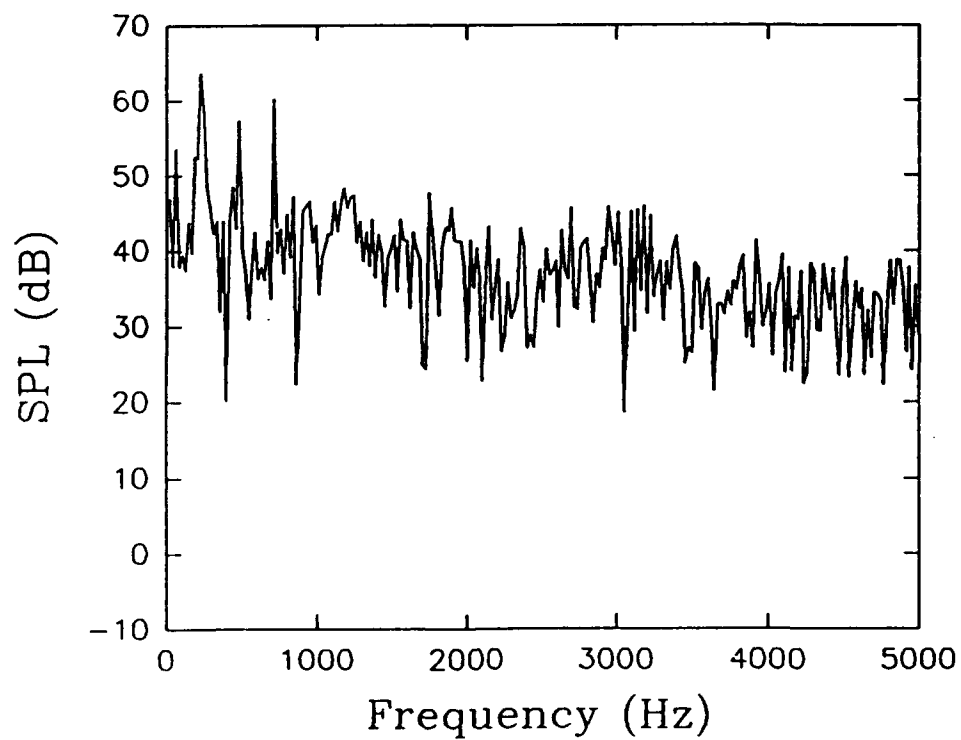   Controller at 3510 rpm at Location 3.

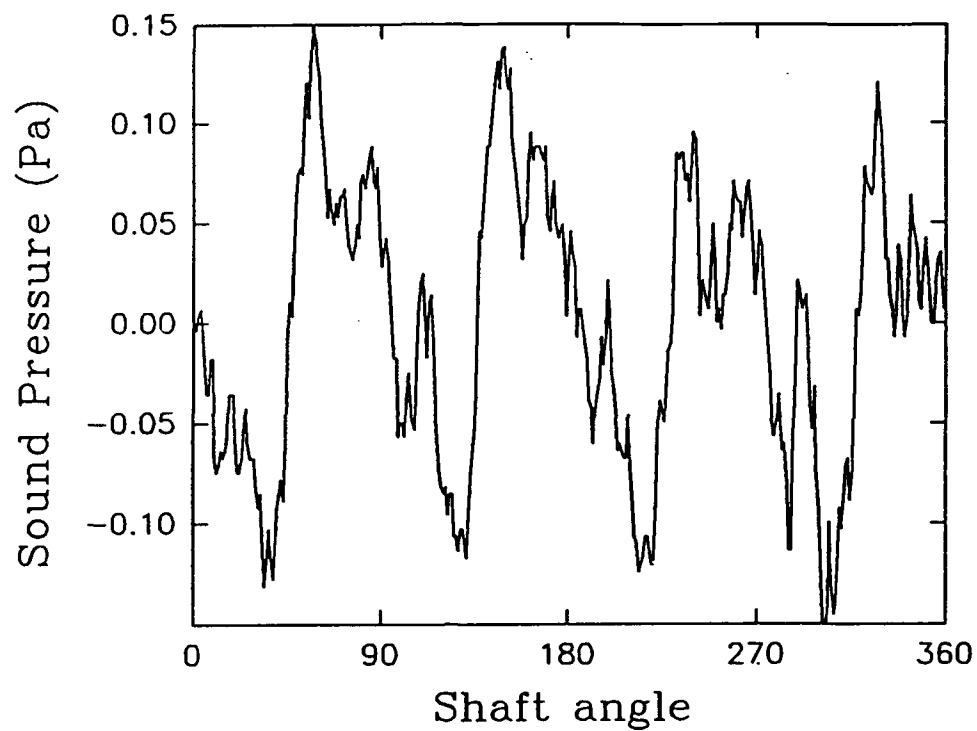Figure 19(d)   Instanaeous Airborne Noise Characteristics and Frequency
                Spectra Obtained with the Metal Casing and the aid of a
                Controller at 3510 rpm at Location 4.